CRANFIELD UNIVERSITY

Zhongyuan Wang

RANS AND DETACHED-EDDY SIMULATION OF THE NASA TRAP WING FOR HILIFTPW-1

Cranfield University
MSc by Research

MSc by Research
Academic Year: 2016 - 2018

Supervisor: Dr. Panagiotis Tsoutsanis
Associate Supervisor: Dr. Karl Jenkins
May 2018

CRANFIELD UNIVERSITY

Cranfield University
MSc by Research

MSc by Research

Academic Year 2016 - 2018

Zhongyuan Wang

MSc by Research

Supervisor: Dr. Panagiotis Tsoutsanis
Associate Supervisor: Dr. Karl Jenkins
May 2018

This thesis is submitted in partial fulfilment of the requirements for the degree of MSc by Research

ABSTRACT

This project aims to study and perform a turbulent flow simulation over the NASA Trap Wing by exploring the numerical aerodynamic predictions capacity of high lift configurations using two S-A, k-ω SST and DES method for comparison in ANSYS Fluent software, among which DES method has been paid key attention for its accuracy as a CFD high lift prediction tool. NASA Trap Wing geometry from High lift Prediction Workshop-1 is applied in this project with slat angle of 30° and flap angle of 25°. Prediction results are analysed for several flow characteristics including pressure distribution, force and moment coefficient as well as skin friction and some other flow visualization. Results show that the DES method performs the best flow prediction near stall, however, it fails to provide as good flow characteristics at low pitch angles as S-A model and fails to show stall patterns. Both S-A and k-ω SST model shows a premature stall due to massive separation at high AoAs, while k-ω SST model gives a worst prediction results among all the three turbulent models applied. Restarted S-A model, based on experience from the 1st AIAA High lift Prediction Workshop, means high pitch angle case restarted with the converged solution of lower pitch angle case, which improves the prediction results of original S-A model by delaying the separation in very limited extent. Further researches have been proposed including key local mesh adaption, further application of URANS model for comparison, higher AoA cases for DES model for testing its capability, increasing the pitch angles cases more gradually for better prediction.

Keywords:

RANS, DES (Detached-eddy Simulation), High lift Prediction Workshop, NASA trap wing, stall prediction.

ACKNOWLEDEMENTS

I wish to express my gratitude to my supervisor, Dr. Panagiotis Tsoutsanis, for the responsible supervising, valuable help and discussion during my MSc by Research project.

I would like to also thank Dr. Karl Jenkins, not only for his enlightening advice of the research method, but also for providing corresponding knowledge for the project.

In addition, I would like to thank my friends, Dongyu Li and Sipeng Song, for their support and company during the length of my MSc study.

Finally, a big thank you to my family for their love and support in the duration of my MSc course.

TABLE OF CONTENTS

LIST OF FIGURES

LIST OF TABLES

LIST OF EQUATIONS

NOMENCLATURE

Abbreviation

AIAA	American Institute of Aeronautics and Astronautics
AoA	Angle of Attack
AUSM	Advection Upstream Splitting Method
CBL	Confluent Boundary Layer
CCW	Circulation Control Wing
CFD	Computational Fluid Dynamics
DDES	Delayed Detached-eddy Simulation
DES	Detached-eddy Simulation
GIS	Grid Induced Separation
IDDES	Improved Delayed Detached-eddy Simulation
LES	Large-eddy Simulation
LLM	Log-Layer Mismatch
PIV	Particle Imaging Velocimetry
RANS	Reynolds-averaged Navier-Stokes
S-A	Spalart-Allmaras
SGS	Subgrid Scale
SST	Shear Stress Transport
ZDES	Zonal Detached-eddy Simulation

Latin Symbols

C_L	Lift Coefficient
C_{Lmax}	Maximum Lift Coefficient
C_D	Drag Coefficient
C_M	Moment Coefficient
C_P	Pressure Coefficient
k	Specific Turbulence Kinetic Energy
Ma	Mach Number
p	Pressure
Re	Reynolds Number
T	Temperature

Greek Symbols

α	Angle of Attack
$\Delta_{\|\|}$	Grid Spacing Parallel to the Wall
ϵ	Dissipation Rate of the Kinetic Energy
δ	Boundary Layer Thickness
$\tilde{\nu}$	Kinematic Eddy Viscosity
ω	Specific turbulent Dissipation

1 Introduction

1.1 Motivation of the project

The study of high lift aerodynamics can go back to 1914 when the first flap was put into an experiment for testing of shape[1] as shown in Figure 1.1. Then in 1921[2], Handley Page gave a lecture about his ten years' work on the effectiveness of airfoils slots and slats, which also proved the airfoil with multiple-elements can develop more lift. Nowadays, high lift configuration with multiple elements has been universally applied in the field of aircraft design, but the prediction of high lift flow field is still a challenge. Flow feature at high angles of attack, which means near stall and post-stall, shows even more complex behaviour, which is particularly difficult for a three-dimensional airfoil. Flow physics may happen over high lift flow are stated in Rumsey and Ying[3], mainly including shock/boundary layer interaction, transition for each element, boundary layer separation and possible former element wake merging with boundary layer of element downstream.

Figure 1.1 RAF 9 Airfoil with a 0.385c plain flap [1]

On account of so many challenges for high lift prediction, to solve the difficulties in accurately predicting complicated characteristics over high lift flows, an international workshop for high lift flow prediction, namely, the First AIAA CFD High Lift Prediction Workshop (HiLiftPW-1)[4], came into being in 2009 to advance that state of art. According to statistics, RANS method with one equation (S-A model) and two equation (k-ω SST model) are two methods that have been most widely used during HiLiftPW-1. However, DES, as a new arising numerical method, is now acknowledged and widely used as its combination of RANS and LES leads to both a relatively good performance and economical computation resource. To explore the numerical prediction capability as well as compare the

performance of accuracy of high lift flow prediction between different turbulent models, S-A, $k-\omega$ SST and DES will be applied as CFD tool in this research.

1.2 Aims of the project

The aim of this paper is to explore the numerical aerodynamic predictions of high lift configurations using three different turbulent methods: S-A model, k-w SST model and DES model (Detached-eddy Simulation with the Spalart-Allmaras model). Also, results comparison between the three will also be carried out to assess their performance as a high lift flow prediction tool in ANSYS Fluent software. The high lift configuration studied in this paper is based on a semi-span three-element NASA trap wing, which is also the test model in the 1st AIAA High lift Prediction Workshop (HiLiftPW-1). Aerodynamic predictions in this paper will mainly focus on the near stall situation with high AoA, which can usually show stall characteristics.

1.3 Major Activities

The whole project process will include activities from literature review, mesh generation to result analysis. The specific objectives are shown as follows:

- Review of Literatures of High Lift Prediction Workshop and papers related to flow simulations over high lift configurations by RANS and DES model. Previous contribution towards high lift flow prediction will be summarized and compared.
- Numerical simulation of the chosen geometry of NASA trap wing. Several steps will be taken to obtain the flow solution, including mesh creation with Pointwise software, grid convergence study, flow simulation carried out with S-A, $k-\omega$ SST and DES model in ANSYS Fluent software.
- Prediction results analysis for several flow characteristics including but not limited to pressure coefficient, skin friction, drag, lift and moment coefficient. Comparison study will be carried out among all three models.
- Summary of contribution of the paper and discussion of future works to be done.

2 Literature Review

This chapter is aimed to achieve following objectives: a) Introduction of high lift devices. b) Flow feature over airfoil at high angles of attack such as massive separation, flow transition, reattachment, unsteady effects, etc. c) The AIAA high lift prediction workshop, including a brief background of the workshop, the geometry (NASA trapezoidal wing) provided and summary of CFD results. d) Study of turbulent models used to explore the prediction of high lift flow physics and its application. e) Challenges that the current-generation CFD technology is facing to for high lift flow prediction. f) Summary of all the contents above.

2.1 High lift Devices

To gain more lift of a wing, there are generally two ways: one is to increase the suction by increasing the airfoil camber or rising the angle of attack, and the other is to delay or prevent the massive separation. Airfoil camber usually can be increased by applying a device such as trailing-edge flaps, and commonly the separation can be delayed by leading edge flaps, slats or slots with some boundary layer control. All devices mentioned above are collectively called “mechanical high lift devices (or unpowered)[5]”. Another high lift devices designed for vertical or short take-off/landing is called powered high lift devices. Powered high lift devices mean aircraft engines exhaust that are shaped or directly used to modify the flow field over the wing. One example of that is blown flaps (or jet flaps), detail of which will not be further discussed in this chapter.

The purpose of trailing-edge flaps is to produce extra lift by adding aft camber and sometimes chord length through deflection around several hinges, in other words, being bent into airflow at expected angles. Trailing-edge flaps are cataloged into four basic types including plain flap, split flap, slotted flap and Fowler flap. There are also some other flap architectures been designed and developed based on the four basic types, such as Junkers flap, Gouge flap, Fairey-Youngman flap, Zap flap and Gurney flap, which are used on some specific military birds instead of being in widespread use.[6]

According to Anderson, separated flow usually comes from a loss of kinetic energy and causes an increase of pressure drag and substantial loss of lift[7]. Hence, to resist flow separation, a turbulent boundary layer is a better choice than a laminar one because turbulence means higher energy inside. To energizing the boundary layer, separation delayed devices are developed such as boundary layer control, slats, slots and leading-edge flaps.

2.2 Characteristics present in flows over high lift configuration

Due to increasing wing loading and larger lift range covering the entire flight envelope for modern aircraft including the cruise and low-speed condition, high lift devices are designed to meet the challenge. Moreover, to reach higher lift demanded, the airfoil shape needs to be optimized through the way of fully understanding of the flow characteristics over multiple elements of the high lift devices. Figure 2.1 shows a sketch of flow physics over an airfoil with three elements (leading edge slat, main wing and trailing-edge flap).

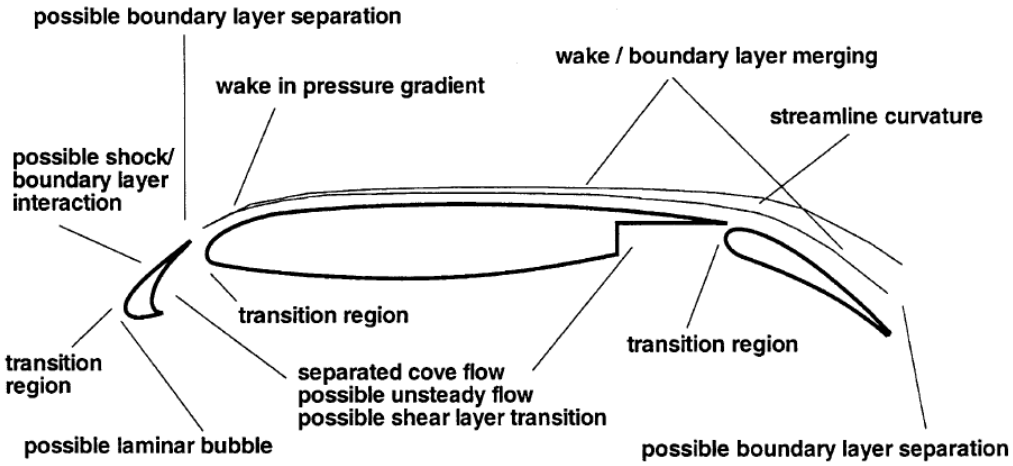

Figure 2.1 Physics of high lift flow over three-element airfoil [3]

For each element, there exists a boundary layer and interaction of boundary layer and wake from previous element over wing region and flap region. Those together come into merging a flowfield with complex velocity profile called confluent boundary layer (CBL). CBL usually extend 20% chord from the upper surface at high angle of attack into the flowfield[8]. CBL can endure pressure rise with wake disturbing the high adverse pressure region to avoid separation due to the

impressive interaction of the inviscid and viscous effects. Also, Thomas and Nelson[9] found out from experiments that lift performance can be improved by changing slat position as the gap between the slat and the main wing can affect the confluent boundary layer position. If the gap is too large, leading-edge separation forms with a reduced lift. And if the gap is too small, the lift will be cut down as well because of the confluent will be closer to the fore main wing, and an early CBL will lead to a momentum loss and an increased momentum thickness.

Other flow features can also be observed such as laminar bubble, transition regions for each element, and possible shock/boundary layer interaction if Mach number reach the requirement. However in this paper, flow condition for Mach number is 0.2, which is far from the formation criterion of shock wave, thus physics related to shock wave will not be discussed below.

2.3 The AIAA CFD High lift Prediction Workshop

2.3.1 Brief Background

The CFD High lift Prediction Workshop is aiming to provide an opportunity to bring all CFD experts together and to exchange the experience of CFD coding and modelling techniques. The workshop launched several long-term development tasks in CFD engineering, including the assessment of CFD prediction capability, development of modelling guidelines for high lift prediction, enhancement of high lift flow physics understanding, exploration of CFD prediction for future design and optimization and identifying area that needs additional study and development. The 1st AIAA CFD High lift Prediction Workshop was held at Chicago in 2010, while the 2nd workshop took place at San Diego in 2012 and the 3rd at Denver in 2017 associated with AIAA Aviation and Aeronautics Forum and Exposition. The geometry provided for research in three workshops are NASA Trapezoidal Wing, EUROLIFT DLR F11 and JAXA standard model respectively. Only NASA trap wing will be focused on in this paper.

2.3.2 NASA trapezoidal wing

The geometry provided by the 1st workshop is based on NASA trapezoidal wing, a swept, high aspect ratio, and three-element configuration attached to a body pod, including a leading slat, a main wing and a trailing-edge flap. The trap wing model was firstly tested in the Langley 14*22 wind tunnel in 1998 to explore some basic flow field information including force/moment and surface pressure, which covered a range of configurations and Reynolds numbers[10]. The second test was carried out in 2002 in the same place, which mainly focused on the more detailed flow physics data such as dynamic pressure, total and static pressure, turbulence intensity, and temperature over the landing configuration (config 1). The 2003 test added particle imaging velocimetry (PIV) method for the off-body velocity field measurements. The models installed then were illustrated in Figure 2.2 and 2.3 below.

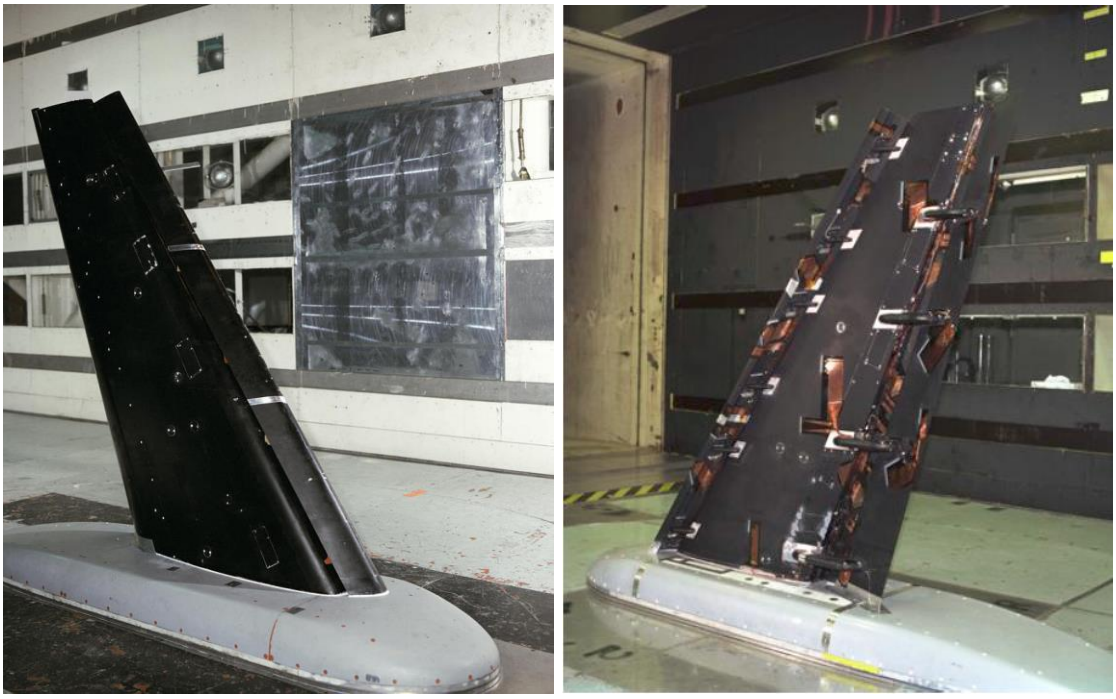

Figure 2.2 NASA trapezoidal wing model tested in 14*22 wind tunnel in 1998 (left) and 2002 (right) [10]

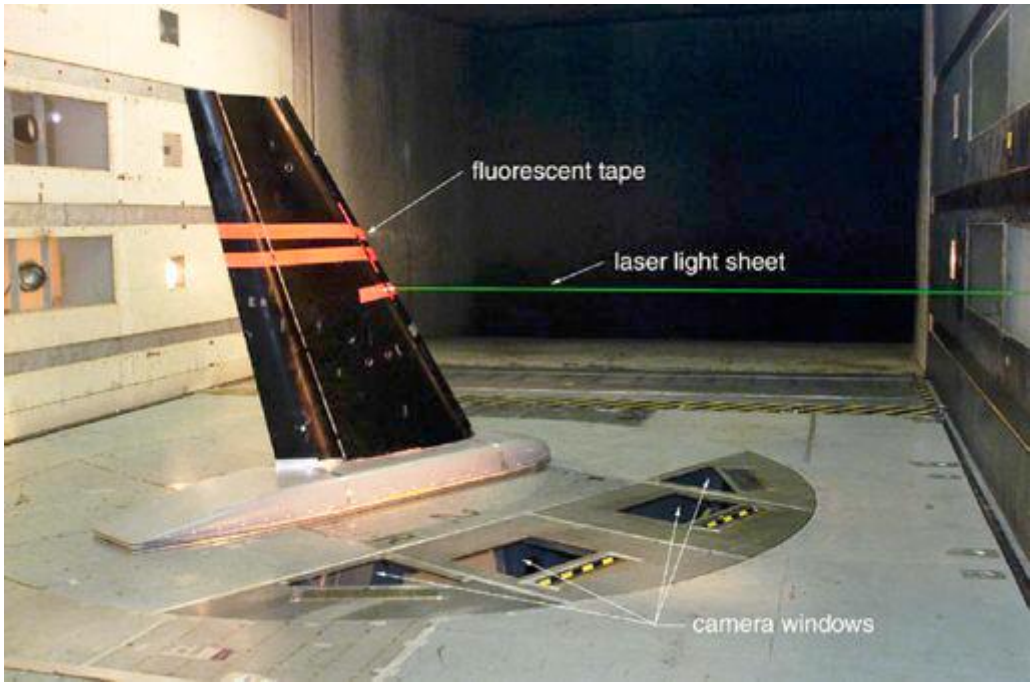

Figure 2.3 NASA trapezoidal wing model tested in 14*22 wind tunnel in 2003 [11]

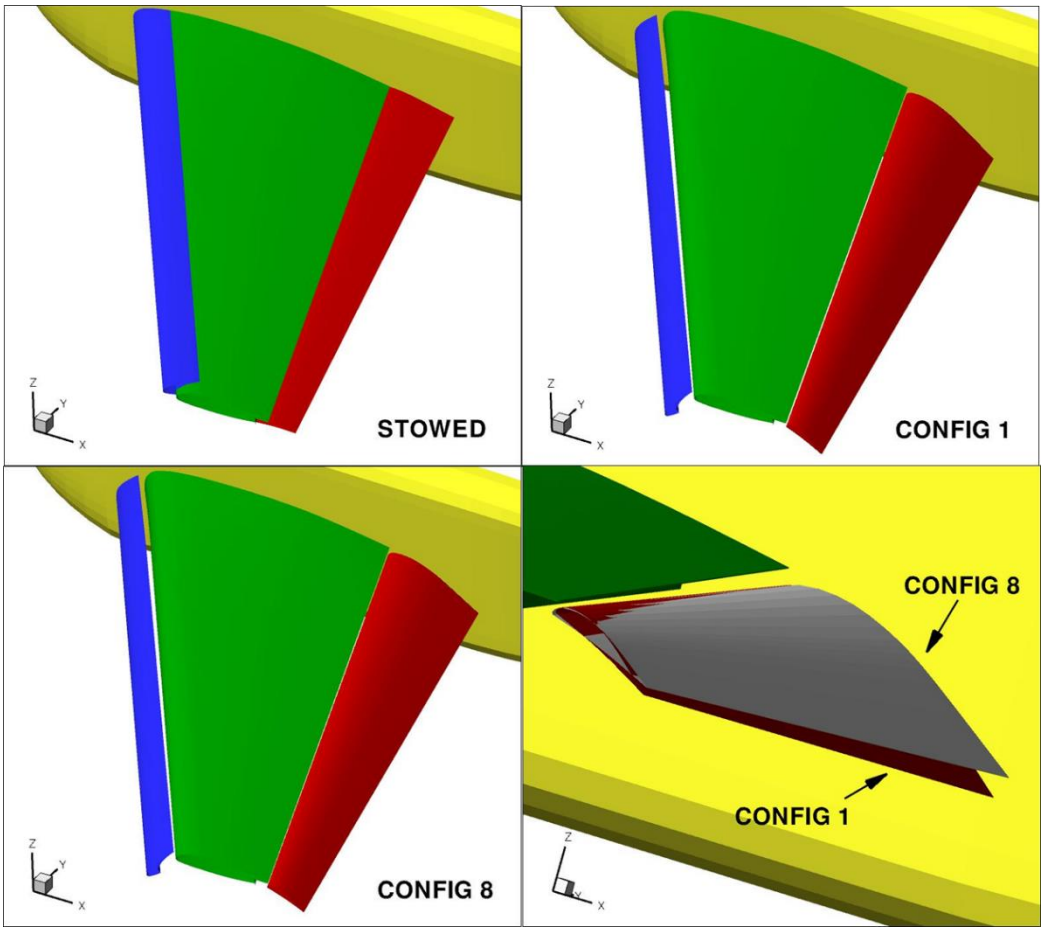

Figure 2.4 Three forms of NASA trapezoidal wing [12]

Three deployed slat and flap positions were studied in the workshop and displayed as stowed, configuration 1 (slat with deployed angle of 30 degrees and flap with deployed angle of 25 degrees) and configuration 8 (slat with deployed angle of 30 degrees and flap with deployed angle of 20 degrees), the differences of flap details can be observed in Figure 2.4. In this paper, only the flow feature over the geometry of configuration 1, which is also the landing configuration, will be calculated and discussed. All the related experimental data are based on the tests from 1998, 2002 and 2003. The trap wing geometric reference parameters is listed in table 2.1 below.

Table 2-1 NASA Trapezoidal Wing CFD Reference Parameters

Reference Area	22.028 ft^2
Mean Aerodynamic Chord	39.634 in
Semi-span	85.054 in
Aspect Ratio	4.561
Leading Edge Sweep	33.9 deg
Moment Reference	x=34.342 in y=-0.95 in z=0 in

2.3.3 Summary of the 1st AIAA High lift Prediction Workshop

Some statistics CFD results of the 1st AIAA CFD High lift Prediction Workshop (hereinafter to be referred as HiLiftPW-1) will be summarized in this section. In HiLiftPW-1, There were in 39 entries from 21 individuals/groups in total and the most frequently used turbulence model is Spalart-Allmaras (SA) model (21 entries) and Menter's shear stress transport (SST) model (7 entries), variant and special versions were included. In force and moment curves, collective results showed that only a few of outliers fell out of the average range and

underpredicted the lift, drag and moment coefficient at high angles of attack, which may be due to the CFD code sensitivity to initial conditions[4]. Some participants also mentioned that the converged solutions at lower angles of attack can be considered as an initial condition at high angles of attack, which is proved to be an effective way to avoid the premature stall and massive separation[13]. Generally, the S-A model is leading to higher lift coefficient than other models. As for grid effects, it has been found that unstructured tetrahedral grid is more sensitive than those with boundary layers merged from tetrahedral into prisms[14]. Also, flow field around wing tip exhibits a lot of challenge for accurate prediction, especially for those entries who choose to neglect the viscous cross-derivative terms instead of using full Navier-Stokes equation[15]. That leads to a large negative impact on surface pressure distribution over wing tip area.

2.4 Turbulent Models & Previous Works

Here in this subsection, RANS models and DES model together with their application in the previous AIAA High Lift Prediction Workshop series will be discussed and summarized. Findings of turbulent models contribution in high-lift flow prediction will also be highlighted and abstracted.

2.4.1 RANS

As the most commonly used method, Reynolds Averaged Navier-Stokes (RANS) is a methodology in which the fluctuating quantities of the flow are replaced with Time-averaged term and fluctuating part. Usually, RANS method includes $k-\varepsilon$ model, $k-\omega$ model with two equations, Spalart-Allmaras model with only one equation and Reynolds stress model with seven equations, which are indeed more economical than DES and LES. However, since RANS is based on time-averaging, it can only obtain the time-averaging mean value. Relatively, it is a better choice of LES or DES when the variation with time of the velocity vector is needed, as both the method is time-dependent, which can accurately model turbulence at utmost so far.

According to the overviews and summaries of the previous three workshops, RANS models are the most commonly used methods for high lift prediction,

especially for S-A model, $k-\omega$ and their variant version. In the 1st AIAA High lift Prediction Workshop, 25 out of 39 entries used S-A model, and 9 of the rest used $k-\omega$ model[4].

However, some of the participants tried to improve the prediction results by adjusting the wing tip vortex simulation. Eliasson et al.[16] used flow solver Edge with both thin-layer approximation (only normal derivatives) and full viscous operator (both normal and tangential derivatives) that respectively applied on S-A model. Results show that for pressure distribution at outermost station of 98% span, both methods reduce the gap between computed and measured data, with full viscous operator giving more considerably improvement, leading to a good wing tip flow solution. Furthermore, in his later investigation, Eliasson applied an approach of positioning the transition location by finding appropriate N-factors for the e^N method with S-A model[17]. Results seem to delay the lift break down as well as reduce the pitching moment, both bring a significant improvement compared to the fully turbulent calculations.

The German Aerospace Centre DLR also made contribution to the HiliftPW-1 by testing three different RANS model, (S-A, Menter SST and a Reynolds stress model called SSG/LLR-ω developed by DLR) with their own flow solver, TAU[14]. Unstructured grids have been created by two different mesh generation packages, Centaur and Solar, solutions from both have been compared to each other. Here in their research, results suggest that both packages shows some similarity in drag prediction. For lift curve at high incidence, Solar shows some early break down and under-prediction while Centaur shows a bit over-prediction but identical critical angle of attack with measured data. Among three RANS models, only S-A shows a fair agreement with experimental results. The shortcoming of SST and SSG/LLR-ω model can be speculated as some insufficient grid resolution at the wingtip region.

As a whole, conclusions for HiliftPW-1 can be drawn that RANS model performs well in flow prediction, but some entries presented the issues that RANS generally underpredicted lift and drag coefficient. Meanwhile, pressure distribution at wing tip region was far away from the experimental results due to massive separation

happens[18][19][20]. Moreover, as mentioned in 2.3.3, RANS cannot reach the experimental results of stall angle of attack unless the high angle of attack case was initialized with the converged lower angle of attack results.

As for flow simulation of the DLR-F11 wing at 2nd AIAA High lift Prediction Workshop, more untraditional methods were pulled in such as Wall-modelled large-eddy simulation (WMLES) and very-large-eddy-simulation (VLES) with Lattice Boltzmann code[21]. S-A model and its variant are still the most commonly used simulation method. However, as the geometry for HiLiftPW-2 brought more challenge compared to HiLiftPW-1 like slat brackets and flap fairings, the solution of a case with brackets appeared to be not as good as the clean model case. From three angle of attack case of 7, 16 and 21 degrees, the 7-degree case is underpredicted while 21-degree case is overpredicted.

Moreover, Mavriplis et al. from Bombardier Aerospace[22] found out that S-A is less sensitive than SST model on grid density, different grid generated by different mesh generator and cell type (prismatic-tetrahedral mesh with different prisms proportion). In their research, two grids sets are employed, one is generated by VGRID from workshop, and the other is based on the best practice by ICEM from Bombardier. Taken together, k-ω model with ICEM grid leads to a best performance in stall region and the best post-stall performance is achieved by k-ω model with VGRID grid. Observed from oil flow patterns, conclusion can be drew that the flow separations result from slat brackets.

Rudnik et al.[23] summarized the DLR's contribution in HiliftPW-2. This time, only Solar package was applied in mesh generation, with TAU code and S-A model solving the flow performance. A good agreement is observed for S-A model computations and experimental data for midboard pressure distribution for both low and high Reynolds number cases at AoA = 16°. Also, lift curves of configurations of different complexity are studied for comparison, including clear wing/body configuration (stage II), stage II with slat tracks and flap track fairings (stage IV) and stage IV with slat pressure tube bundles (stage V). Analysis shows that slat tracks and flap track fairings did not cause a lift reduction as a

disturbance compared to clear configuration, while pressure tube bundles exert distinct effects on early lift breakdown.

Chitale et al. [24] carried out an anisotropic boundary layer mesh adaptive method based on Hessians, which is only applied in an extra coarse grid. In comparison with the other mesh, the adapted mesh solution shows performance on par with medium mesh, even fine mesh in capturing wing tip vorticity. As unsteady RANS model with Spalart-Allmaras is used, effect of different time step is taken into consideration at high angles of attack. Higher C_L can be reached when the time step is reduced from 1e-4s to 1e-5s.

Lee-Rausch et al. also studied about mesh adaptation to solve the early separation problem. Their research focused on S-A model with output-based mesh adaptation, which requires the solution of the governing flow equations and the corresponding discrete adjoint equations. Flow analysis from the adapted medium grid indicated that this method can improve the situation of under-prediction of C_L at high incidences and reduce the reserved flow at flap trailing edge, but no significant improvement is shown for pitching moment. Except for origin S-A model, a rotation variation of S-A model is also used, and the result showed the variation model improved the prediction of pressures at wing tip region.

JAXA (Japan Aerospace Exploration Agency) employed two different CFD flow solvers in HiliftPW-2[25], UPACS code and TAS code for structured grid and unstructured grid respectively, and the former is developed by JAXA. Furthermore, two variant RANS models are applied and denoted as SA-noft2-R and SST-V. Also, to capture the secondary flows at wing-body juncture corner, an extra model called QCR2000 from Spalart is added on the two variants, respectively. Results show that S-A predicts higher C_L value and lower pitching moment than SST, while also SST shows early separation on flap outboard region. The introduction of QCR2000 shows identical effect for all the turbulence models, which decreases the lift value and cause an earlier separation.

Coder used OVERFLOW solver to predict high-lift flows over DLR-F11 with SA eddy-viscosity model and Menter SST model[26]. Moreover, effect of Spalart-

Shur rotation correction and flap brackets, as well as influence of two transition models are studied. From the analysis results, none of the model combination can accurately predict the lift curve, but SST with Langtry-Menter transient model shows a best overall performance for the stall pattern among all, which is unexpected due to SST model's inferior prediction ability to S-A model in general. Besides, brackets off condition can increase the suction peaks at flap.

In summary, in HiliftPW-2, RANS model did not show any clear trend for results of flow characteristics due to too many different but specific codes applied to the model from the entries, yet all the RANS results fall within the range of the scatter limits of workshop collective results with the coefficient of variation decreases with the increasing grid density. The most used RANS model is still S-A and its variants, which is 32 out of 48 entries, while 8 other entries chose Menter SST model, which could be caused by the experience from last workshop. Based on discussion above, S-A model and its variant show a better performance in lift curve prediction at high AoAs in most cases compared to SST model. But still, a small part of participants got the results that Menter SST model predicts a better stall pattern. Also, mesh adaption effect is investigated by some entries, which contributes in capturing the wing tip vorticity and reducing reversed flow over flap trailing edge. Moreover, brackets are proven to plays an important role in high-lift flow prediction, the inclusion of brackets usually causes a reduction of suction peaks in pressure distribution.

For the third AIAA High-Lift Prediction Workshop, two geometries are determined for different test cases, one is NASA High Lift Common Research Model (HL-CRM) for grid convergence test and the other is JAXA Standard Model (JSM) for nacelle installation study and turbulence model verification study. Furthermore, according to the experience from previous workshops, no consistent results are shown as different codes are used for turbulence models. Hence, an additional case is required to verify the consistency of 2-D near-wake flow performance with different model variant. Since the HiliftPW-3 was held in 2016, papers from most participates have not been published yet, the summary will mainly focus on the results analysis from presentation they displayed and published by the workshop.

Same thing happened in HiLiftPW-3 as nearly all participant chose RANS for their prediction model. More and more entries apply their own code to the original model, which lead to great inconsistency of the results but still stay in a range around experimental data. Some participants compare different turbulence models to figure out model effect. Glasby and Erwin[27] compare several RANS models such as S-A, Menter SST and Menter transition model with KCFD solver. For lift curve, Menter transition model shows a great agreement with experimental for both linear and stall part. Both S-A and SST show an early separation, while S-A breaks down earlier than SST. Also, from CP contour, facts can be observed that S-A solutions have large mid-span separation instead of small separations behind slat bracket region for Menter SST, which can be equally seen in CP plot at the same position with an underprediction of suction peak for each element. Luo and Lee[28] also make a comparison of S-A negative and k-omega SST model, but their study drew a conclusion opposed to Glasby that k-omega SST predicts an early separation as well as lower lift even at linear part.

One other thing that deserved to be discussed about is an S-A variant called QCR, which is proposed by Spalart[29] and explained as Quadratic Constitutive Relation, using a new turbulent stress to replace the traditional linear Boussinesq relation in the original S-A model. Seven of the entries choose to use this variant for high-lift prediction, as its capability in reducing side-of-body separation according to JAXA's research from HiliftPW-2. Take JAXA's research in Hiliftpw-3 for example[30], case with and without QCR is compared, while the results show that the inclusion of QCR leads to a deviation of lift at latter linear part and improvement of pitching moment. From oil flow images, the addition of QCR causes a large separation from slat track, which region considerably expands as the increase of incidence. Jensen et al.[31] studied the difference between S-A and SA-QCR2000 model in their research, outcome can be observed that QCR2000 improve the lift and moment results, but still being under prediction with the measured data. From pressure distribution at midboard, clearly QCR2000 reduce the section peak at slat leading edge at critical AoA, but good agreement is achieved in the following two elements.

In conclusion, similar to the situation happened in Workshop 2, no consistent results are shown as different codes are applied for turbulence models. Reasons can be found that may make those situation happen such as unintentional bugs or insufficient grid refinement. Despite same turbulence model or variant can be chosen, different flow solvers will lead to different outcome, not to mention the grid generation practice. To figure out this problem, HiLiftPW-3 require an additional case for code verification. However, collective results from only S-A model (not enough results from other models) shows that S-A model with verified code can improve the consistency to a great extent, but solution consistency near C_{Lmax} is still under challenge.

In summary, for all three High Lift Prediction Workshops, RANS model is most commonly used for flow prediction over high lift configuration for its accuracy under cost-effective performance in time and computational resources. Nowadays, Codes has been added in RANS method to explore the capacity in precisely capturing flow characteristics, but still, it failed in predicting the flow near stall area. Among all the RANS model cases, S-A model and its variant is the most popular choice, while sometimes Menter SST model shows satisfactory solution as well. However, as the increasing geometry complexity such as the inclusion of slat and flap tracks and pressure tube bundle in HiLiftPW-2 and nacelle in HiLiftPW-3, RANS model performance is no longer in good agreement with the experimental data as in HiLiftPW-1. Finally, as the rapid development of massively parallel computers and workstation cluster, maybe it is time to shift the emphasis to a better performance but a little higher time-consuming model.

2.4.2 Detached-eddy Simulation (DES)

From introduction above, RANS is considered not suitable for solving flow with mass separation properly for its poor performance while LES is appropriate enough but too time/computational-costly in calculating boundary layers. In this circumstances, the hybrid RANS/LES method has been developed and proved precise enough for predicting unsteady effects and geometry-dependent separation in transonic flows. Detached-eddy Simulation (DES) is a combination of RANS and LES, namely, RANS method near the wall deal with small-scale

motion and LES far away from the wall deal with large-scale motion (especially in the separation region). DES was first proposed in 1997 and first put into use in 1999[32], which was created to challenge the high Reynolds number flow case, especially those with massive separation.

DES97, as the very original version of DES, is created and based on Spalart-Allmaras model as the single turbulence RANS model for grids not fine enough for large eddy simulation, and the subgrid-scale model for regions where it is[33]. The switch of RANS and LES model depends on the grid density. The length scale, which is the distance to the closest wall *d* in RANS model, is substituted into a new length scale $\tilde{d}$ in DES as in Equation 2-3[34]:

$$\widetilde{\boldsymbol{d}} \equiv \boldsymbol{min}(\boldsymbol{d}, \boldsymbol{C_{DES}}\Delta) \quad \textbf{(2-1)}$$

where the model constant C_{DES} is to be decided but empirically 0.65 and Δ depends on the largest dimension of the grid cell.

$$\Delta \equiv \boldsymbol{max}(\Delta \boldsymbol{x}, \Delta \boldsymbol{y}, \Delta \boldsymbol{z}) \quad \textbf{(2-2)}$$

In most cases, the interface of RANS and LES model locates outside the boundary layer region, but it will move towards the wall as the grid refinement being applied, which will cause the length scale switch to LES mode.

However, as a new arise numerical model, there must be some weaknesses and inadequacies for DES. Moreover, for further extended, DES has been improved in several directions: the adaption of two-equation RANS model, Zonal Detached-eddy Simulation (ZDES), Delayed Detached-eddy Simulation (DDES) and Improved Delayed Detached-eddy Simulation (IDDES)[32]. DDES was first developed because of some incorrect behaviours happens at regions between the boundary layer and flow separation when DES was used to prediction separated flows. While grid is refined to achieve the DES length scale, the grid spacing parallel to the wall $\Delta_{||}$ will be less than boundary layer thickness δ. Therefore, the resolved Reynolds stresses of LES and modelled Reynolds stresses of RANS at interaction region do not match with each other and led to a depressed value of Reynolds stresses. Premature separation caused by that means rather than reaching the LES precision level, the solution is even less

accurate than RANS. DDES is modified on the basis of DES to solve the problem above, namely, grid induced separation (GIS). In DDES, blending functions of SST model was used to shield the boundary layer[35]:

$$\widetilde{\boldsymbol{d}} \equiv \boldsymbol{d} - \boldsymbol{f_d max}(\mathbf{0}, \boldsymbol{d} - \boldsymbol{C_{DES}}\Delta) \quad \textbf{(2-3)}$$

Where f_d is a function of wall distance and is related to kinematic eddy viscosity, In near-wall region, $f_d = 0$, which means RANS length scale is preserved in that region no matter which has a smaller length scale, RANS or LES. Thus, the LES processed has been delayed to avoid the separation.

DDES can also be considered as Wall-modelled LES if near-wall turbulent region is resolved by RANS model. However, problems showed as the modelled log-layer produced by RANS and resolved log-layer produced by LES model do not match with different intercept C (as in $U^+ = log(y^+)/\kappa + C$) and turned out mismatched. This issue is called Log-Layer Mismatch. Under the motivation of solving the problem, IDDES was built by Shur et al. [36]. IDDES is a hybrid of WMLES and DDES, which can switch between DDES and WMLES as a specific condition without producing LLM. The detail principle and functions of IDDES will not be introduced in this paper.

The alternative of more complex RANS model in DES will lead to a more accurate solution to the boundary layer, which is critical for flow simulation. A more user-friendly method called ZDES is developed as it supports a user-defined zone for RANS and LES. ZDES has also been widely applied in aerodynamic physics research. Brunet and Deck[37] perform the simulation of a transonic buffet on a half-body rigid model, where ZDES accurately predicts the whole mean field especially the shape of the separated area.

DES has been applied and proved to have good performance in a variety of research fields in the past. such as the transonic cavity flows prediction[38][39][40][41], high lift configuration[42][43], transonic flow over supercritical airfoil and delta wing, flow over a circular cylinder[33][44]. In this subsection, we will mainly talk about aerodynamics simulation for flow over a three-dimensional airfoil, which is also the research direction of this paper.

As a new hybrid turbulence model to accurately predict the flow over high lift configuration, DES was not explored until HiLiftPW-2. Only two teams attempted to use DES method during the DLR-F11 configuration high lift prediction and results have shown that DES mode in both of them have got a better agreement with the experiment than RANS model. It should be mentioned that DLR-F11 features a complete span slat and flap with 7 slat tracks and was chosen due to there is reliable wind tunnel test data obtained in the framework of the EC-Project EUROLIFT.

Escobar et al.[43] investigated to improve the stall regime prediction using a hybrid RANS-LES model (DES based on SA). Flow conditions in the European Transonic Windtunnel (ETW) test with DLR-F11 model is an average Mach number of 0.176 with an average Reynolds number of 15.1 million and average total pressure and temperature of 301560Pa and 114.7K respectively. The angle of attack ranged from -3.2 deg to 24.24 deg. For comparison, the original coarse mesh was computed with SA model together with an adapted mesh computed with DES. Results showed a significant improvement prediction of DES in pressure distribution except for some failure pressure coefficient increment description at 15% and 44.9% wingspan. Moreover, DES failed to prediction the stall, which can be explained that all the simulation were carried out the inclusion of slat tracks. However, DES and its corresponding grid refinement lead to higher values of turbulence viscosity ratio, which is in agreement with the capability to capture smaller eddies in the flow field where the LES mode was activated.

Different with Escobar et al. using ANSYS Fluent v14.5, a parallel solver called PHASTA was applied in the simulation of Rasquin et al.[42]. An initial mesh was first computed with both URANS and DES to figure out the mesh detail location that needs to be refined for adaption, such as the wakes of the slat, main wing, flap, slat track fairings and flap track fairings. After mesh adaption, DES proved to perform better prediction and significant improvement at key locations and those wake mentioned above, and the pressure distribution matches perfectly from the root to the two-thirds of the wingspan after mesh adaption. For further better agreement, more resolution will be required in the vicinity of the fourth and

fifth flap track fairings as well as the most flap flow control simulations for the DES simulations, which should be considered in the future work.

In conclusion, DES can also handle the high lift flow prediction, with considerably improvement at key locations and wakes for each element. Also, flow details such as small eddies can be captured more specifically by DES.

2.5 Summary of Literature Review

As can be seen from previous sections, the numerical prediction for flow over high lift devices is still facing two challenges waiting to be solved as follows:

The first challenge is that the complexity of flow physics present in flow over simple airfoil makes it very hard to get fully predicted, not to mention the additional features emerge and interact with each other over a multi-element wing. Also, massive separation at angles of attack near stall has been a nodus to be overcome all the time since the origin of computational fluid dynamics.

The second challenge is exploring the perfect turbulence model that meets the request of both the computation accuracy and economical cost. To figure out this problem, previous works from previous three AIAA CFD High Lift Prediction Workshop are discussed, analyzed and summarized. As far as we know from the previous work, S-A model is satisfying in the solution of adverse pressure gradient flows in boundary layer and computational efficiency due to only one transport equation involved during computation. However, without any variant, S-A alone cannot resolve the eddies arise after the massive separation. Even though S-A with variant can only do limited improvement to stall prediction.

As for $k-\omega$ model, it performs well enough if high accuracy boundary layer simulation is required, and is able to handle more complex geometries than S-A model because of its advantage in vortices and swirl flows prediction. But it seems to overpredict separation and underpredicts lift coefficient even more than S-A model, which leads to a failure of prediction at stall region as well. However, from the previous High Lift Workshop entries experience, sometimes Menter SST model gives a best performance in stall pattern prediction compared to other RANS models.

LES has been tested accurate enough in high lift prediction, however, it is not mature enough as a routine basis prediction tool, which leads to wall-modelled LES and DES. Both methods show great improvement in flow prediction, while the latter has a greater development prospect in airfoil design application and an increasing ability to handle cases with high Reynolds number conditions. DES has been proved to achieve good performance in most cases of geometry-dependent massive flow separation and unsteady effects prediction compared to RANS and LES respectively. Although DDES, IDDES and ZDES are still being explored to fix the problem brought by DES such as Grid Induced Separation and Log-Layer Mismatch, DES is accurate enough to handle the separation for most geometries at high angles of attack, but wake at key locations needs more exploration, especially for near stall.

Thus, in consideration of both advancing prediction commitment, performance assessment of stall prediction and model capability exploration, original S-A, Menter k-ω SST and DES model are chosen in this project for flow prediction over high lift devices.

Another significant feature from the previous three high-lift prediction workshop is the unstructured mesh has become dominant gradually. The reason why this happened can be inferred that the unstructured mesh reduce the computational effort when compared to structured mesh. Also, with the growing of geometry complexity, only unstructured mesh can take care of all the details of geometry such as the slat and flap track fairings, pressure tube bundle as well as the nacelle in HiLiftPW-3. All of those mentioned above are almost impossible to be constructed by structured mesh. Thus, unstructured mesh can be inferred to become more mainstream in CFD prediction in the near future, both economical and feasibility.

3 Methodology

To achieve the objectives listed for this project, the whole simulation process will roughly be divided into three steps. To briefly summary, the first step would be the generation of geometry and creation of mesh using Pointwise. Secondly, once the mesh file is examined fine tested for its independence it will be exported as case file and imported into ANSYS Fluent for case setup respectively by S-A, k-ω SST and DES model. Then the case will be uploaded to Delta (the high-performance computer in Cranfield University) as well as the journal file and submission file for computing. Finally, the results will be exported, processed and plotted by both Tecplot 360 and Microsoft Excel.

Software used during the project:

- Pointwise
- ANSYS Fluent
- ANSYS CFD-Post
- Tecplot 360
- Microsoft Excel
- Engauge Digitizer

3.1 Governing Equation

The Governing Equations of fluid dynamics contains three equations: the continuity equation, the momentum equation and the energy equation, which corresponds to the following three laws of physics of fluid flow:

(1) Mass is conserved

(2) Newton's second law

(3) Energy is conserved

Firstly, mass conservation means for every fluid element, the rate of mass increase equals the net rate of mass that flows into it. Figure 3.1 shows the mass flow rate in three dimensions of the element, which leads to an equation as follow.

$$\frac{\partial \rho}{\partial t} + \frac{\partial (\rho u)}{\partial x} + \frac{\partial (\rho v)}{\partial y} + \frac{\partial (\rho w)}{\partial z} = 0$$

(3-1)

Eq. 3-1 is called the **mass conservation or continuity equations** for compressible fluid.

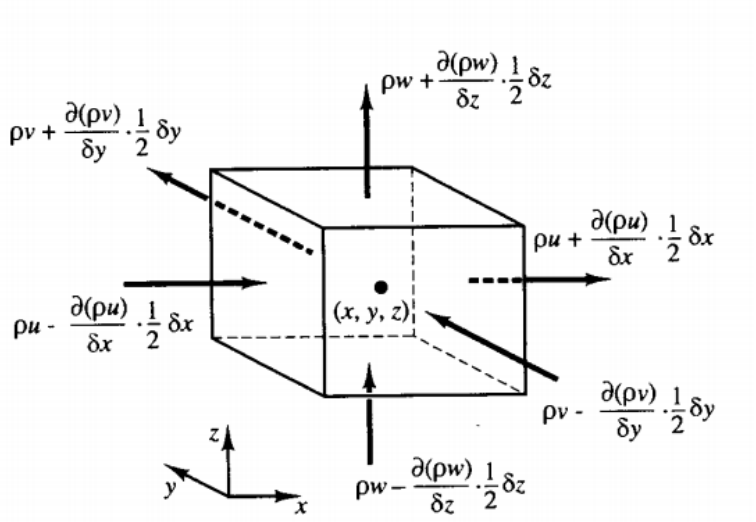

Figure 3.1 Mass flows in and out of fluid element [45]

For momentum equation, Newton's second law will be applied in Eq.3-2, forces (including pressure and viscous stress) acting on a fluid element in the x-direction are shown in Figure 3.2.

$$F_x = ma_x \tag{3-2}$$

As all the forces in x-direction add up to the product of mass and acceleration according to Eq.3-2, thus, the x component of the moment equation can be yielded as

$$\rho \frac{Du}{Dt} = -\frac{\partial p}{\partial x} + \frac{\partial \tau_{xx}}{\partial x} + \frac{\partial \tau_{xx}}{\partial y} + \frac{\partial \tau_{zx}}{\partial z}$$

(3-3)

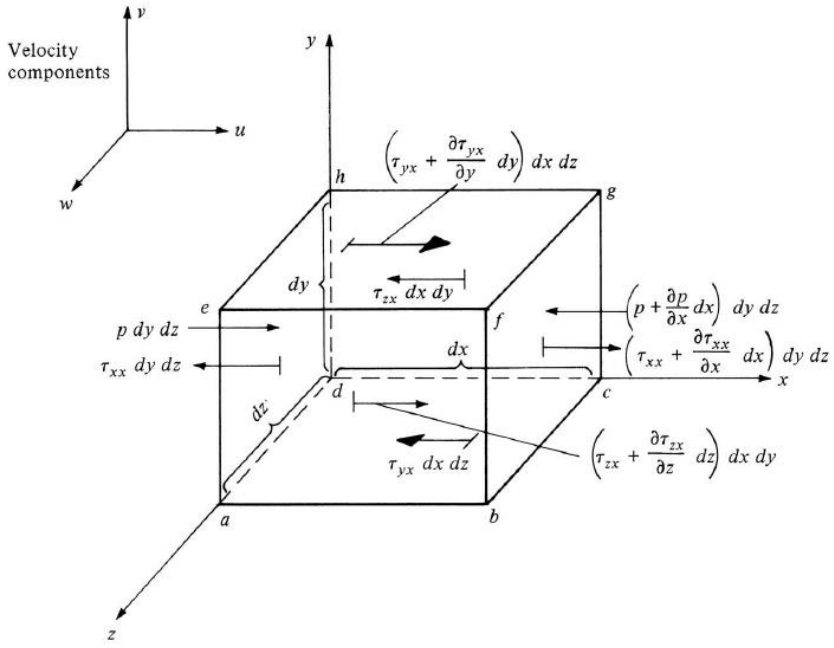

Figure 3.2 Forces act on fluid element in x-direction [7]

To complete the equation, the viscous stresses and acceleration can be further detailed, which makes the x-direction equation be written as

$$\rho\frac{\partial u}{\partial t}+\rho u\frac{\partial u}{\partial x}+\rho v\frac{\partial u}{\partial y}+\rho w\frac{\partial u}{\partial z}=-\frac{\partial p}{\partial x}+\frac{\partial}{\partial x}\left(\lambda\nabla\cdot V+2\mu\frac{\partial u}{\partial x}\right)$$

$$+\frac{\partial}{\partial y}\left[\mu\left(\frac{\partial v}{\partial x}+\frac{\partial u}{\partial y}\right)\right]+\frac{\partial}{\partial z}\left[\mu\left(\frac{\partial u}{\partial z}+\frac{\partial w}{\partial x}\right)\right] \quad \textbf{(3-4)}$$

Similarly,

$$\rho\frac{\partial v}{\partial t}+\rho u\frac{\partial v}{\partial x}+\rho v\frac{\partial v}{\partial y}+\rho w\frac{\partial v}{\partial z}=-\frac{\partial p}{\partial y}+\frac{\partial}{\partial x}\left[\mu\left(\frac{\partial v}{\partial x}+\frac{\partial u}{\partial y}\right)\right]$$

$$+\frac{\partial}{\partial y}\left(\lambda\nabla\cdot V+2\mu\frac{\partial v}{\partial y}\right)+\frac{\partial}{\partial z}\left[\mu\left(\frac{\partial w}{\partial y}+\frac{\partial v}{\partial z}\right)\right] \quad \textbf{(3-5)}$$

$$\rho\frac{\partial w}{\partial t}+\rho u\frac{\partial w}{\partial x}+\rho v\frac{\partial w}{\partial y}+\rho w\frac{\partial w}{\partial z}=-\frac{\partial p}{\partial y}+\frac{\partial}{\partial x}\left[\mu\left(\frac{\partial u}{\partial z}+\frac{\partial w}{\partial x}\right)\right]$$

$$+\frac{\partial}{\partial y}\left[\mu\left(\frac{\partial w}{\partial y}+\frac{\partial v}{\partial z}\right)\right]+\frac{\partial}{\partial z}\left(\lambda\nabla\cdot V+2\mu\frac{\partial w}{\partial z}\right)$$

(3-6)

Equations (3-4 to 3-6) are the **complete momentum equations** for unsteady, compressible, three-dimensional viscous flow.

Last but not least, the energy equations are also needed when describing fluid flow. According to the first law of thermodynamics, the change rate of energy inside a fluid element equals to the net flux of heat into the element plus the power done on the element due to the pressure and stress forces acting on surface. Hence, for intuitively understanding, Figure 3.3 simply illustrates the energy fluxes through a fluid element in x-direction.

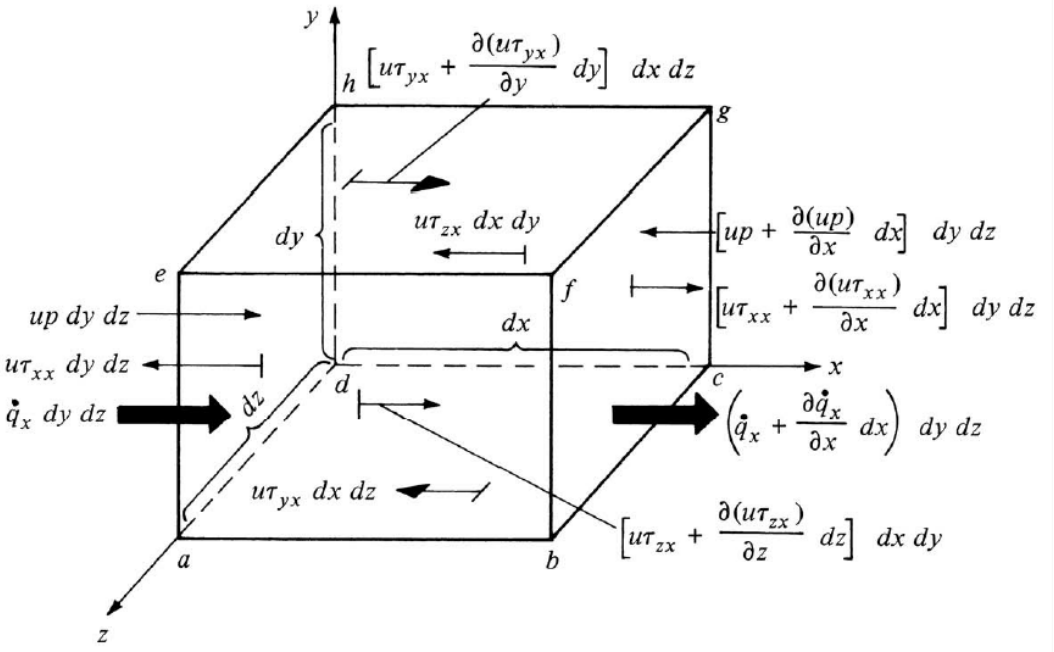

Figure 3.3 Energy fluxes of a fluid element in x-direction [7]

However, as the energy equation for incompressible flow can be decoupled from its continuity and momentum equations, and the flow studied in this paper is limited to a low velocity of 0.2 Mach number, thus, energy for compressible flow will not be deduced here.

Except for the equations above, every turbulence model will have additional transport equations and Reynolds stress terms for their own development. Further detail information of the turbulence model employed in this paper will be introduced in the next few subsections.

3.1.1 Spalart-Allmaras

Spalart-Allmaras model is a one-equation turbulence model for kinematic eddy turbulent viscosity $\tilde{\nu}$, which is first proposed by P. R. Spalart and S. R. Allmaras[46]. It is the most commonly used turbulence model for external aerodynamics prediction for its economical and good performance on computational of boundary layers.

The original S-A model from Spalart et al. have four different versions corresponding to different flow conditions independently: free shear flow, near-wall region at high Reynolds number, near-wall region at finite Reynolds number and laminar region with its trim term. Each version has its own transport equation. This paper focuses on the second version, with a destruction term that can accurately describe a log layer in a U^+/y^+ plot.

The one transport equation for $\tilde{\nu}$ is written as

$$\frac{\partial(\rho\tilde{\nu})}{\partial t} + div(\rho\tilde{\nu}U) = \frac{1}{\sigma_v} div\left[(\mu + \rho\tilde{\nu})grad(\tilde{\nu}) + C_{b2}\rho\left(\frac{\partial\tilde{\nu}}{\partial x_k}\right)^2\right] + C_{b1}\rho\tilde{\nu}\tilde{\Omega} - C_{w1}\rho\left(\frac{\tilde{\nu}}{\kappa y}\right)^2 f_w$$

I II III IV V

(3-7)

where

$$\tilde{\Omega} = \Omega + \frac{\tilde{\nu}}{(\kappa y)^2} f_{v2}$$

(3-8)

$$\Omega = \sqrt{2\Omega_{ij}\Omega_{ij}}$$

(3-9)

$$\Omega_{ij} = \frac{1}{2}\left(\frac{\partial U_i}{\partial x_j} - \frac{\partial U_j}{\partial x_i}\right)$$

(3-10)

And all the model constants mentioned in the transport equation above are shown in Table 3-1. Constants from the original Spalart's paper is the same as in Fluent software

Table 3-1 Spalart-Allmaras model constant

σ_v	κ	C_{b1}	C_{b2}	C_{w1}
2/3	0.4187	0.1355	0.622	$C_{b1} + \kappa^2 \frac{1 + C_{b2}}{\sigma_v}$

Every terms in Eq. 3-7 will be explained as follows

(I) Rate of change of viscosity $\tilde{\nu}$

(II) Transport of $\tilde{\nu}$ by convection

(III) Transport of $\tilde{\nu}$ by turbulent diffusion

(IV) Rate of production of $\tilde{\nu}$

(V) Rate of dissipation of $\tilde{\nu}$

For Spalart-Allmaras model in Fluent software, all the destruction, diffusion and production term are completely in accordance with the equation mentioned above in Spalart's original paper, including the empirical constant. There is one modification in Fluent with a user-defined source term added to the right side of the equation, which equals to zero by default. Besides, S-A model in Fluent has been extended with an Enhanced Wall Treatment within the whole boundary layer[47]. `

3.1.2 K-omega Shear-Stress Transport

K-omega Shear-Stress Transport (K-ω SST) model is first proposed by F. R. Menter in 1994[48], to solve the problem of two-equation models failing to predict separation flows. It is a variation on the basis of k-ω standard model and k-epsilon (k-ε) model, a hybrid model with near-wall region performed by k-ω standard model and fully turbulent region resolved by k-ε standard model, which is also able to account for the transport of the principal turbulent shear stress in adverse pressure gradient boundary layers according to Menter's research[49]. SST model shows better performance in adverse pressure gradient boundary layer flows prediction than the standard k-ω model and Spalart-Allmaras and meanwhile shows less sensitive to the freestream values.

The transport equation for ω will be like ε-equation but with ε being replaced by kω, as shown in Eq. 3-11.

$$\frac{D\rho\omega}{Dt} = \frac{\gamma}{\upsilon_t}\tau_{ij}\frac{\partial u_i}{\partial x_j} - \beta\rho\omega^2 + \frac{\partial}{\partial x_j}\left[(\mu + \sigma_\omega\mu_t)\frac{\partial\omega}{\partial x_j}\right] + 2(1-F_1)\rho\sigma_{\omega 2}\frac{1}{\omega}\frac{\partial k}{\partial x_j}\frac{\partial\omega}{\partial x_j}$$

(3-11)

where the eddy viscosity υ_t is a distinct from those in conventional two-equation models as in origin k-ε and k-ω model and defined as

$$\upsilon_t = \frac{a_1 k}{max(a_1\omega;\ \Omega F_2)}$$

(3-12)

where F_2 goes to one in boundary layer and zero in free shear flow.

And the transport equation for k is

$$\frac{D\rho k}{Dt} = \tau_{ij}\frac{\partial u_i}{\partial x_j} - \beta^*\rho\omega k + \frac{\partial}{\partial x_j}\left[(\mu + \sigma_k\mu_t)\frac{\partial k}{\partial x_j}\right]$$

(3-13)

in which the Reynolds stresses τ_{ij} are computed as

$$\tau_{ij} = -\rho\overline{u_i' u_j'} = \mu_t \left(\frac{\partial U_i}{\partial x_j} + \frac{\partial U_j}{\partial x_i} - \frac{2}{3}\frac{\partial u_k}{\partial x_k}\delta_{ij} \right) - \frac{2}{3}\rho k \delta_{ij}$$

(3-14)

Two sets of constant are used to calculate the equation, which is listed in table 3-2. From this table, constant set 1 with subscript 1 is used in Wilcox formulation at near wall region and it will switch to set 2 with subscript 2, which is used in k-ε standard formulation in the wake region of boundary layers and free shear layers. All the constants of the SST model from Menter's original paper are the same as in the SST model from Fluent software[50].

Table 3-2 k-ω model constants

Set 1	$\boldsymbol{\sigma_{k1}}$	$\boldsymbol{\sigma_{\omega 1}}$	$\boldsymbol{\gamma_1}$	$\boldsymbol{\beta_1}$	$\boldsymbol{\beta^*}$	$\boldsymbol{a_1}$
constant value	0.85	0.5	0.55	0.075	0.09	0.31
Set 2	$\boldsymbol{\sigma_{k2}}$	$\boldsymbol{\sigma_{\omega 2}}$	$\boldsymbol{\gamma_2}$	$\boldsymbol{\beta_2}$	$\boldsymbol{\beta^*}$	$\boldsymbol{a_1}$
constant value	1.0	0.856	0.44	0.0828	0.09	0.31

3.1.3 Detached-eddy Simulation

As mentioned in the previous section, Detached-eddy simulation is a combination of RANS and LES model. It is first proposed by Spalart et al.in 1997[34] hence known as DES97, as the LES model is so time-consuming that it is beyond the feasibility for the large area of thin boundary layers in engineering applications, and that is when DES rises in response to that pressing need. DES performs as RANS model near boundaries and switches to LES in a subgrid scale mode in the rest area, especially at separation. The word "detached" is relative to "attached eddies" from Townsend [51], which is used to describe the eddies within the boundary layer.

The new DES length scale $\widetilde{d}$, which is a substitution of distance to the closest wall d in RANS model, is shown as in Equation 2-3 and is repeated here:

$$\tilde{d} \equiv min(d, C_{DES}\Delta)$$

(3-15)

Which means

$$\tilde{d} = d \quad \text{if} \quad d < C_{DES}\Delta$$

$$\tilde{d} = C_{DES}\Delta \quad \text{if} \quad d > C_{DES}\Delta$$

where Δ is defined as the largest spacing among the x-, y- and z-direction in a grid cell. C_{DES} is an empirical constant, which is usually obtained from wind tunnel test, here in this paper is given a value of 0.65 for DES with the S-A model in Fluent software.

$$\Delta \equiv max(\Delta x, \Delta y, \Delta z) \quad \textbf{(3-16)}$$

In other words, for the grids in boundary layer region, Δy is far smaller than d. However, with anisotropic grids being applied, spacing in the other two direction can still be far larger than the distance. On the contrary, grids in massive separation region are more isotropic, which results in an S-A destruction term of $C_{DES}\Delta$ and behaves as an SGS model.

LES part in DES is regarded the same as LES method alone when used in a simulation, for both spatial and temporal resolution. For LES part, the velocity is separated by the filter into two component: filtered, resolved one and the residual, sub-grid scale one. Time-dependent flow field with the filtered velocity can be regarded as in large eddy motion.

The filtering function of LES is shown in Eq. 2-1 and 2-2, which will be repeated and renumbered here:

$$\emptyset(\mathbf{x}, \boldsymbol{t}) \equiv \iiint \boldsymbol{G}(\mathbf{x}, \mathbf{x}', \Delta)\emptyset(\mathbf{x}, \boldsymbol{t})\, \boldsymbol{dx_1' dx_2' dx_3'}$$

(3-17)

$$\Delta = \sqrt[3]{\Delta x \Delta y \Delta z}$$

(3-18)

There are three commonest forms of filtering function in 3-D LES simulation: Top-hat filter, Gaussian filter and Spectral cutoff filter. The latter two filters are more often used in research literature, especially the Gaussian filter, which has become the centre of research on LES as a turbulence modelling tool and is shown as follow in Eq. 3-19:

$$G(x, x', \Delta) = \left(\frac{\gamma}{\pi\Delta^2}\right)^{3/2} exp\left(-\gamma \frac{|\mathrm{x} - \mathrm{x}'|^2}{\Delta^2}\right)$$

(3-19)

Typical value for parameter $\gamma = 6$

Similar with the RANS equations, the filtered LES continuity and momentum equations can be seen as below from Eq.3-20 to 3-23:

LES continuity equation:

$$\frac{\partial \rho}{\partial t} + div(\rho\bar{u}) = 0$$

(3-20)

Compared to standard Navier-Stokes forms, the momentum equations for LES has additional term of residual stress tensor or SGS stress tensor, which come with the residual motion.

LES momentum equations:

$$\frac{\partial(\rho\bar{u})}{\partial t} + div(\rho\bar{u}\bar{\mathrm{u}}) = -\frac{\partial \bar{p}}{\partial x} + \mu div\big(grad(\bar{u})\big) - \big(div(\rho\overline{u\mathrm{u}}) - div(\rho\bar{u}\bar{\mathrm{u}})\big)$$

(3-21)

$$\frac{\partial(\rho\bar{v})}{\partial t} + div(\rho\bar{v}\bar{\mathrm{u}}) = -\frac{\partial \bar{p}}{\partial x} + \mu div\big(grad(\bar{v})\big) - \big(div(\rho\overline{v\mathrm{u}}) - div(\rho\bar{v}\bar{\mathrm{u}})\big)$$

(3-22)

$$\frac{\partial(\rho\bar{w})}{\partial t} + div(\rho\bar{w}\bar{\mathrm{u}}) = -\frac{\partial \bar{p}}{\partial x} + \mu div\big(grad(\bar{w})\big) - \big(div(\rho\overline{w\mathrm{u}}) - div(\rho\bar{w}\bar{\mathrm{u}})\big)$$

(3-23)

I II III IV V

It worth mentioning that all the overbar indicates spatial filtering instead of time-averaging. Each term in momentum equations can be explained as:

(I) Rate of change of the filtered three-dimensional momentum

(II) Convective of filtered three-dimensional momentum

(III) Gradients in x, y and z directions of the filtered pressure field

(IV) Diffusive fluxes of filtered three-dimensional momentum

(V) Sub-grid-scale stresses (caused by the filtering operation)

Subgrid-scale (SGS) stresses contains further contributions than Reynolds stresses, from which we should consider flow variable $\emptyset(\mathbf{x}, t)$ as

$$\emptyset(\mathrm{x}, t) = \overline{\emptyset}(\mathrm{x}, t) + \emptyset(\mathrm{x}', t)$$

(3-24)

where $\overline{\emptyset}(\mathbf{x}, t)$ is the filtered functions with resolved spatial variables $\mathbf{x}$ and $\emptyset'(\mathbf{x}, t)$ is the functions contains the modelled spatial variables $\mathbf{x}'$.

What's more, SGS stresses of LES is different with RANS Reynolds stress due to additional contributions of filtered functions and unresolved variations smaller than the cutoff width mentioned above. Thus, the SGS stress is written as follow:

$$\tau_{ij} = \rho\overline{u_i u_j} - \rho\overline{u}_i\overline{u}_j = \left(\rho\overline{\overline{u}_i\overline{u}_j} - \rho\overline{u}_i\overline{u}_j\right) + \rho\overline{\overline{u}_i u_j'} + \rho\overline{u_i'\overline{u}_j} + \rho\overline{u_i' u_j'}$$

(3-25)

where $\rho\overline{\overline{u}_i\overline{u}_j} - \rho\overline{u}_i\overline{u}_j$ is called the Leonard stresses, $\rho\overline{\overline{u}_i u_j'} + \rho\overline{u_i'\overline{u}_j}$ is called the cross-stresses, and $\rho\overline{u_i' u_j'}$ is LES Reynolds stress. The three stresses items above represent the interaction between large scales, between large and small scales, and between sub-grid scales respectively.

It should be noted that for hybrid RANS-LES methods, grey area problem is one main issue that had been proposed and identified by Spalart et al[34], which happens in specific case when attached boundary layer modelled by RANS is

followed by separation that resolved by LES. The switch of two models leads to inconsistency of turbulent kinetic energy, which forms an area neither RANS nor LES. However, DES can reduce the influence of grey area to a very insignificant one due to its amplification of resolved turbulence development that only acting on massive separation, and that is the reason why DES is more suitable for massive separation prediction than other original hybrid RANS-LES methods.

It should also be highlighted that DES is not the same as embedded LES. Although both methods require different grid design for different models, the latter has a clear distinction between RANS and LES region and needs appropriate solution method at the region interface.

4 Mesh Generation

Grid generation is the most important step of CFD simulation, as grid quality and solution results have a highly significant correlation. Besides, some key locations are particularly refined for a better solution. In this Chapter, we will discuss about the mesh generation process for every detail steps, including the creation process, quality examination and the setup work.

4.1 Grid Guideline

According to the Workshop, some gridding guidelines for self-generated grids are published for reference, which targets to guarantee the required mesh quality. Based on the given test case (Re=4.3 million based on reference chord length of 39.6 inches), initial spacing normal to all viscous walls should be restrained to reach the required y plus value for grids of different density, the guideline of which is shown in Table 4-1.

Table 4-1 Gridding Guideline for HiLiftPW-1

Mesh	y+	dy[inch]	Minimum cells across TE base	Cell Number Generated (Million)
Coarse	1.0	0.00020	4	8
Medium	2/3	0.00013	6	22
Fine	4/9	0.00009	9	30
Extra Fine	8/27	0.00006	14	-

It should be specifically noted that for medium mesh, more detailed guidelines should be referred to for chordwise spacing on each local device (slat, wing and flap) and spanwise spacing on both leading edge and trailing edge. Those

guidelines lead to a 22 million medium mesh, detailed generation steps will be focused on in the next sections. The medium grid guidelines are shown in Table 4-2.

Table 4-2 Detailed Gridding Guideline for medium grid from HiLiftPW-1

	Flap		Wing		Slat	
Chord length [inch]	LE	TE	LE	TE	LE	TE
	14.7	7	38.1	16.6	6.1	5.7
LE and TE chordwise spacing [inch]	0.015	0.007	0.038	0.017	0.006	0.006
Spanwise length [inch]	85.054		85.054		85.054	
Roots and tips spanwise spacing [inch]	0.085		0.085		0.085	

4.2 Mesh Generation

According to the workshop, geometry file of NASA Trap Wing can be downloaded from their website, flap position of which is comes from the 2002 Quality Assurance (QA) data [52]. All the measurement parameters and coordinates of the Trap Wing geometry are presented in Figure 4.1, which is in accordance with the data in the geometry file. For a start, the geometry is imported directly into Pointwise software. All the geometry scales are British units in Pointwise, which can be uniformly converted to SI units later during the setup work in ANSYS Fluent.

The mesh generation process is usually divided into several steps as listed below.

- Create surface mesh
- Check surface mesh quality, improve and repair
- generate volume mesh
- Examine volume mesh quality metrics, improve and repair

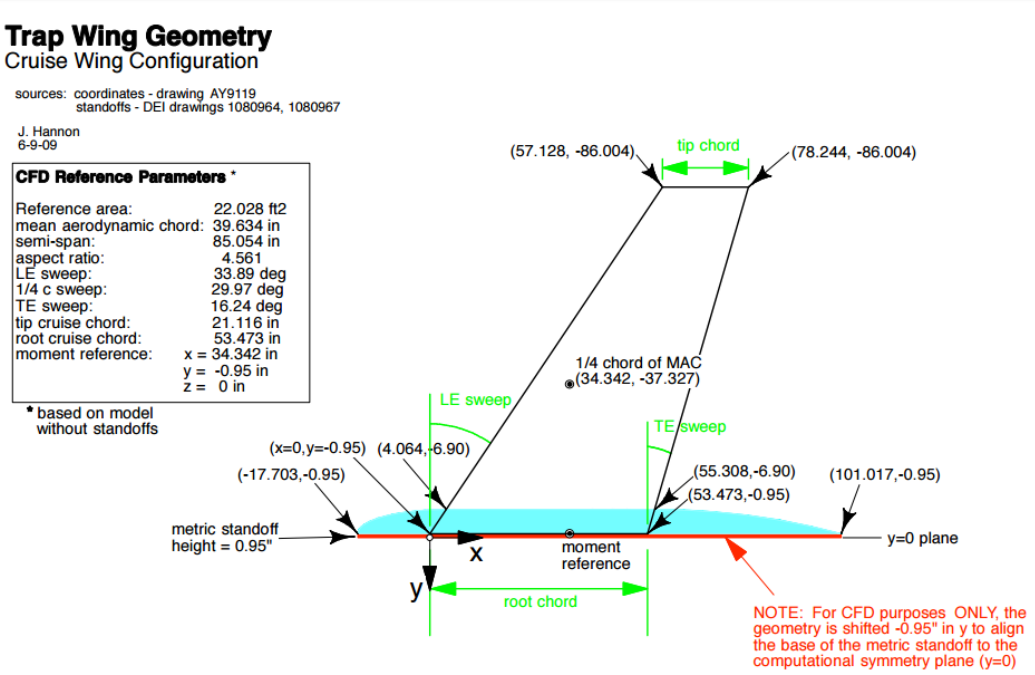

Figure 4.1 Trap Wing Geometry cruise configuration diagram [53]

In this project, the surface grid of NASA trap wing is generated in Pointwise as unstructured, three-dimensional tetrahedral elements using T-Rex algorithm. The Unstructured mesh is used because of its high efficiency during generation when dealing with complex geometry like multi-element airfoil. Also, since ANSYS Fluent is chosen for the next numerical solution, unstructured mesh seems like a wise choice under this circumstance. Because Fluent is an unstructured solver that only can handle unstructured mesh and usually deal with structured mesh by converting it into unstructured one, which involves extra work.

For surface mesh generation, grid spacing around leading edge of the main wing, the slat and the flap should also be small enough to accurately capture the flow phenomenon in that region. Moreover, the wake region around the trailing edge requires a denser grid to capture the flow separation in terms of the TE base grid guideline from the Workshop in Table 4-2. Both of the mesh refinement can be achieved by Pointwise through generating T-Rex grid with first spacing and growth rate defined and creating source to envelope region that grids need to get concentrated, respectively. For the convenience of observation, enlarged view of grid details at trailing edge base will be shown in Figure 4.2.

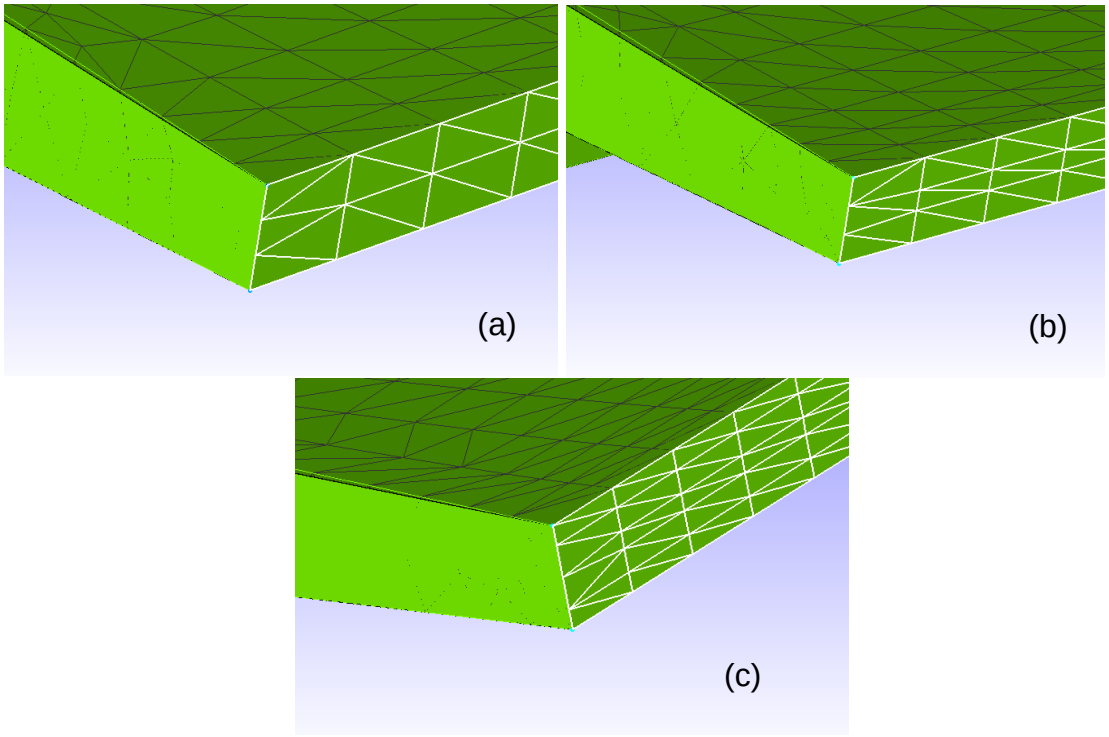

Figure 4.2 Enlarged View of Grid details at trailing edge base of coarse mesh (a), medium mesh (b) and Fine mesh (c)

To increase the computational efficiency, surface mesh density of fuselage should be decreased appropriately. Details of the medium mesh are shown in Figure 4.3 to 4.5.

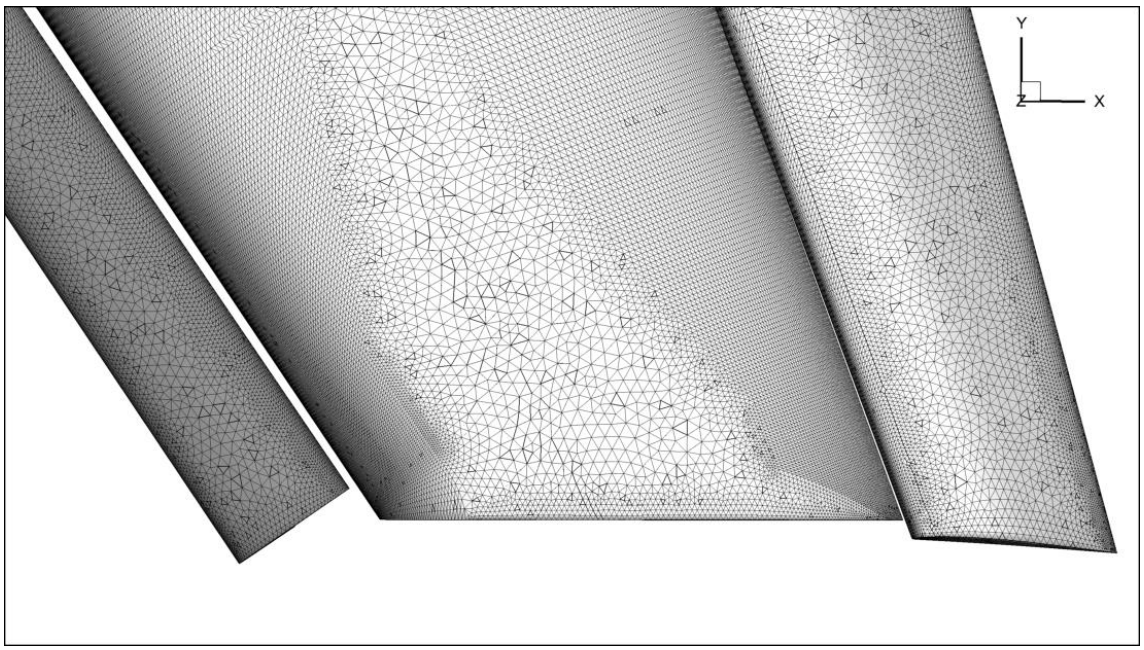

Figure 4.3 Medium mesh at wing tip (vertical view)

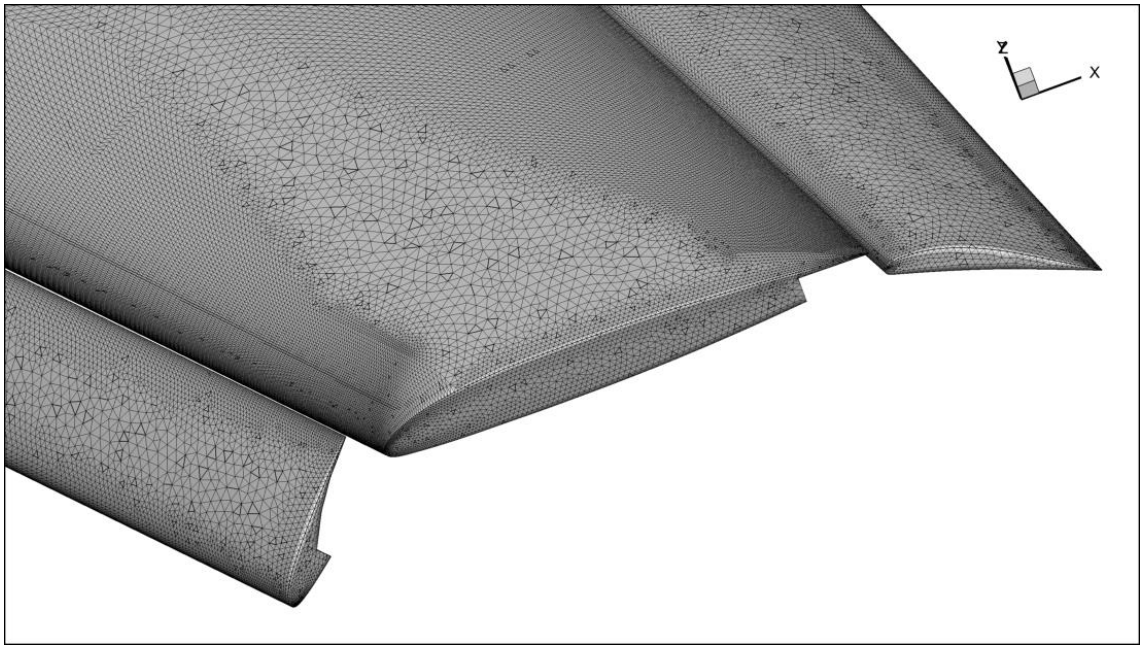

Figure 4.4 Medium mesh at wing tip (oblique view)

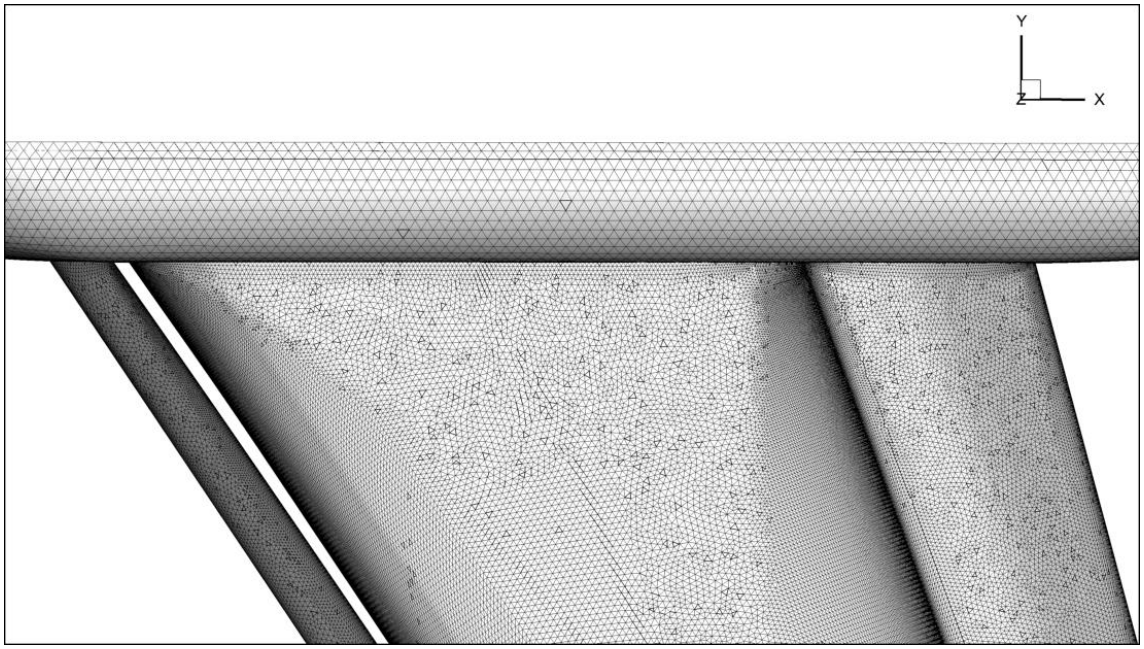

Figure 4.5 Medium mesh at wing root (vertical view)

Volume mesh is generated in the flow field, namely, the interspace between the aircraft surfaces, the hemisphere far-field surface and the circular plane spreads based on the cross section of the fuselage. The last two surfaces are created in a diameter of 20 times the length of the fuselage. The whole flow field can be regarded as a special block, which should be assembled first as the volume mesh

is generated inside the block. Next, T-Rex mesh max layer of 50 is set up with a growth rate of 1.2. The maximum y plus value and first spacing based on it from the whole surface in normal-wise direction has been provided by the Workshop. Finally, three different density of mesh has been created and each consists of four different cell types. Names and numbers of the cell type have been listed in Table 4-3.

Table 4-3 Numbers of cell for each cell type of three different density of volume mesh

	Tet	Pyramid	Prism	Hex	T-Rex	Total cells
Coarse	2699852	564758	801622	0	5146548	7457582
Medium	6033391	143910	15914174	0	16387422	22091475
Fine	12111029	283692	29880834	0	30790830	42275555

4.3 Mesh quality

After the T-Rex surface mesh created, some metrics should be evaluated to remain in limited range in consideration of the surface mesh quality, as poor mesh quality will affect the simulation results to a great extent. For every two adjacent cell of any single surface or two adjacent surfaces, a good rule of thumb is all the mesh quality metrics should be evaluated and be kept within the normal range, which leads to a good surface mesh. Here in this section, some parameters will be discussed about through Pointwise examination, including *aspect ratio, maximum included angle and equiangle skewness.*

Aspect ratio is a metric to measure the smoothness of the grid, which is defined as the ratio of the longest edge length to the shortest edge length in one cell. The optimal aspect ratio is 1. Here in this paper, for medium mesh, the average value of surface mesh aspect ratio is 3.08, with a maximum value of 21.24 and minimum value of 1.0. High aspect ratio (≥ 5) happens at the leading edge and trailing edge of slat, flap and main wing, not including the element tips and roots. This is

due to the grid guideline of minimum cells across the trailing edge base, which results in an extremely small spacing along the streamwise direction and vertical direction. Meanwhile a relative large spacing along the spanwise direction is applied in consideration of the mesh density, because too large mesh quantity cannot be handled by computational resource available.

Maximum Included Angle is a measure of cell skewness and literally means the maximum value of all the included angle of a cell. During T-Rex mesh generation, the maximum included angle has been restricted to less than 175°[54]. According to the examination results, the maximum value of the maximum included angle is 171.6, which is within limits.

Equiangle Skewness is represented as the maximum ratio of the cell's included angle to the angle of an equilateral element Q_e (60° for triangle, 90° for quadrangle)[55]. Equiangle Skewness is usually defined as

$$max\left[\frac{(Q_{max}-Q_e)}{(180-Q_e)},\frac{(Q_e-Q_{min})}{Q_e}\right]$$

where Q_{max} is the maximum included angle, Q_{min} is the minimum included angle. For this metric, high quality mesh is achieved when it gets closer to 0, conversely, low quality mesh is achieved when it gets closer to 1. In this research, the maximum value of equiangle skewness is 0.96. Empirical range from CFD practitioner indicates that value below 0.9 is acceptable. The cells of excess skewness value are distributed in the same regions as the high aspect ratio part.

Table 4-4 List of Surface Mesh Quality Metrics

Metrics	Average	Maximum	Minimum
Aspect Ratio	3.08	21.24	1.0
Equiangle Skewness	0.45	0.96	1E-12
Maximum Included Angle	81.2	60	171.6

After the surface mesh is created and examined, volume mesh will be generated. According to grid guideline in table 4-1, take medium mesh for example, wall spacing for the boundary layer is 0.0002 inches. Growth rate for two adjacent cell layers is set to 1.2 with a limitation of max layer of 50. Based on practical experience, there is a strong link between the time cost of a volume mesh generation and the surface mesh quality. A good surface mesh usually costs less time in the following volume mesh creating process.

Figure 4.6 to 4.10 illustrate the cell volume cutting contour at three different spanwise positions and the enlarged details at the gap between slap and wing as well as the gap between wing and flap. No negative cell volume error shows in the whole mesh block.

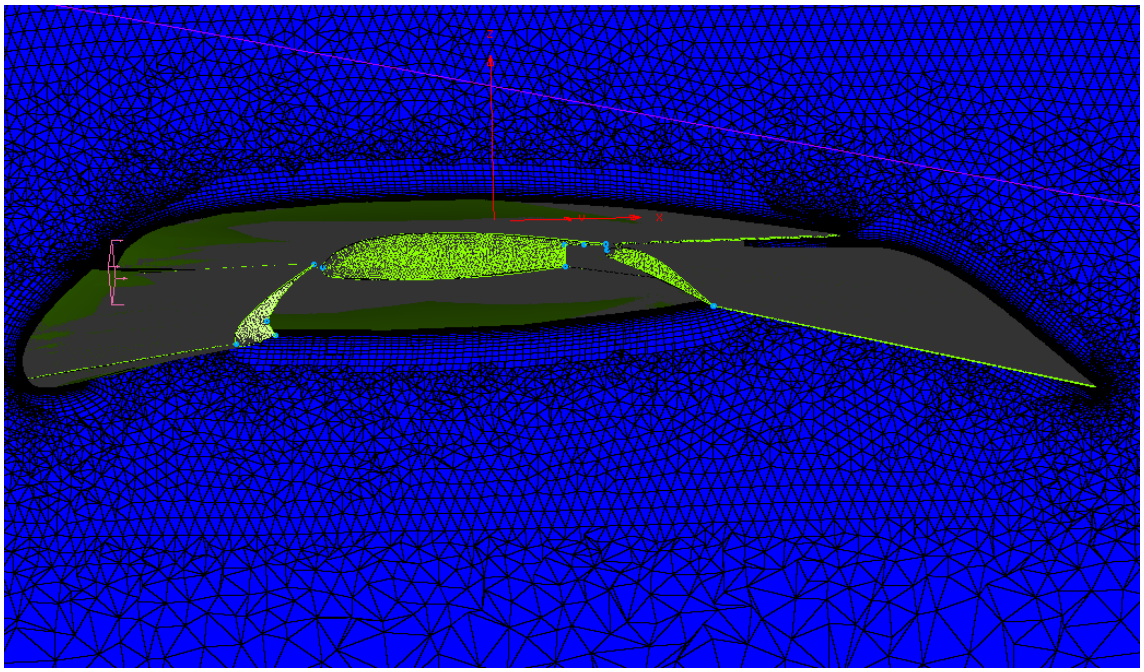

Figure 4.6 cell volume contour at y = -10 inches

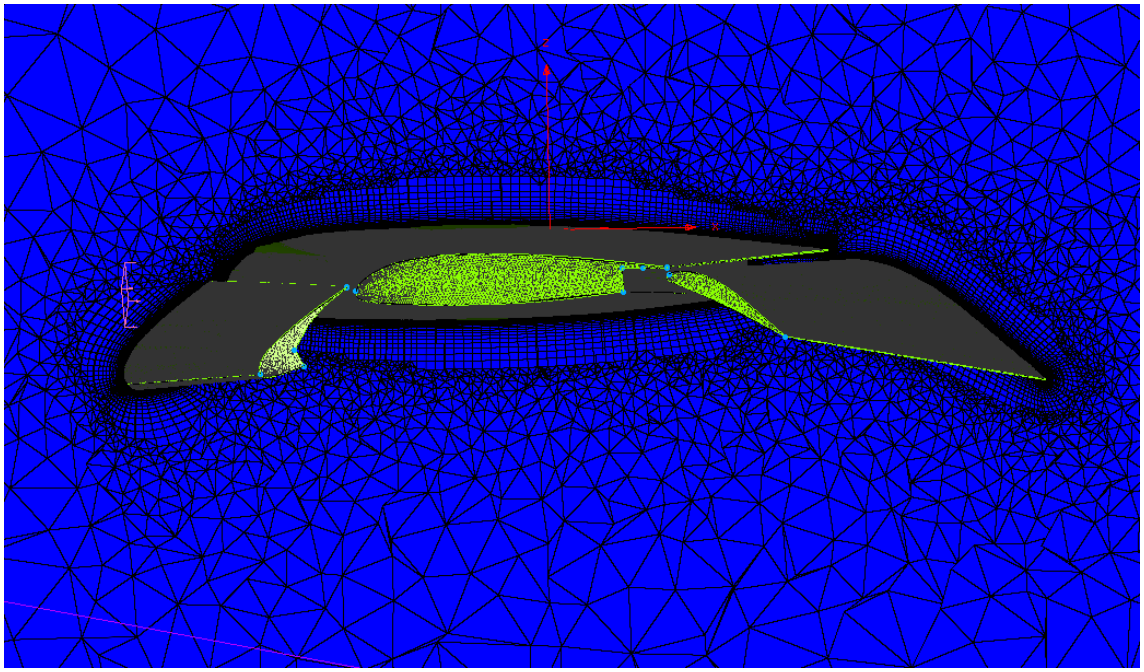

Figure 4.7 cell volume contour at y = -40 inches

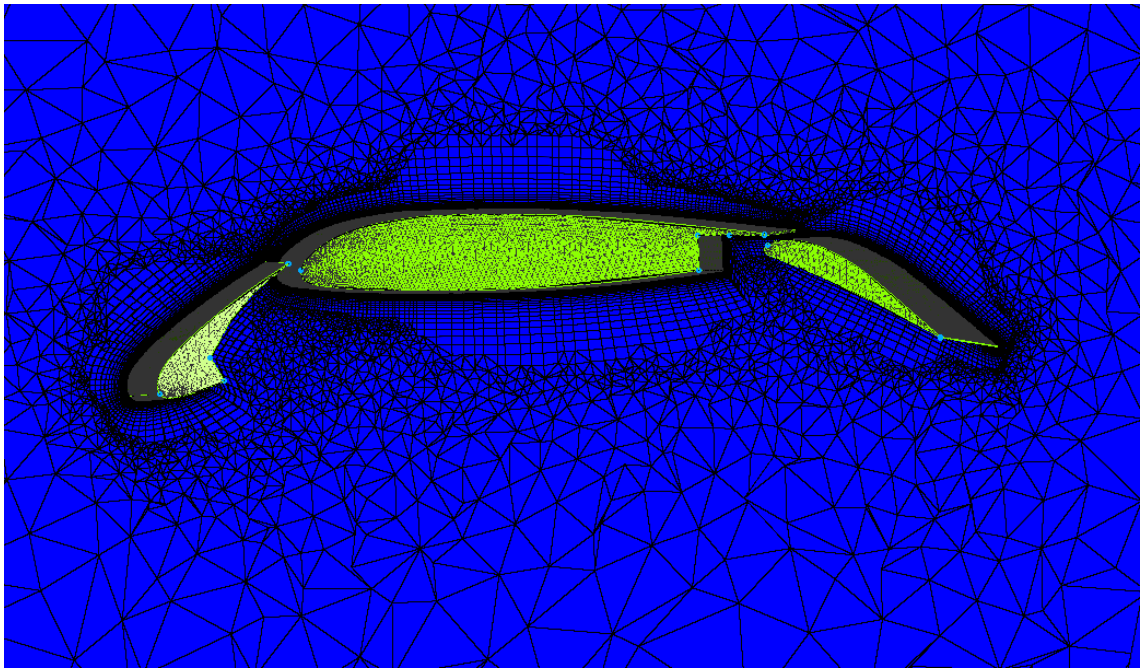

Figure 4.8 cell volume contour at y = -80 inches

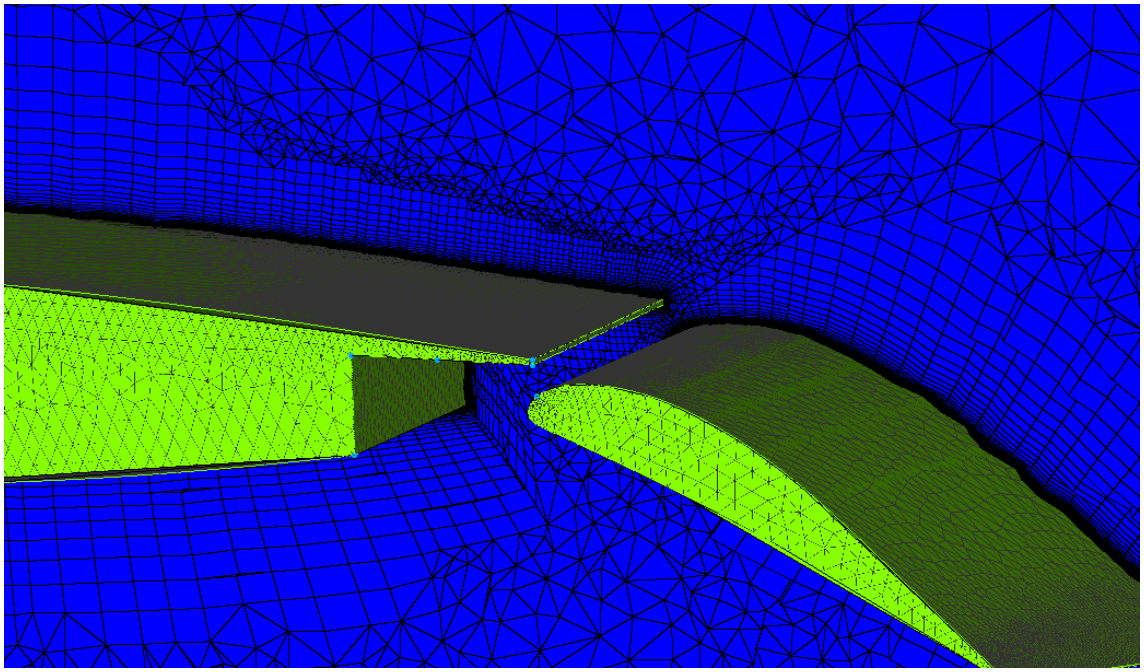

Figure 4.9 detail of cell volume contour at y = -80 inches

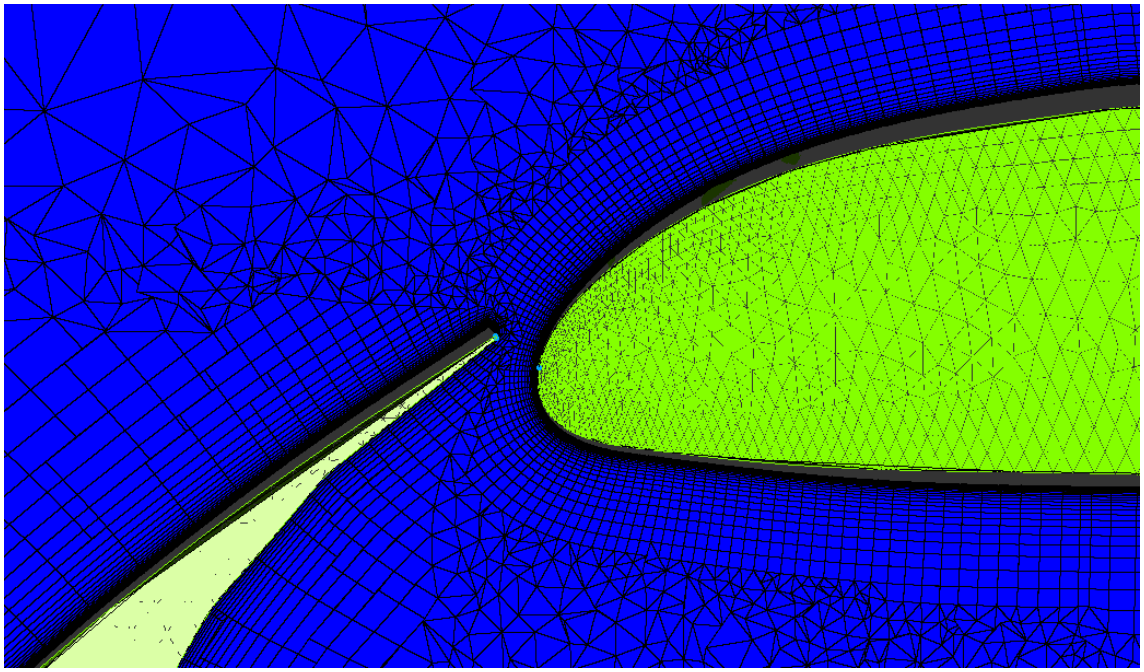

Figure 4.10 detail of cell volume contour at y = -80 inches

5 Result Analysis and Discussion

This section will mainly talk about the prediction results analysis, in terms of several flow characteristics including but not limited to pressure coefficient distribution, drag, lift and moment coefficient, skin friction. For verification, flow characteristics will be compared to experimental data provided by 1st AIAA high lift prediction workshop. Detailed flow visualization of flow separation at high angles of attack near stall will also be displayed and discussed. For further research, the r.m.s velocity of turbulence varies with time will be figured out for assessment of the performance of DES. All computational results are exported from Fluent and analysed and plotted in Microsoft Excel and Tecplot360. Additionally, Engauge digitizer software is applied for data digitization and comparison with results of other Workshop participants.

5.1 Case Setup

The case setup process is one of the most important steps for accurately calculating the solution to model, which usually consists of defining all the flight conditions and solving methods of the simulation. Two test cases will be studied in this report. The first test case is grid convergence study of landing configuration at the angle of attack of 13 degrees only in coarse, medium and fine grids. The second test case is flap deflection prediction study in six increasing angles of attack and only medium mesh with 22 million cells is used in consideration of the availability of the computing resource and temporal constraints. Flight conditions and official test cases are shown in Table 5-1 and 5-2, respectively.

Table 5-1 Flight Test Conditions

temperature [K]	density [kg/m^3]	viscosity [$Pa\cdot s$]	kinematic viscosity [m^2/s]
288.89	1.2226	1.8E-5	1.4724E-5

Table 5-2 Official Test Cases for HiLiftPW-1

Test Case	Grid Convergence	Flap Deflection Prediction Study
Mach number	0.2	0.2
Config	Slat 30, Flap 25	Slat 30, Flap 25
Reynolds number	4.3 million	4.3 million
Reference Temperature (k)	288.89	288.89
AoA to be computed (deg)	13, 28	6, 13, 21, 28, 32, 34, 37
Tested Models	S-A	S-A, k-ω SST, DES

5.1.1 RANS Model Setup

The RANS setup tasks start with solvers selection. There are two RANS models for flow prediction, including S-A and k-ω SST. For both models, a density-based solver is chosen as the fluid is incompressible based on its free-stream Mach number. As both the test cases do not involve a rotation, an absolute velocity formulation should be selected. Finally, steady time solver will be in use for computing for both models.

Next, the fluid material should be confirmed as properties of air, while the solid material of wall keeps default as aluminium. For fluid density, the ideal gas law is applied for fluid density while Sutherland law is applied for fluid viscosity, and the former law forces the energy equation to be checked. For boundary condition, the pressure far field boundary condition should be set up to the free-stream Mach number as 0.2, with 7 different angles of attack presented as their corresponding

radians value (as in Table 5-5 below), and the Gauge pressure should be set to 0 pascals. Reference Temperature should be specified to 288.89K.

All reference values should be computed from far field boundary, which is listed in Table 5-3. Parameters related to the airframe are converted to SI units. It should be noted that viscosity value is computed based on Reynolds number, free stream velocity, air density and chord length.

Table 5-3 Reference Values

Area [m^2]	2.046
Density [kg/m^3]	1.2226
Enthalpy [j/kg]	0
Length [m]	1
Pressure [pascal]	0
Temperature [K]	288.89
Velocity [m/s]	68.06
Viscosity [kg/m·s]	1.8E-5
Ratio of Specific Heats	1.4

All Solution methods choices are listed in Table 5-4. Implicit formulation is chosen for the numerical solution schemes. Though implicit solution methods requires more internal memory and computational time due to its principle of solving the unknown variables by sets of coupled equations, a matrix through iteration method[56], it shows a superior performance in computational accuracy and converging velocity when compared with explicit formulation.

Roe-FDS is chosen for convective flux type of spatial discretization, which is proposed by Roe[57] in 1986. Roe-FDS is short for Roe Flux-Difference Splitting Scheme, which can be regarded as a second-order central difference plus an added matrix dissipation. Substantially, it is a method that estimate the flux vector F by splitting it into parts with information that propagates in their own direction as well as the corresponding eigenvalues, which makes the flux vector for each face as

$$\mathrm{F} = \frac{1}{2}(F_R + F_L) - \frac{1}{2}\Gamma\left|\hat{A}\right|\delta Q$$

(5-1)

The detail of the equation will be omitted here.

It is recommended in most cases and default in Fluent for its accuracy for it providing stability and effective convergence for incompressible flows. However, it shows lack of robustness when dealing with high Mach number flow in comparison with AUSM (advection upstream splitting method) scheme. In this paper, low Mach number of 0.2 is applied, hence Roe-FDS is chosen and accurately enough in this case.

When it comes to spatial discretization, Green-Gauss node-based scheme is chosen as the gradient evaluation. It is a method that reconstructs the scalar value at a node from its surrounding cell centre value or computes the secondary diffusion terms and velocity derivatives[58], which is applied for irregular unstructured mesh. In Fluent Theory Guide, this scheme is described as to compute the gradient of the scalar at cell volume centre.

$$(\nabla\emptyset)_{c0} = \frac{1}{\nu}\sum_f \overline{\phi}_f \vec{A}_f$$

(5-2)

where the value of scalar at the cell face centroid $\overline{\emptyset}_f$ is computed by

$$\overline{\emptyset}_f = \frac{1}{N_f}\sum_{n}^{N_f}\overline{\emptyset}_f$$

(5-3)

where N_f is the face nodes number.

Though the node-based method consumes more than the cell-based method, it provides a more accurate prediction result. As for the spatial discretization of flow, turbulent kinetic energy and dissipation rate, second order upwind scheme is selected. Upwind scheme is a discretization method that use the cell value upstream to evaluate the face value, which is computed in an order of flow direction. Hard though it may get converged, second order upwind is still a better choice in complex cases because it can yields higher precision results than the first order upwind scheme.

Table 5-4 Solution method setup for S-A model

Subject		Setup
Formulation		Implicit
Convective Flux Type		Roe-FDS
Spatial Discretization	Gradient	Green-Gauss Node Based
	Flow	Second Order Upwind
	Turbulent Kinetic Energy	Second Order Upwind
	Turbulent Dissipation Rate	Second Order Upwind

Lift, drag and Moment coefficient needs to be set up first to get monitored in Fluent. For further information, C_L and C_D should be appointed in a correct direction that breaks down into sine and cosine values in x and z component,

respectively. As a matter of convenience, specific values of components are listed for velocity direction setup as well as lift and drag coefficient monitor in different pitch angle cases, which are illustrated in Table 5-5.

Table 5-5 Velocity, lift and drag coefficient component for all test cases

test case	AoA	Velocity component		C_L component		C_D component	
		U_x	U_z	x	z	x	z
1	6	0.995	0.105	-0.105	0.995	0.995	0.105
2	13	0.974	0.225	-0.225	0.974	0.974	0.225
3	21	0.934	0.358	-0.358	0.934	0.934	0.358
4	28	0.883	0.469	-0.469	0.883	0.883	0.469
5	32	0.848	0.530	-0.530	0.848	0.848	0.530
6	34	0.829	0.559	-0.559	0.829	0.829	0.559
7	37	0.799	0.602	-0.602	0.799	0.799	0.602

Moment coefficient monitor references are given by the Workshop from Trap Wing Geometry cruise configuration diagram (Figure 4.1), which are converted to SI units here in Table 5-6. Both figure 5.1 and 5.2 illustrate the Trap Wing model in wind tunnel test. As can be seen, only pitching moment over y-axis is measured in the test. Thus, the moment axis in moment monitor can be set up as a vector of (0, 1, 0), as in Table 5-6.

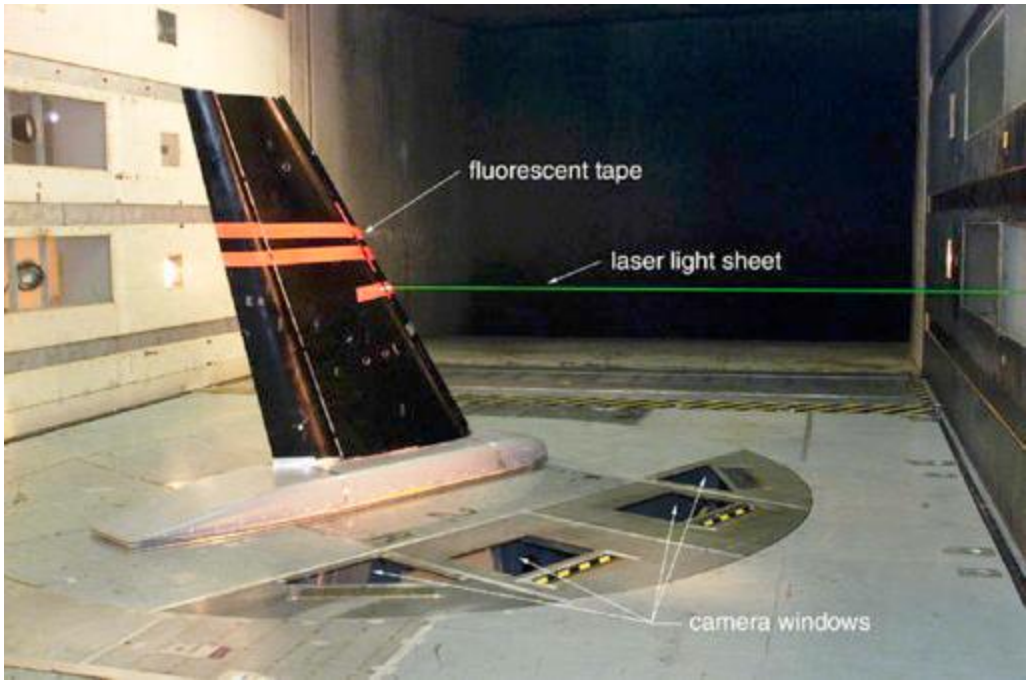

Figure 5.1 Flow field test of NASA Trap Wing [11]

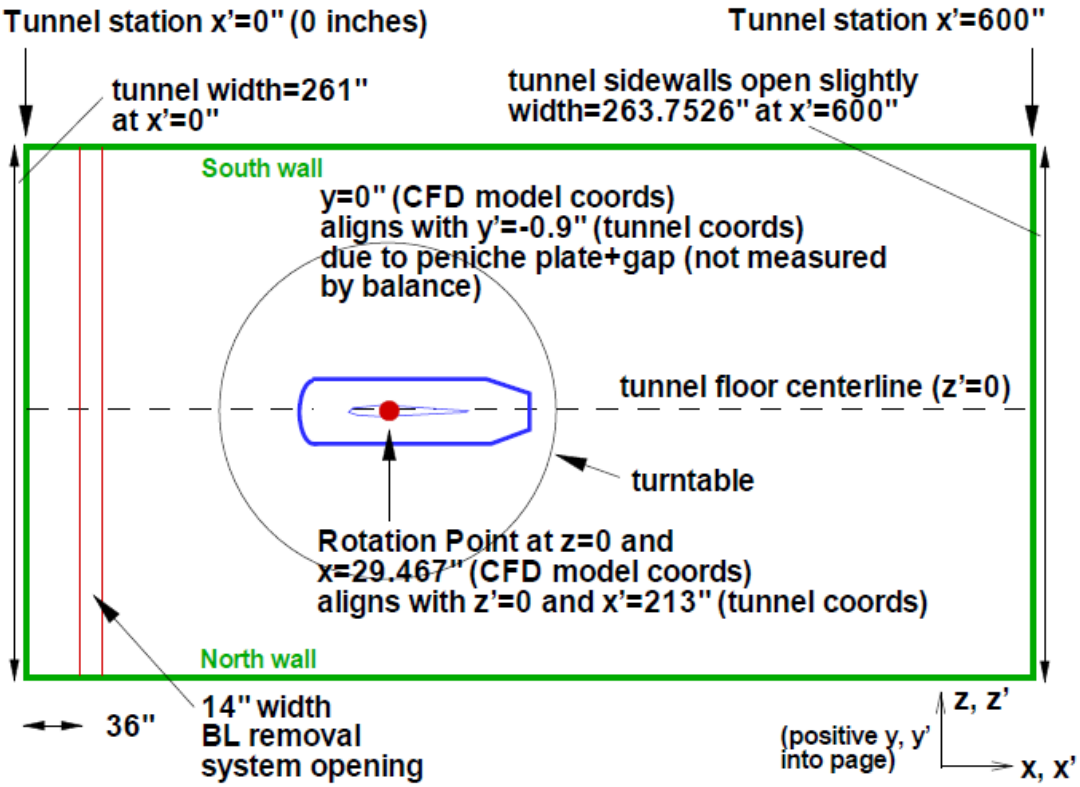

Figure 5.2 Trap Wing position in 14x22 Tunnel [59]

Table 5-6 Moment monitor setup value

Name	x	y	z
Moment Centre (m)	0.872	-0.0243	0
Moment Axis	0	1	0

5.1.2 DES model Setup

For DES model case, time solver has been switched to transient. Accordingly, modifications has been made to solution method and corresponding calculation activities. Table 5-7 listed all the solution method selections.

Table 5-7 Solution method setup for DES model

Subject		Setup
Formulation		Implicit
Convective Flux Type		Roe-FDS
Spatial Discretization	Gradient	Green-Gauss Node Based
	Flow	Second Order Upwind
	Modified Turbulent Viscosity	Second Order Upwind
Transient Formulation		First-order Implicit

Different from those of S-A model, more discretization schemes have been provided such the spatial discretization in modified turbulent viscosity and time discretization. Time discretization scheme is applied for transient solver, which is associated with the integration of every term in differential equations over a time step[60]. First-order implicit scheme, namely, dual-time stepping method is

involved in the DES method, due to its unconditional stability, which leads to high-accuracy results under the condition of given time step value.

Firstly, the Time-Stepping Method is chosen as fixed with time step size, which is based on the CFL number:

$$CFL = \mathrm{U}\frac{\Delta t}{\Delta x} \tag{5-4}$$

The CFL number is related to the smallest grid size, the smallest time step and the freestream velocity in the streamwise direction. Usually, for a DES model, CFL number should be less than 1 to guarantee the accuracy of the calculation. Here in this paper, we can set the CFD number as 1, and the freestream velocity equals to 68.08m/s according to reference values in Table 3-8. To capture the flow detail at leading edge, the smallest grid size should be derived from the grid spacing at leading edge of the main wing in streamwise direction, which is 0.025inch. When all the units are converted to SI units and substituted into Equation 5-4, the minimum time step will reach the results of $1e^{-05}$s.

The number of time steps is set up to 5000 for a start, which will lead to a physical flow time of 0.05s. Then the time steps will be added until the solution gets converged, and the start number is in consideration of the bearing capacity of Delta. There are at most 30 iterations in each time step, the solution will directly switch to next time step if it comes to convergence before the max number of iterations in each time step. All the calculation setup of DES is listed as follows in Table 5-8.

Table 5-8 Transient Calculation Setup

Time Stepping Method	Fixed
Time Step Size (s)	1e-05
Number of Time Steps	5000
Sampling Interval	100
Max Iterations/Time step	30

5.1.3 Grid Convergence Study

Grid convergence study always plays an important role in CFD numerical simulation for its value in verifying the refinement level of grid and selecting the optimal grid choice for an accurate prediction results. Grid convergence study are usually carried out to test the grid independence, namely, when the refinement of the grid reaches a certain extent, the solution will not be improved any further. Generally, two methods are widely used in the verification study, which will be applied in this paper (see below).

The first method is the convergence study of aerodynamic coefficients, as is shown in Figure 5.3. This figure consists of three plots of convergence criteria: lift, drag and moment coefficient respectively against cell number to the power of -2/3. Results are computed from three different density level of mesh at angle of attack of 13 degrees only with S-A model and results are compared with data from wind tunnel test. From pictures above, it can be seen that simulation results of the coarse mesh are obviously different with experiment results, especially for lift coefficient, which shows an error of 13.8%. As the mesh refined with smaller grid spacing and more cell number, the solution is closer to experiment results, hence the solutions are well within the asymptotic range of convergence.

However, there is no significant change between the medium and fine mesh, therefore the medium mesh is chosen for computational resources saving.

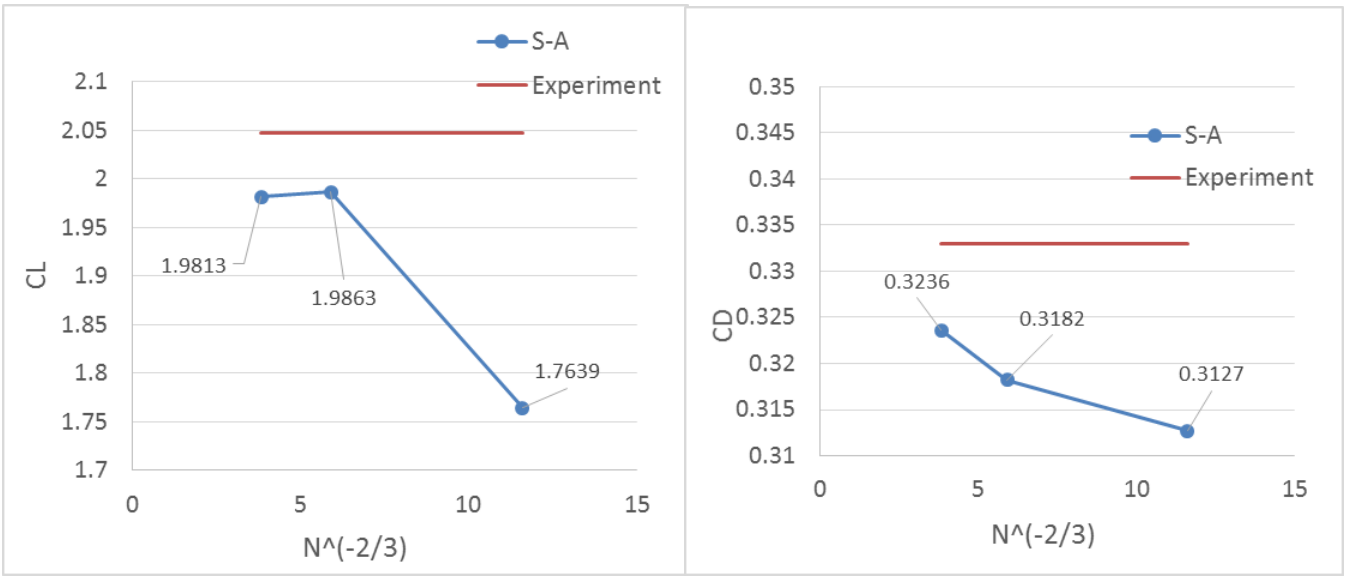

(a) Lift Coefficient (b) Drag Coefficient

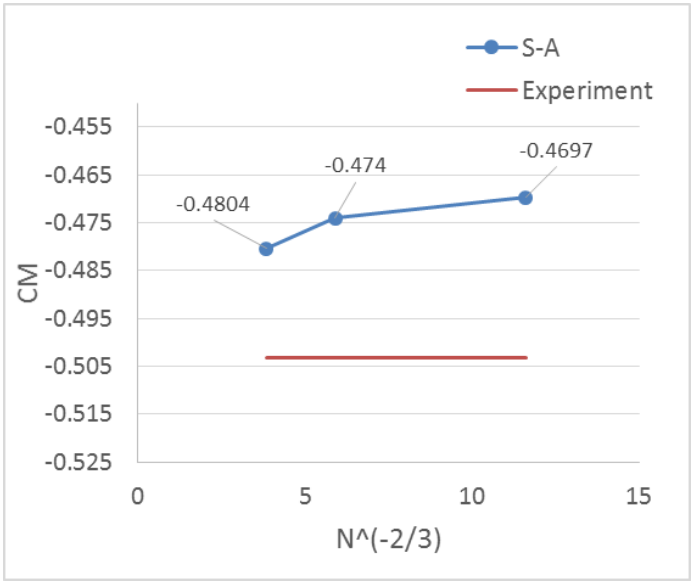

(c) Moment Coefficient

Figure 5.3 Grid Convergence test for lift, drag and moment coefficient

The other method is called Grid Convergence Index (GCI), which is proposed by P. J. Roache in 1994[61]. Essentially, it is a grid refinement error estimator originated from Richardson Extrapolation.

$$f = f_{exact} + g_1 h + g_2 h^2 + g_3 h^3 + \cdots$$

(5-5)

where f is the numerical solution with the grid spacing h, and f_{exact} is the exact solution to the formulation.

For three-dimension calculations, the grid spacing h equals to[62]

$$h = \left[\frac{1}{N}\sum_{i=1}^{N} \Delta V_i\right]^{1/3}$$

(5-6)

where ΔV_i is the volume of the i_{th} cell, and N is the total cell numbers.

Consider grids of two different level, and solution based upon the two grids is f_1 and f_2. Then for second-order calculation

$$f_{exact} = \frac{(h_2^2 f_1 - h_1^2 f_2)}{(h_2^2 - h_1^2)} + O(h^3)$$

(5-7)

Here, a parameter called grid refinement ratio r is defined as

$$\mathrm{r} = h_2/h_1$$

(5-8)

Also, $O(h^3)$ can be dropped, which leads to

$$f_{exact} \cong f_1 + (f_1 - f_2)/(r^2 - 1)$$

(5-9)

Similarly, for calculation of any order method,

$$f_{exact} \cong f_1 + (f_1 - f_2)/(r^p - 1)$$

(5-10)

where p is the order of the method.

In Roache's another article, the grid error estimator E has been defined as the solution error of fine grid compared with a coarser one, or vice versa. For fine to coarse comparison, the error estimator is defined as[63]

$$E_{12} = \frac{\varepsilon}{1 - r^p} \tag{5-11}$$

where

$$\varepsilon = f_2 - f_1 \tag{5-12}$$

For coarse to fine comparison, the error estimator is defined as

$$E_{21} = \frac{\varepsilon}{1 - r^p} \tag{5-13}$$

Finally, the grid convergence index (GCI) can be computed as

$$GCI_{12} = F_s|E_{12}| \tag{5-14}$$

$$GCI_{21} = F_s|E_{21}| \tag{5-15}$$

Or

$$GCI_{coarse} = r^p \times GCI_{fine} \tag{5-16}$$

where F_s is a safety factor, and a value of 3 is recommended by Roache for a conservative reason.

In this paper, we can calculate the GCI for solution result of lift, drag and moment coefficient, respectively. Table 5-9 listed all the variable value during the calculation process of GCI, where subscript 1, 2, 3 respectively stand for fine grid, medium grid and coarse grid.

Table 5-9 Parameters for Grid Convergence Index Calculation

	C_L	C_D	C_M
N_1	42275555	42275555	42275555
N_2	22091475	22091475	22091475
N_3	7457582	7457582	7457582
$r_{21}(h_2/h_1)$	1.242	1.242	1.242
$r_{32}(h_3/h_2)$	1.436	1.436	1.436
f_1	1.981	0.313	-0.480
f_2	1.986	0.318	-0.474
f_3	1.764	0.324	-0.470
p	2	2	2
ε_{12}	0.005	0.006	0.006
ε_{23}	-0.222	0.005	0.004
E_{12}	-0.009	-0.010	-0.012
E_{23}	0.209	-0.005	-0.004
GCI_{21}	0.028	0.030	0.035
GCI_{32}	0.628	0.015	0.012
GCI_{12}	0.043	0.047	0.055
GCI_{23}	1.295	0.031	0.025

Test cases for all angles of attack have reached converged solutions, which can be seen in Figure 5.4, 5.5 and 5.6, all demonstrate diagram of lift coefficient CL against iteration times for S-A, k-ω SST and DES model. Each case has been

stopped running once it reached a converged solution, which explains the differences of number of iteration times for different case. For two RANS models, the lift coefficient value is calculated every iteration. For DES model, the lift coefficient value is calculated and reported for every time step. However, as the C_L value for every iteration in one step are not be monitored, whether the value is taken from averaged value for every iteration or simply taken from the last iteration in one time step is still unknown.

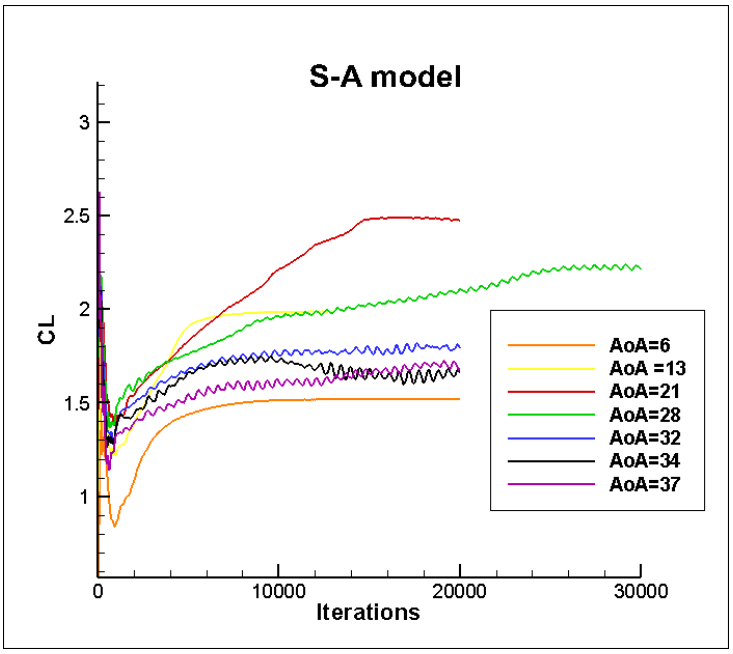

Figure 5.4 Lift coefficient vs iteration times for S-A model

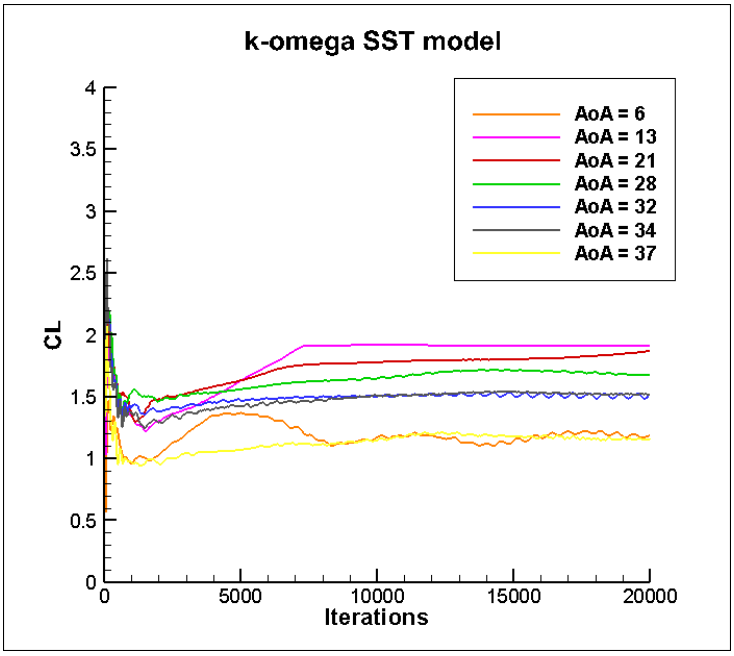

Figure 5.5 Lift coefficient vs iteration times for k-ω SST model

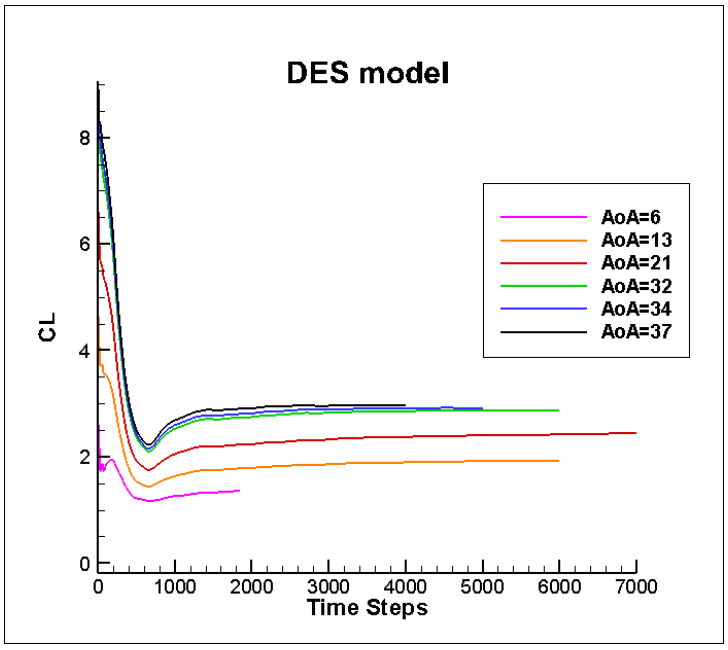

Figure 5.6 Lift coefficient vs iteration times for DES model

Moreover, for S-A and k-ω SST model calculation, as can be seen in figure 5.4, all the results get converged at about 20000 iterations, except for S-A model case AoA = 28°, which reaches a convergence at about 30000 iterations. As for DES calculation, each case gets the converged solution at different time steps, ranging from 1800 to 7000. As mentioned earlier in table 5-8, each time step contains 30

iterations, which means that the iteration time for DES model cases range from 54000 to 210000.

In pursuit of computational speed, a high performance computer of Cranfield University called Delta is applied for numerical simulations in this paper. Delta is a large Linux cluster, which requires Delta submission files written by PBS scripts language. For example, for all the turbulence models in this paper, the CPU request command line is written as

```
#PBS -l select=4:ncpus=16:mpiprocs=16
```

which means four chucks of 16 CPUs are required, namely, 64 CPUs in total. With this configuration, RANS model usually takes about two days to run 20000 iterations and get converged, while DES model usually takes one to two weeks.

5.2 Boundary Conditions

Boundary conditions are set up when volume mesh is done creating, the appointment of boundary conditions are illustrated in Figure 5.7 and 5.8.

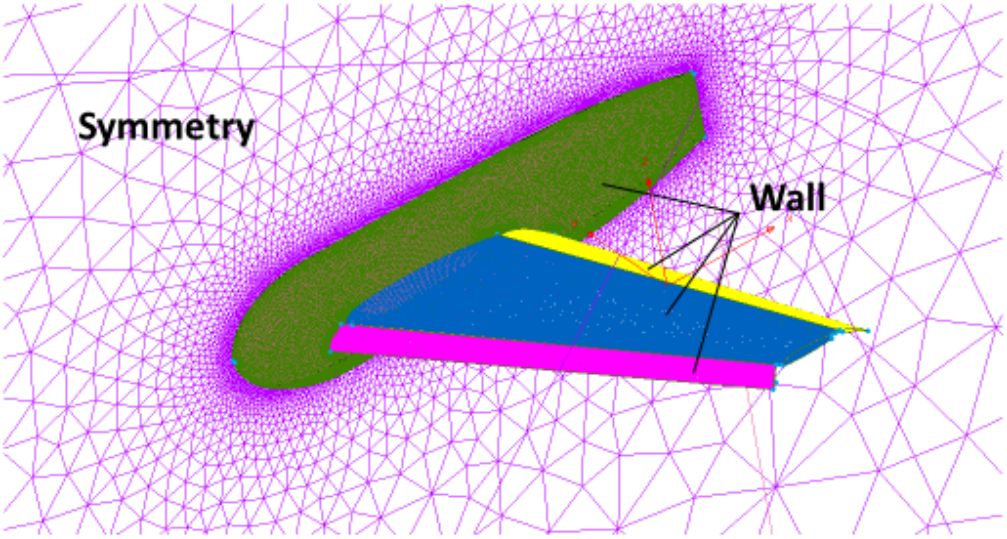

Figure 5.7 Boundary conditions

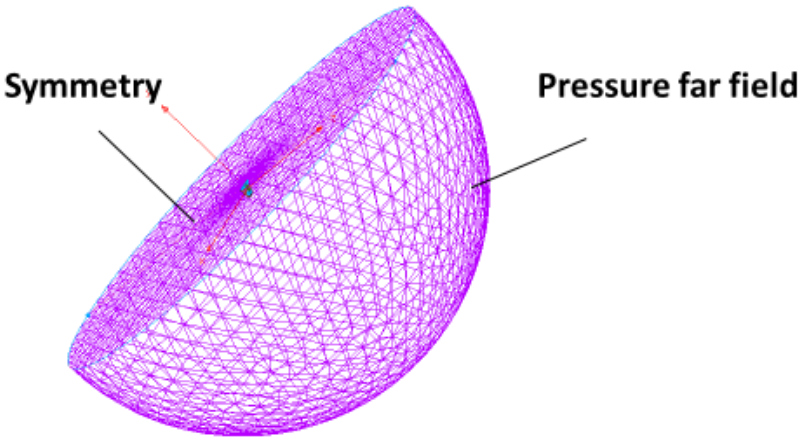

Figure 5.8 Boundary conditions

As can be seen in the figures below, all the wing, flap, slat and fuselage surfaces are specified as wall boundary condition. It is used to bound solid and fluid regions. In our case, no heat transfer is conducted between the fluid and solid region, thus, for all the wall zone and pressure far-field zone, the temperatures are identical and all set to 288.89K.

The spherical surface, namely, the outer boundary of the flow field is specified as pressure far field, which is used to determine the free-stream flow variables at the boundary. This boundary condition can only be applied when flow density is calculated with ideal-gas law. Momentum boundary conditions for pressure far field such as the Mach number and flow direction (angle of attack) are set up as in figure 5.9. Gauge pressure is the difference between the real pressure and the atmospheric pressure. As the real pressure equals to the atmospheric pressure here in Fluent, Gauge pressure is usually kept as default setting of 0 pascal.

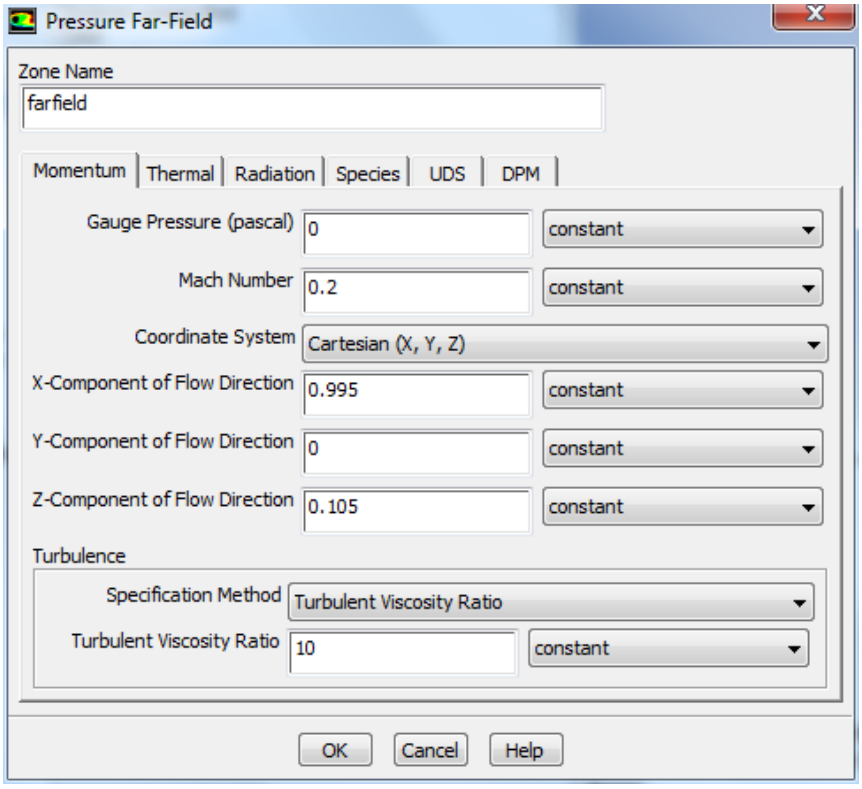

Figure 5.9 Boundary Conditions of Pressure Far-Field for S-A and DES model

Another boundary conditions for pressure far-field boundary are turbulence parameters. A specification method should be chosen first for different turbulence models. In this paper, turbulent viscosity ratio is chosen for S-A and DES model, intensity and viscosity ratio is chosen for $k-\omega$ SST model. All the parameters remains constant and are set to the default value. The turbulent viscosity ratio has a default value of 10 and turbulent intensity has a default value of 5%.

The plane part of the hemisphere is set up as symmetry. As its name suggests, symmetry boundary layer is usually set at the symmetry plane of an expected mirror-symmetric 3D geometry. It is noteworthy that there are no boundary conditions at symmetry boundaries.

Finally, the block contains the whole flow field needs to be given a volume condition as a type of fluid, where all the flow calculations are applied. The volume mesh can be exported as a Fluent case file after all the boundary conditions set up.

5.3 Lift, Drag and Moment Coefficient

Lift, drag and moment coefficient are set up in Fluent monitor before being uploaded to Delta for computation, as introduced in the previous section. Forces and moments results are collected and plotted through Excel after solutions get converged.

Figure 5.10 illustrates comparing results of lift coefficient C_L against seven increasing angles of attack for three different models, S-A, k-ω SST and DES. Experimental results published by Workshop are also put in for reference. It can be obviously observed that DES has the best performance in lift prediction, except for the AoA = 37° case, where the lift does not follow the experimental data to perform a sharp decline due to stall but continue maintaining an upward trend instead. As for two RANS models, S-A model shows great consistency with the experiment before AoA = 21°, but premature stall happens after that point. For k-ω model, we can only say that the lift coefficient curve has an approximate trend of lift curve. However, with C_{Lmax} value happening at 13°, k-ω model predicts the onset of the stall at a lowest angle of attack among all the models. Also, the C_L values not only significantly deviate from the experimental data, but also shows the earliest trend of descent, which results in a lowest accuracy of prediction among the three numerical methods.

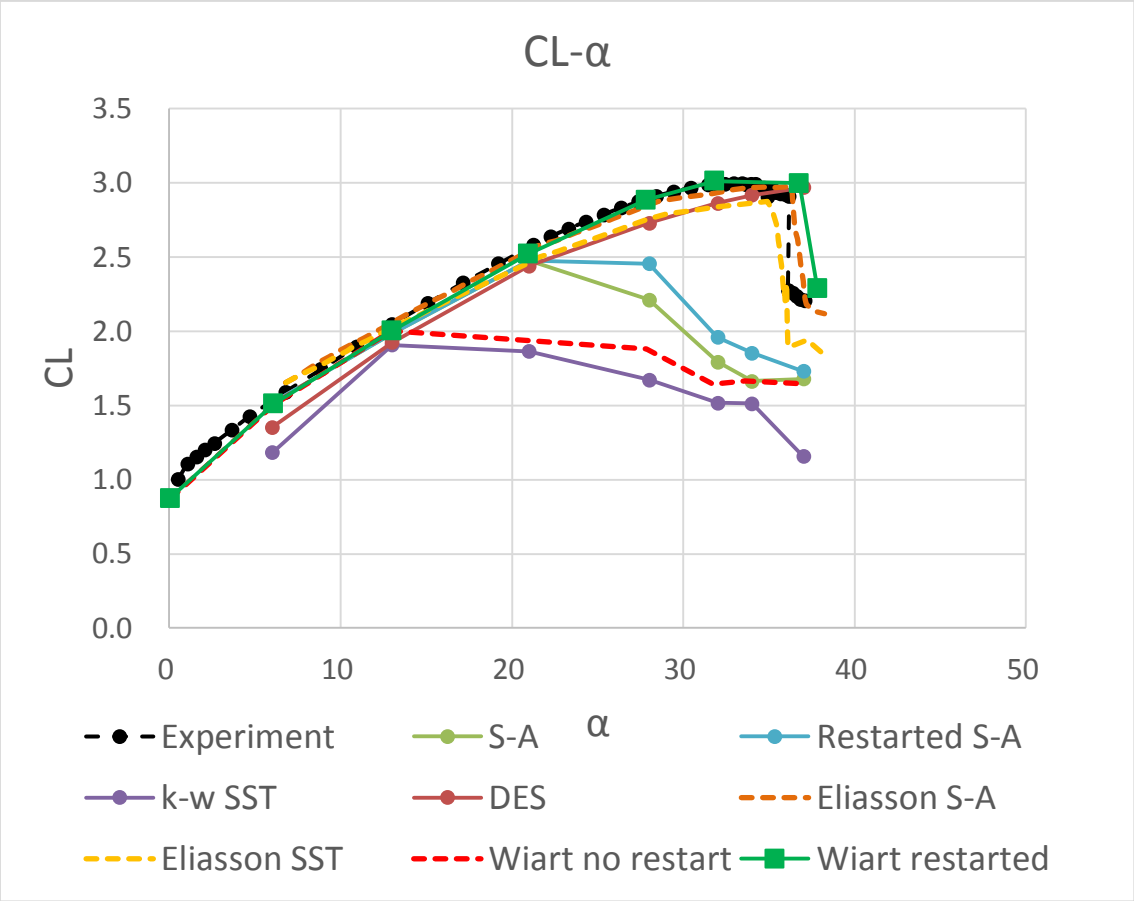

Figure 5.10 Comparison of lift coefficient vs seven various angles of attack for S-A, k-w SST, DES and experimental results

Besides, results from other participates of HiLiftPW-1 are digitized from their published presentations and papers by Engauge Digitizer software, which is a software used to digitize the data graph for replotting when no raw data can be obtained. Here in Figure 5.10, two sets of lift data are digitized and compared with author's results, respectively from Eliasson's published paper[16] and Wiart's published presentation[64]. It can be obviously observed that both turbulence model Eliasson used shows perfectly agreement with measure lift data, with SST model performs a little bit early breakdown.

It is also worth mentioning that according to some participants of the Workshop, a premature stall appears as shown above due to massive separation happens in Figure 4.1. However, experience to avoid or delay that by taking converged solutions at lower angles of attacks as initial conditions of high angles of attack.

From Wiart's data in Figure 5.10, S-A model is applied at first. However, data without initialization from previous AoA shows a similar performance of nearly the same C_{Lmax} value with k-ω SST model in this paper. After restarted, S-A model demonstrates a way better improvement.

In this project, the same method has been applied in Fluent by "Interpolate" function. For example, when AoA = 21° case is converged, the flow data can be extracted by "file - Interpolate Data – Write Data", select data in cell zones and all flow fields, then write the data into the hard drive. When it comes to AoA = 28° case setup, specify all the flight condition in the former way but leave the solution initialization alone. Import the interpolate file into the new case, then fluent will initialize the flow field using data from interpolate file. Computational results were named as "restarted S-A" and marked as blue solid points in Figure 5.10 to 5.14. The new "restarted S-A" method only starts from AoA = 28° as the lower degree cases results agree well with experiment. Unlike Wiart's results, the restarted S-A model shows an observable improvement in lift prediction. It delays the separation to some extent, but the performance is still not as good as DES. Nevertheless, DES fails to predict the stall performance with only an increasing rise of lift up to 37°. Hence, for further research, DES model should be applied in higher angle of attack case to explore its stall prediction capacity.

Meanwhile, a lack of agreement at low pitch angles happens for k-ω SST and DES model, possible reasons could be deduced that high lift system is out of optimum conditions, or the solution is lack of convergence due to closed re-circulation bubbles in flap and slat cove regions. What's more, primary cause may be the low mesh quality due to high skewness at trailing edge and leading edge of the elements.

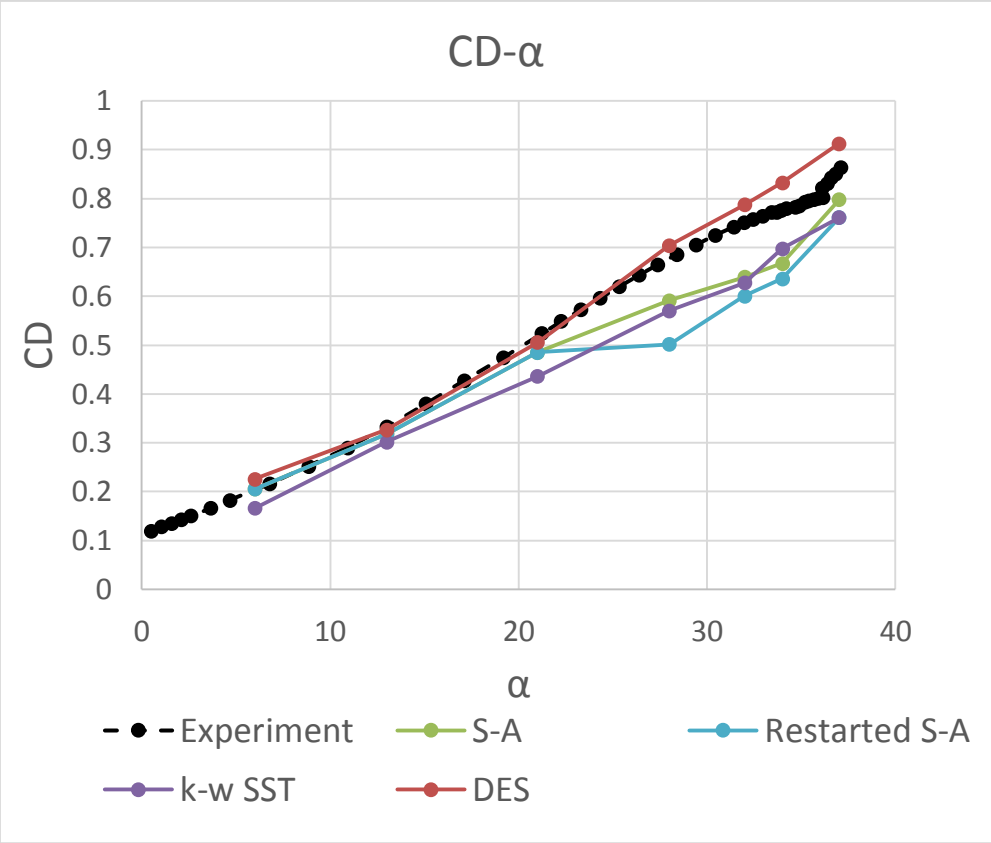

Figure 5.11 Comparison of drag coefficient vs seven various angles of attack for S-A, k-w SST, DES and experimental results

Figure 5.11 shows the comparing results of drag coefficient C_D against seven increasing angles of attack for three different models mentioned above and restarted S-A model. Like lift curve, drag curve of all models shows a same overall trend of upward and with DES showing the greatest consistency with experimental results. S-A model merely in agreement with the experiment before AoA = 21°, and k-ω model starts to deviate from the experiment from the beginning and the gap is gradually widened as the angle of attack increases. As for new S-A model, after the flowfield restarting from converged solution, unlike lift coefficient being improved, drag coefficient seems to obtain a worse result.

From Anderson's textbook[7], the calculation of drag in CFD is obtained by numerically integrating the pressure and shear stress distribution over the surface, which means the drag results that monitored and obtained from Fluent software is total drag that contains both skin friction drag and pressure drag. The former is

generated due to the shear stress acting on the aircraft surface and the latter is generated due to flow separation. Thus, the total drag in this paper can be expressed as

$$D_{total} = D_f + D_p$$

(5-17)

and the drag coefficient is calculated by

$$C_{Dtotal} = \frac{D_{total}}{q_\infty S} = \frac{D_f + D_p}{q_\infty S} = C_{Df} + C_{Dp}$$

(5-18)

As skin friction drag D_f is an integration of wall shear stress on the surface of the body, the skin friction drag coefficient C_{Df} can be expressed as

$$C_{Df} = \frac{D_f}{q_\infty S} = \frac{\int_{surface} \tau \, dS}{q_\infty S}$$

(5-19)

where $\frac{\int_{surface} \tau \, dS}{S}$ is the area-averaged value of D_f, which can be calculated through the performing integrations function in Tecplot 360. Thus, the skin friction drag component and pressure drag component can be calculated and displayed in figure 5.12 and 5.13, respectively. As can be seen in the following two plots, skin friction drag and pressure drag have totally different development trend against pitch angle with most of the drag contributed by pressure drag, which increases with the rise of angle of attack as the flow separation aggravates.

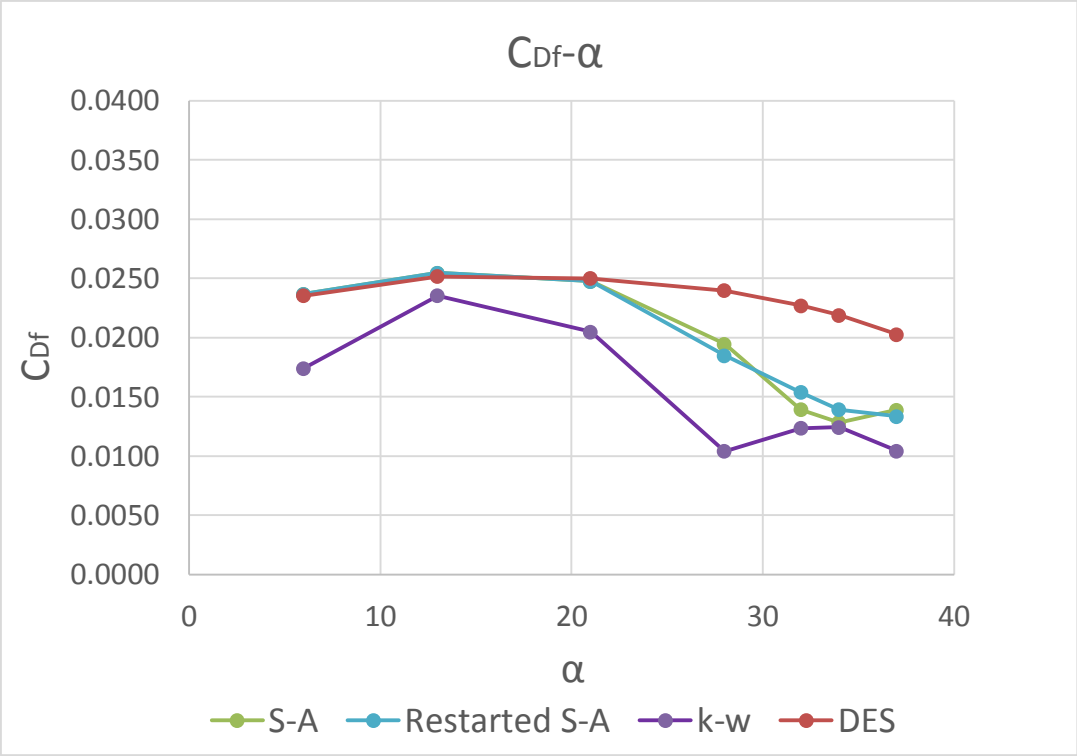

Figure 5.12 Comparison of skin friction drag coefficient vs seven various angles of attack for S-A, k-w SST and DES model

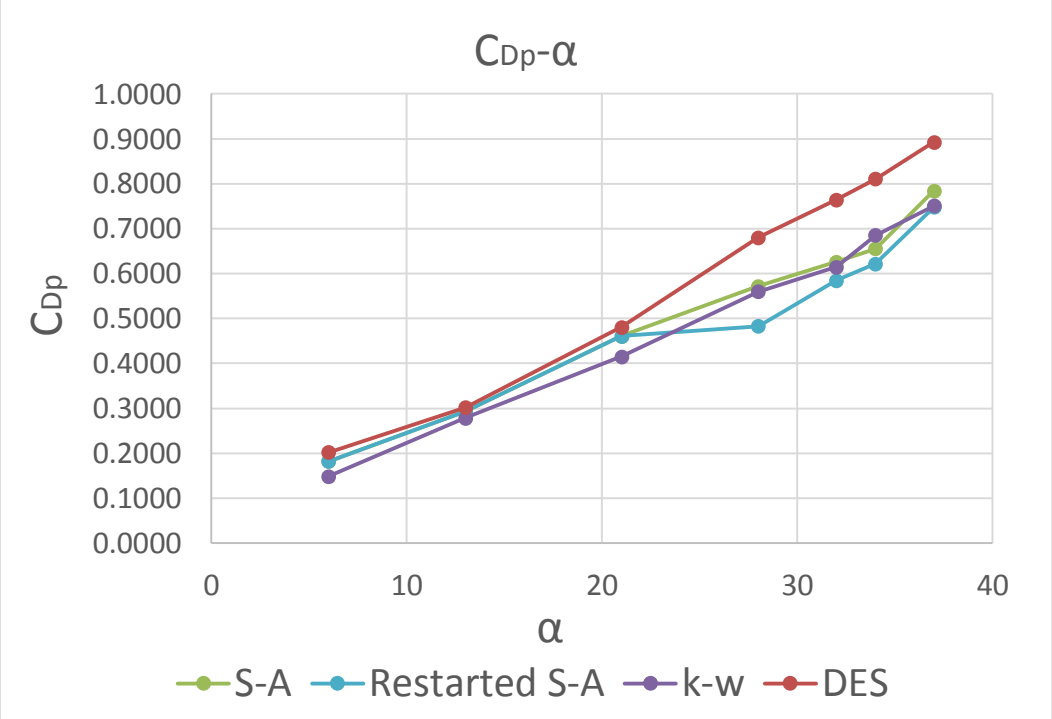

Figure 5.13 Comparison of pressure drag coefficient vs seven various angles of attack for S-A, k-w SST and DES model

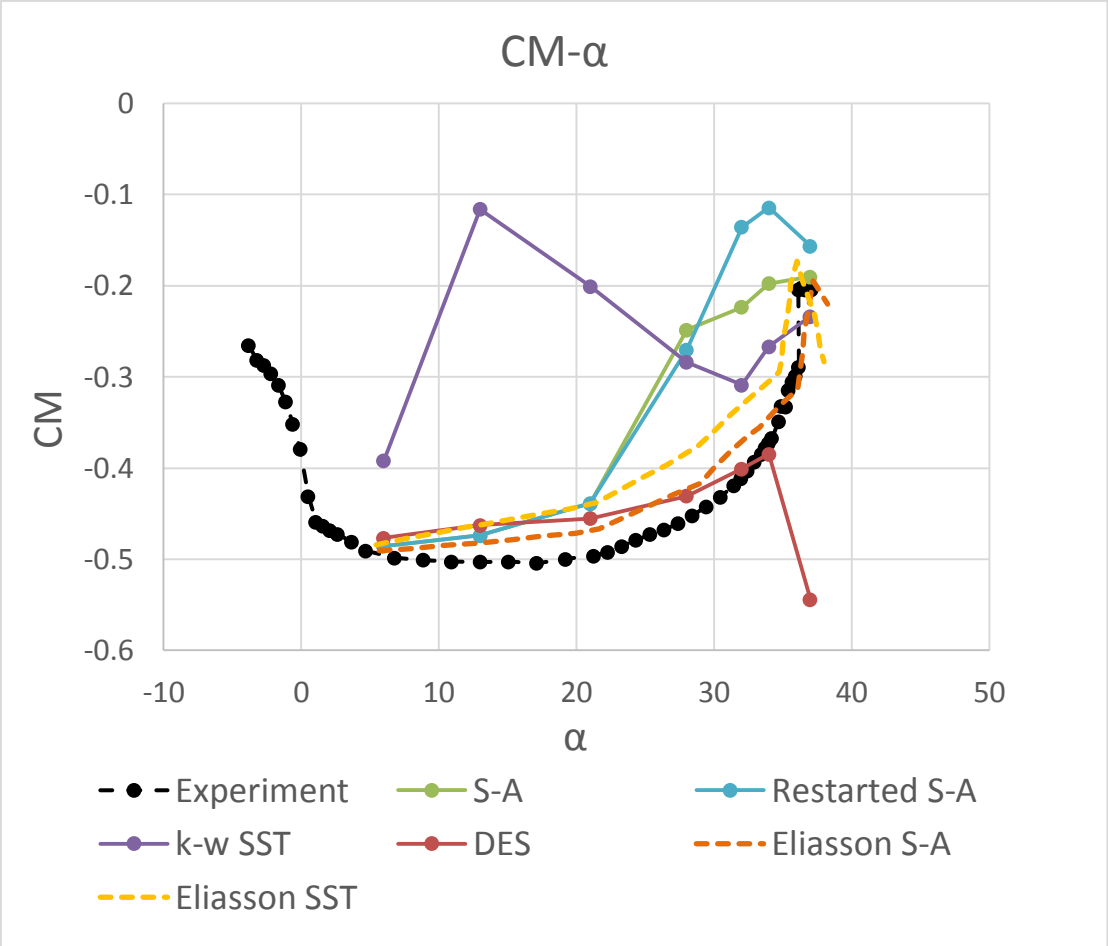

Figure 5.14 Comparison of moment coefficient vs seven various angles of attack for S-A, k-w SST, DES and experimental results

Moment coefficient plot is illustrated in Figure 5.14, where some interesting phenomenon occurs. Obviously, none of the methods perfectly meet the experiment data of moment coefficient against angles of attack. Before AoA = 21°, both DES and S-A have a similar trend of slight rising, while k-ω shows a strange behaviour of sudden rising and falling. When AoA is higher than 21°, both S-A and its restarted method start to deviate with a very high slope, and the latter has more deviation at high angles of attack. Meanwhile, k-ω continues falling until AoA = 32°, then shows slight recovery near stall. As for DES, moment coefficient seems to get on tracks as the angle of attack increases but still fails to predict post stall as in lift curve. Moment data from Eliasson's prediction

5.4 Pressure Distribution

Pressure coefficient distribution over an airfoil can reveal many flow physics, such as separation location, stall characteristics, and other flow details. Relative experimental data are provided by HiLiftPW-1 website, which are collected from Langley 14*22 wind tunnel test as mentioned in Chapter 2.In this project, pressure distribution is displayed at three different streamwise cross-sections including 17% (ST17), 50% (ST50) and 85% (ST85) of the span length counted from the wing root (as shown in Figure 5.15), for seven angles of attack ranging from 6° to 37°. Those three positions are chosen considering the purpose of figuring outflow characteristics over the airfoil as comprehensive as possible. Computational results are analysed and plotted in Tecplot360. It should be noted that the sweep angle of the wing is not taken into consideration when exporting the C_p value over cross-sections.

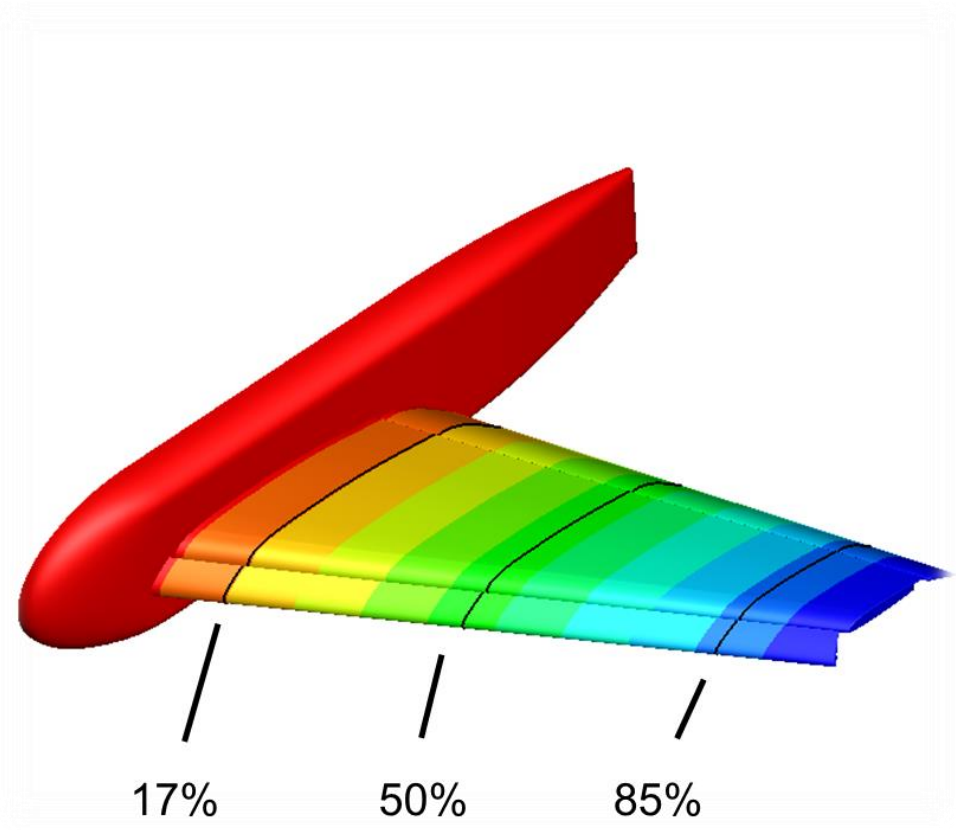

Figure 5.15 Pressure distribution location

As shown below, Figure 5.16 to 5.22 illustrate the pressure distribution comparison results for experiment and three simulation methods along the airfoil surface at seven different angles of attack at three different positions sliced through wing surface zone and parallel to y-plane, namely, position ST17, ST50 and ST85 of the span length from wing root. It can be observed that at ST17, both restarted S-A and DES can accurately predict the negative Cp peak values at leading edge of the main wing part. DES performs even better near stall but overpredicts the upper surface pressure at AoA = 37° while restarted S-A slightly underpredicts the suction side at the same angle of attack. The original S-A model starts to show incapability when AoA = 32° for the upper surface of all three elements, especially for the flap, where both the upper and lower surface pressure curve deviate from the experimental data significantly. Moreover, as mentioned in section 5.3, k-ω model gives the worst performance of lift prediction. The lift loss of k-ω can be analysed from the pressure distribution due to the C_p value at the suction side far below the experimental data.

Besides, restarted S-A model has acted with some small wiggles on lower surface near main wing trailing edge. That kind of unsteadiness may be caused by the interpolation operation, which also results in an oscillation when iteration process is being plotted.

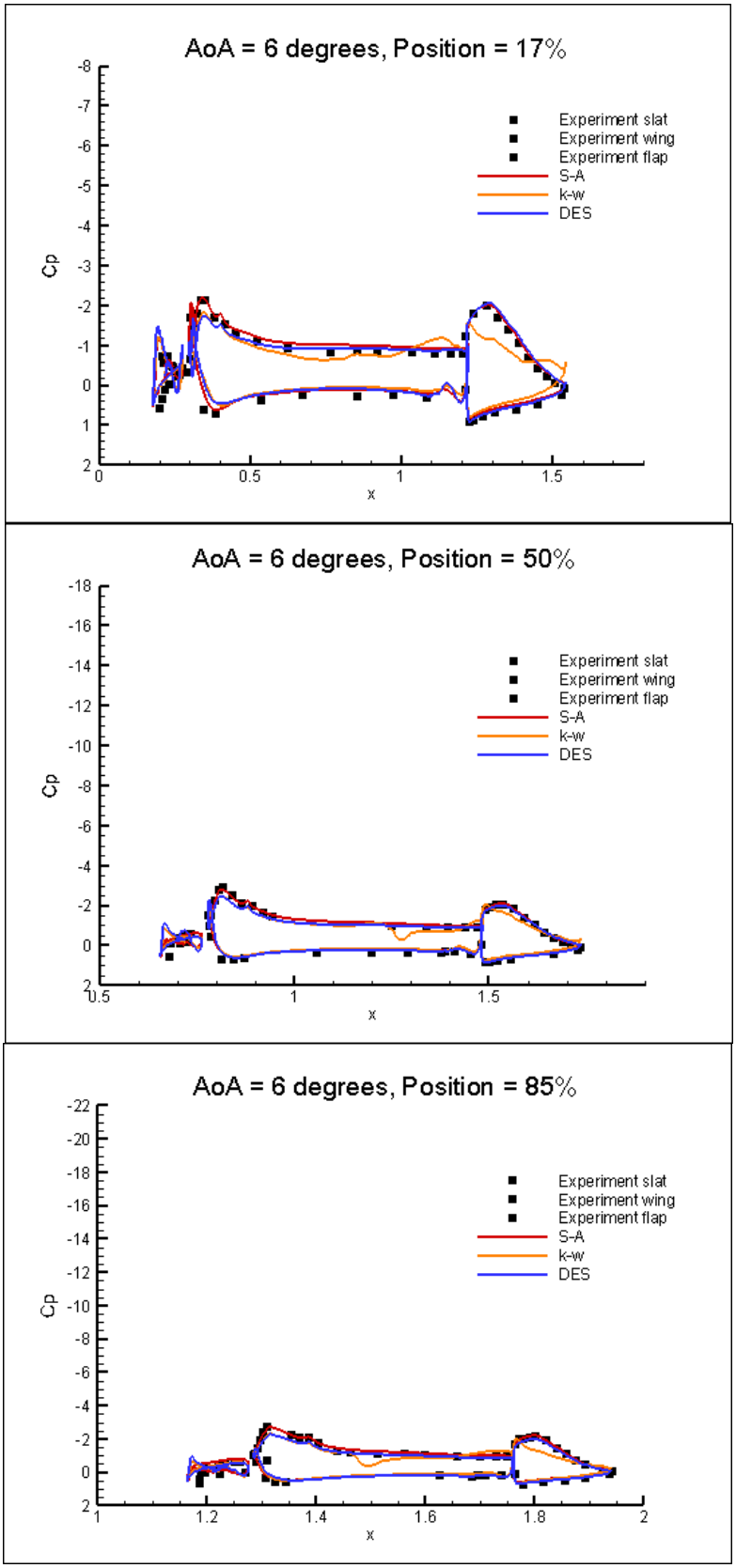

Figure 5.16 Pressure distribution at position ST17, ST50 and ST85 at AoA = 6°

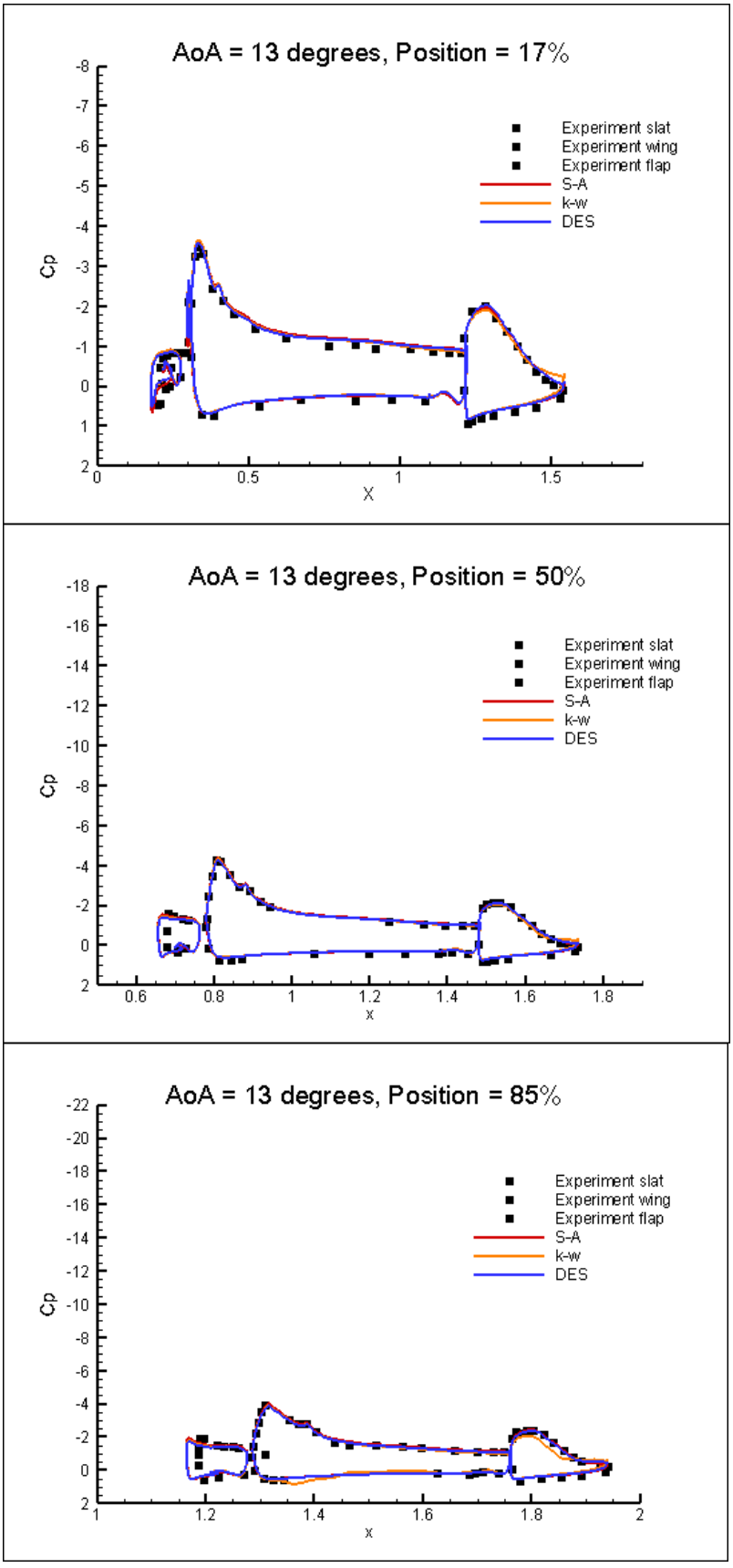

Figure 5.17 Pressure distribution at position ST17, ST50 and ST85 at AoA = 13°

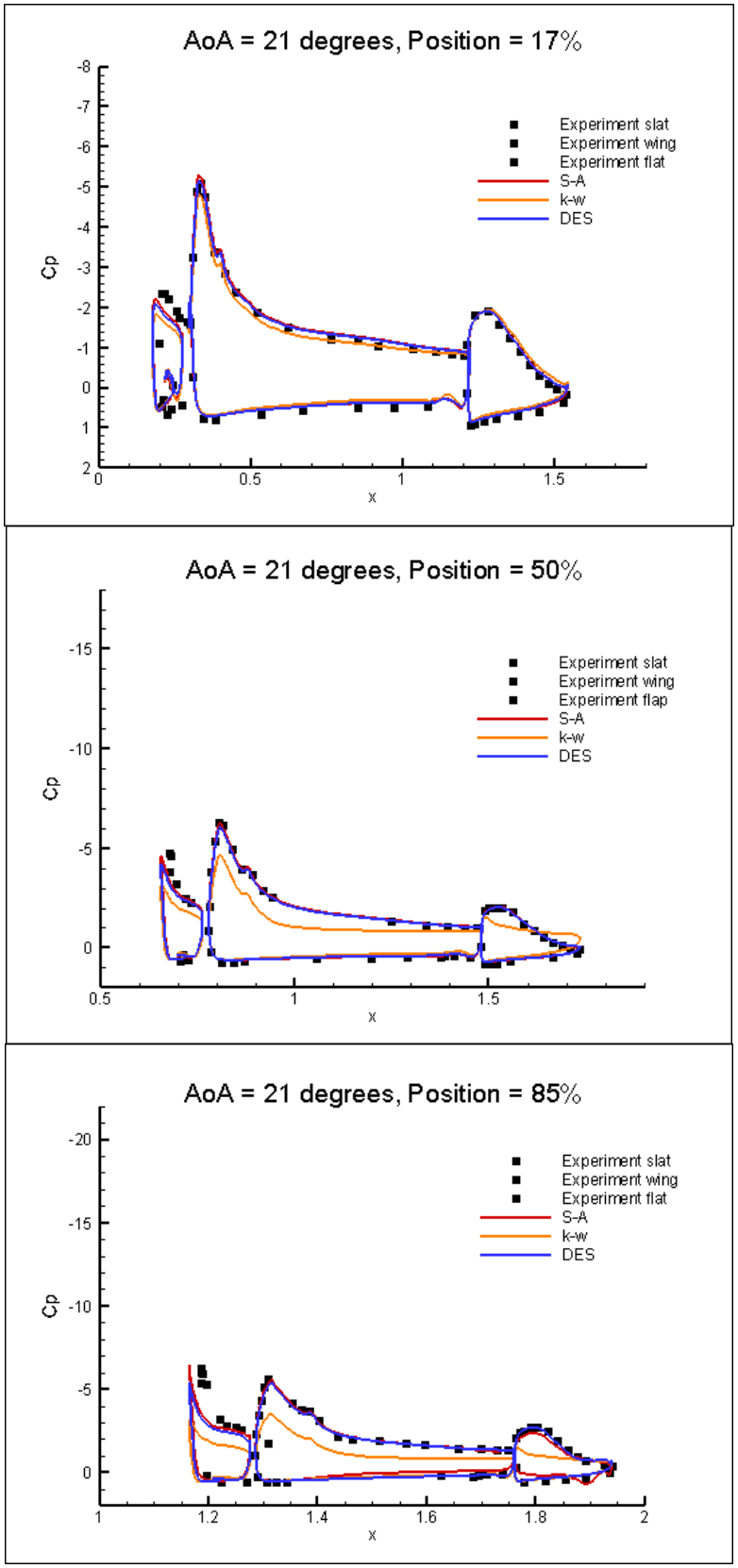

Figure 5.18 Surface Pressure distribution at position ST17, ST50 and ST85 at AoA = 21°

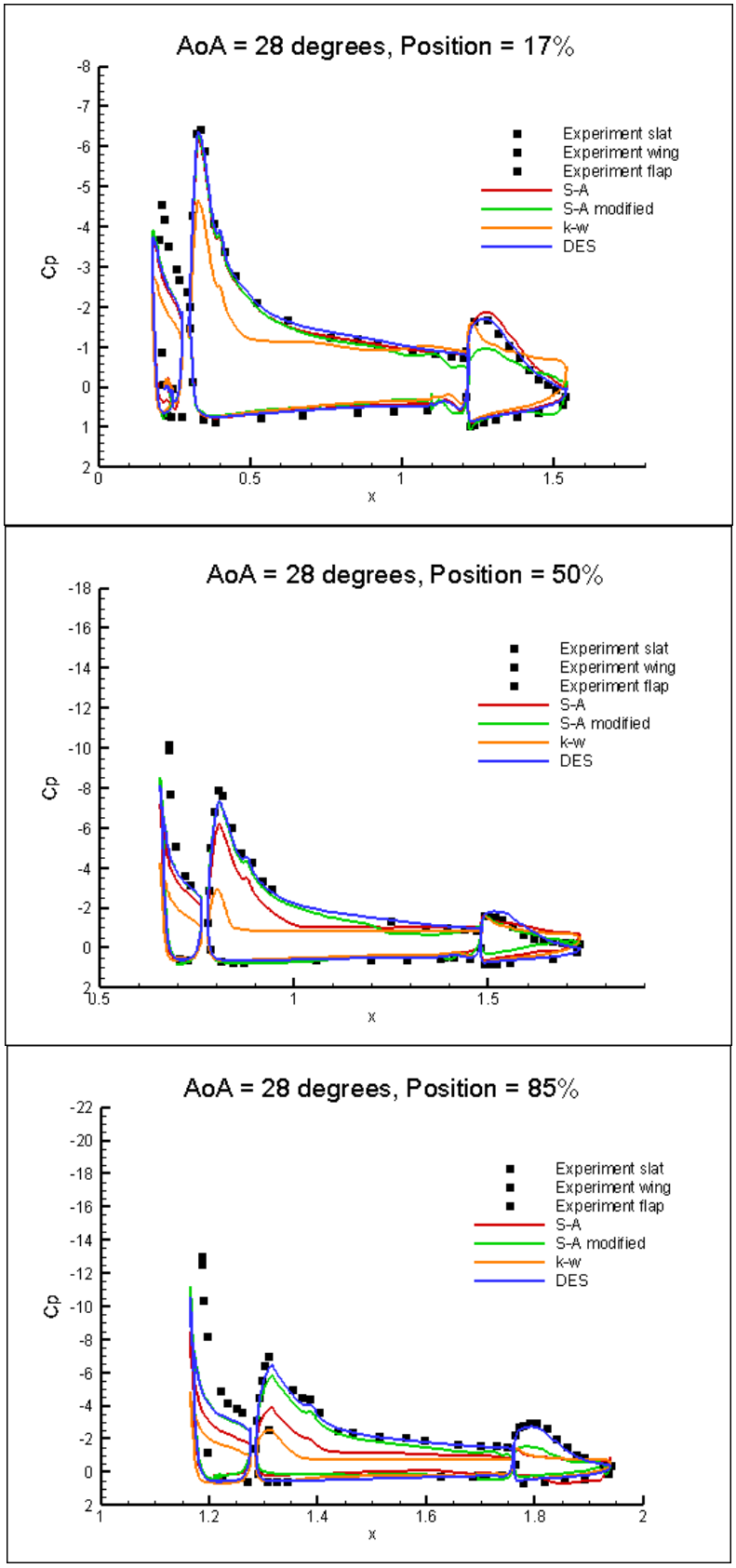

Figure 5.19 Surface Pressure distribution at position ST17, ST50 and ST85 at AoA = 28°

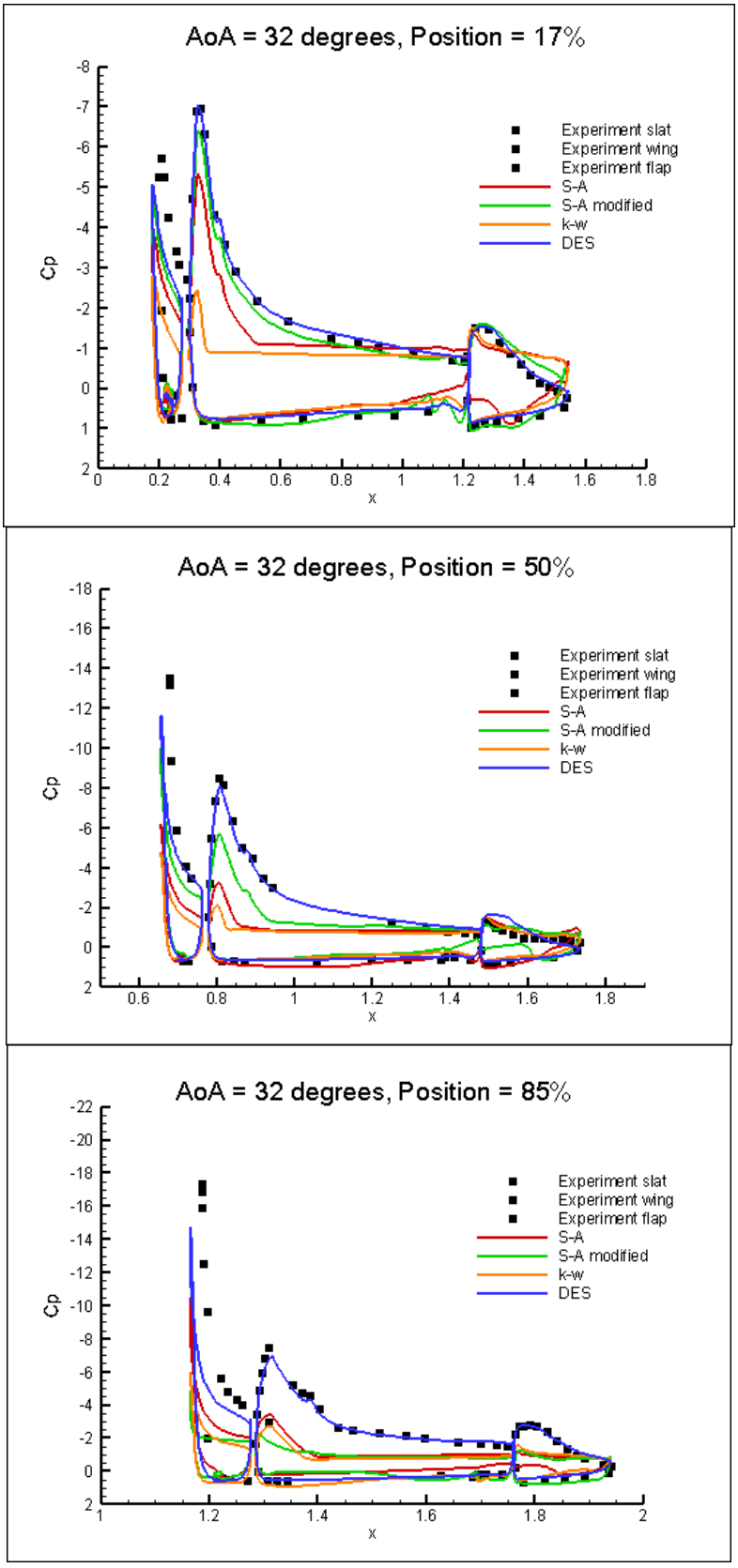

Figure 5.20 Surface Pressure distribution at position ST17, ST50 and ST85 at AoA = 32°

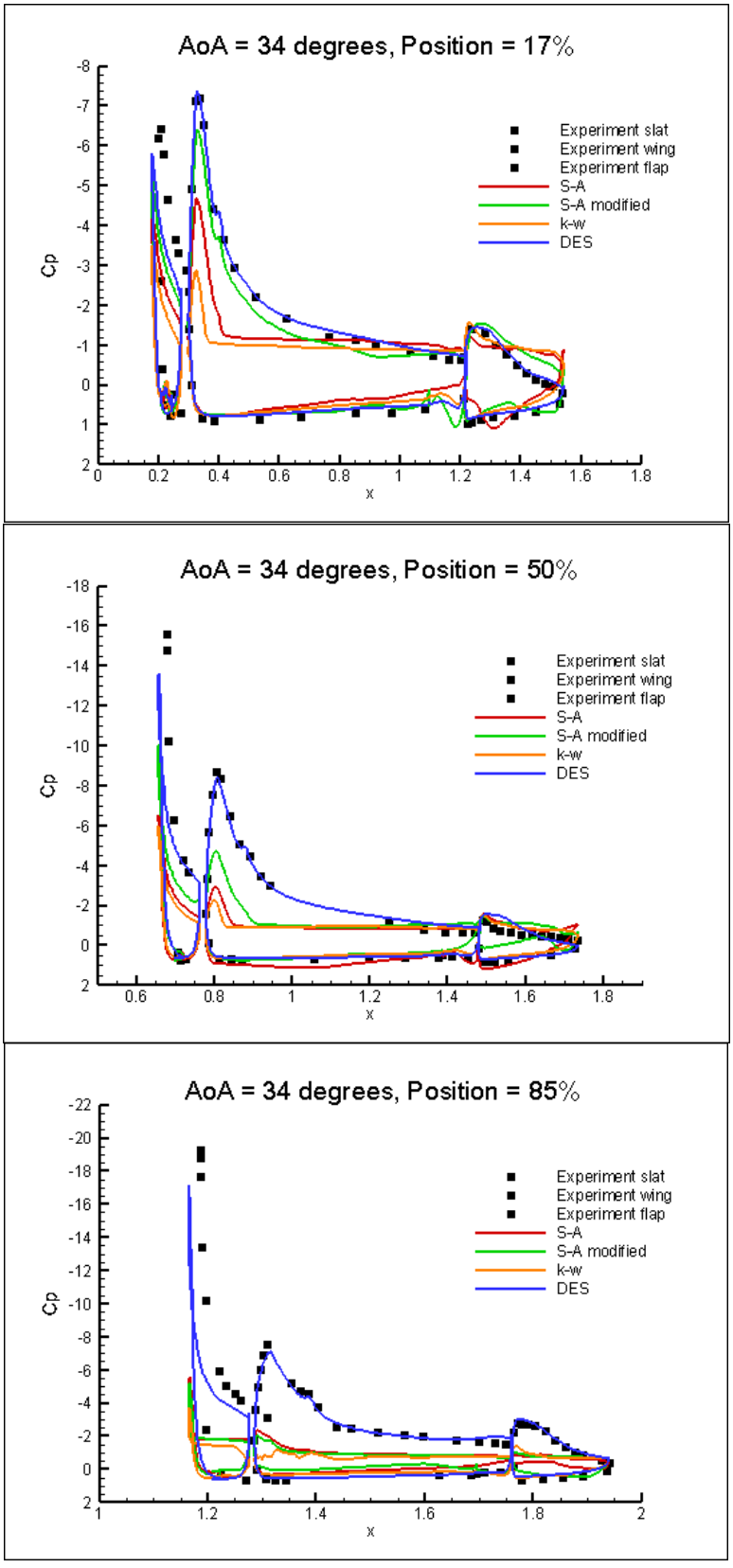

Figure 5.21 Surface Pressure distribution at position ST17, ST50 and ST85 at AoA = 34°

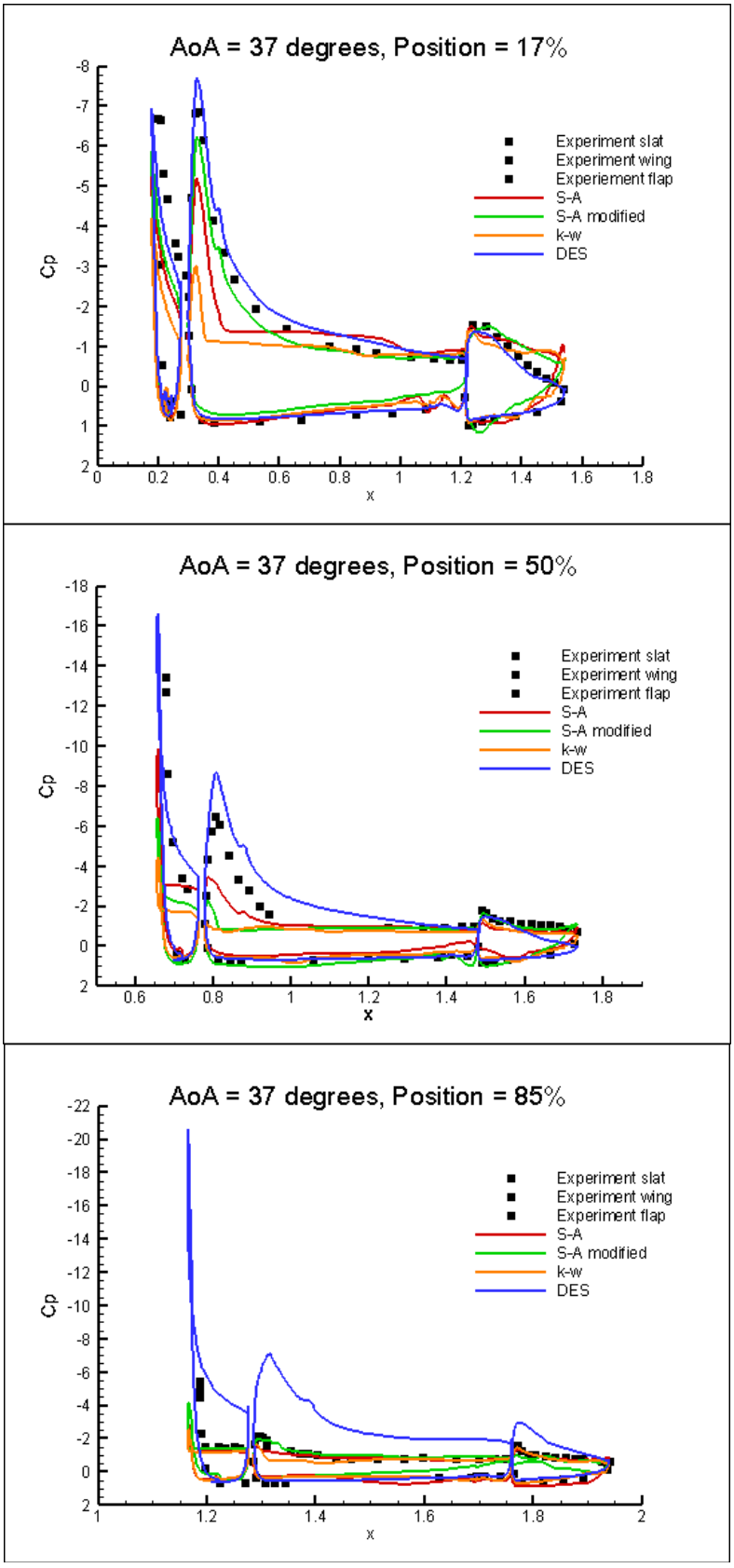

Figure 5.22 Surface Pressure distribution at position ST17, ST50 and ST85 at AoA = 37°

For surface pressure distribution at position ST50, C_p in this region shows a few differences compared to that in wing root region. DES shows a little lift loss at slat region when AoA = 21° and 28°, then starts to overpredict the slat upper surface pressure at AoA = 32°. Meanwhile, main wing surface pressure in the middle position behaves the same as before near the root, with an accurate lower surface C_p and an over-prediction of upper surface C_p. For this region, restarted S-A shows a decline in the ability to improve prediction accuracy, and behaves even worse than original S-A model at AoA = 37°. It is also important to note that S-A and k-ω model almost have the same pressure behaviour near stall, which may reveal that S-A tends to lose the advantages in separation flow prediction and arouses massive flow separation at high AoA. Almost all the failures in prediction for the three turbulence models happen at suction side, pressure side shows relatively accurate results, which may be inferred as the influence of mesh quality. Thus, for further research, some key locations on the upper surface should be paid more attention, such as the leading edge area of the slat and the main wing, and the wake region.

As for pressure distribution along a cross-section surface zone at wing tip (position ST85) is displayed at seven angles of attack for S-A, k-ω and DES model. Similarly, DES results basically agree with experimental data, except for AoA = 37° case, which fails to perform a post-stall pattern. Restarted S-A model can dramatically improve the pressure prediction thereby reduce the lift loss only when AoA = 28°. Besides, it can be observed very clearly that pressure distribution at wing tip presents a massive separation at high angles of attack near stall when two RANS models are applied in simulation, which happens more and more early from wing root to wing tip. In contrast, computational results for DES stay matched with experiment and show no separation, even at near stall condition. Interestingly, two RANS model reach a lot better agreement with the experimental results for the post-stall pressure distribution at AoA = 37°, while restarted S-A model fails to predict the pressure coefficient on the lower surface.

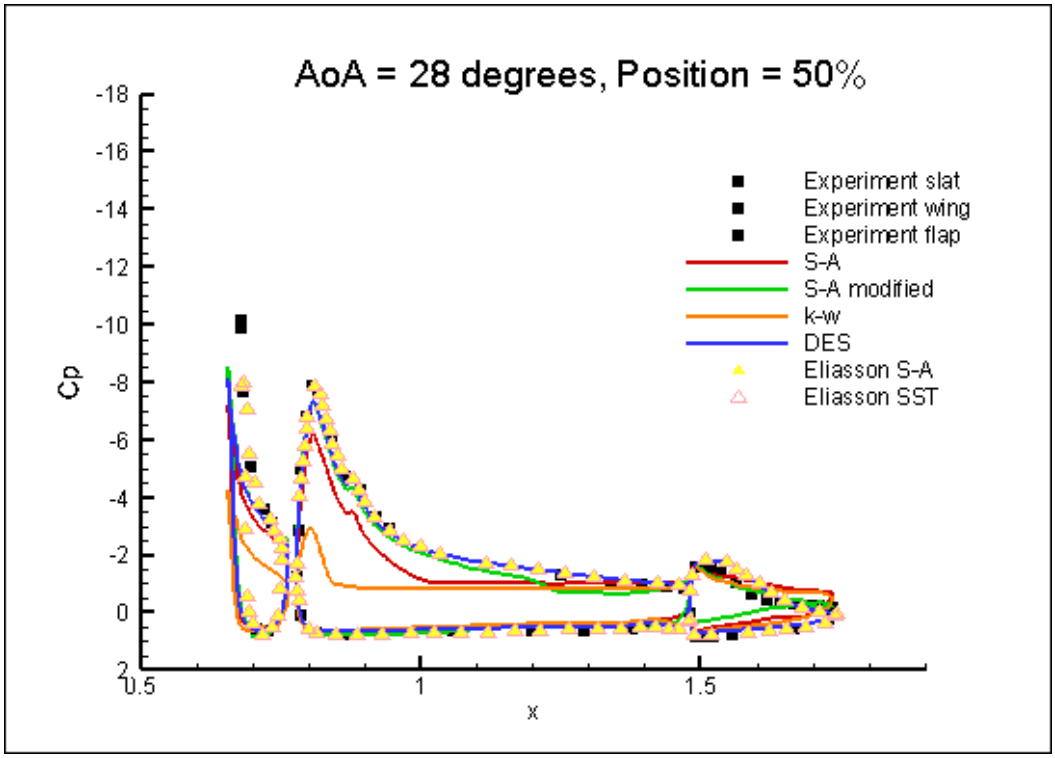

Figure 5.23 Pressure distribution at position ST50 when AoA = 28 degrees

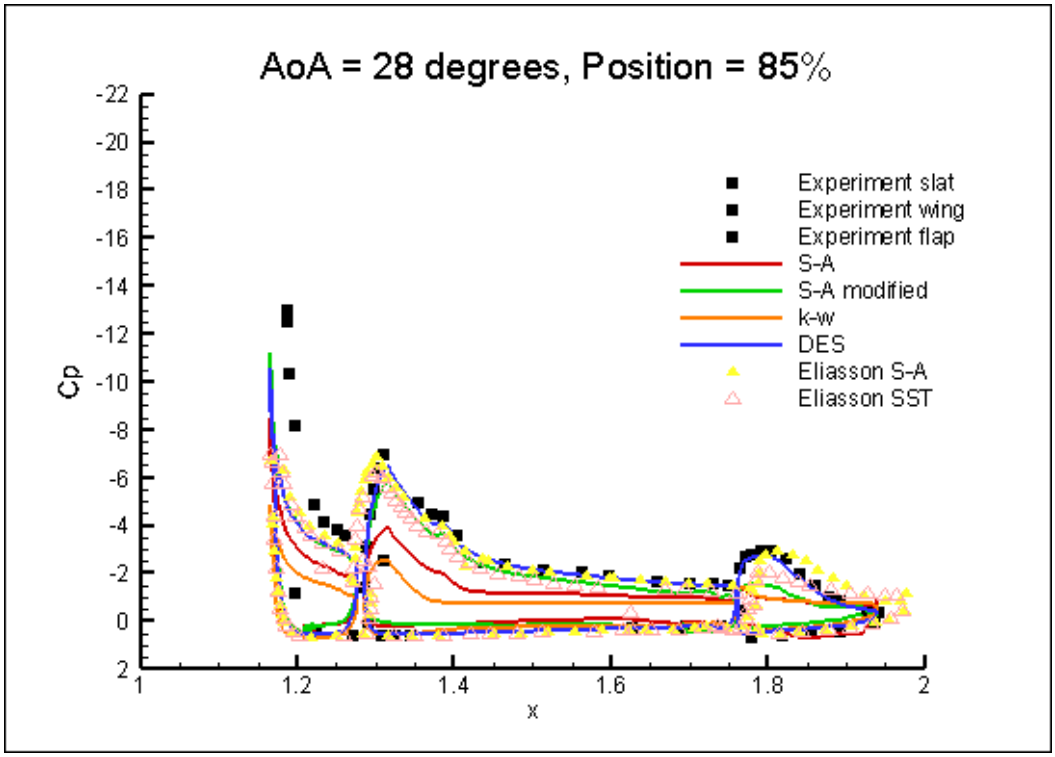

Figure 5.24 Pressure distribution at position ST85 when AoA = 28 degrees

Figure 5.23 and 5.24 respectively shows the C_p distribution at angle of attack equals to 28° at position ST50 and ST85. Two additional sets of data is presented for comparison, which is digitized from calculation of Eliasson et al with original S-A and Menter SST model without any transition specification. For midboard solution in figure 5.13, both models show a fair agreement with experimental results, especially for C_p over flap surface, where all the RANS models including the restarted S-A in this paper overpredict near the trailing edge region for both upper and lower surface. For outboard position pressure distribution, it can be clearly observed that only S-A solution coincides with the experimental results, while k-ω SST solution presents a little underprediction for the upper surface, but still gives a performance better than all the model applied in this paper except for DES model.

In summary, among three turbulence models, DES shows the best prediction results of pressure distribution on airfoil surface while k-ω shows the worst. However, when it comes to post-stall performance, DES tends to overpredict the pressure coefficient on the upper surface, while on the contrary S-A model and k-ω model presents similar data and in good agreement with the experimental ones. What else deserves to be mentioned is that restarted S-A model tends to lose its capability of delaying the separation when the position is closer to wing tip as well as the angle of attack is approaching to stall point. Meanwhile, some little wiggles happen on lower surface pressure distribution when restarted S-A model is applied.

5.5 Skin Friction Coefficient

Skin friction coefficient is a dimensionless parameter, which is defined as the ratio of local wall shear stress and dynamic pressure.[7]

$$\boldsymbol{C_f \equiv \frac{\tau}{q_\infty}}$$

(5-20)

where τ is the wall shear stress and q_∞ is dynamic pressure where

$$q_\infty = \frac{1}{2}\rho_\infty V_\infty^2$$

(5-21)

For the sake of clearly observing the flow separation position and transition patterns as well as further evaluating the capability of flow prediction near stall, skin friction coefficient C_f contour plot is obtained for S-A, k-ω SST, DES and restarted S-A models at AoA = 28°, 34° and 37°.

Figure 5.25 presents the skin friction coefficient contour plot on upper surface when AoA = 28°. As can be seen, DES and restarted S-A shows very little sign of separation, which is displayed as the yellow region in the plot.

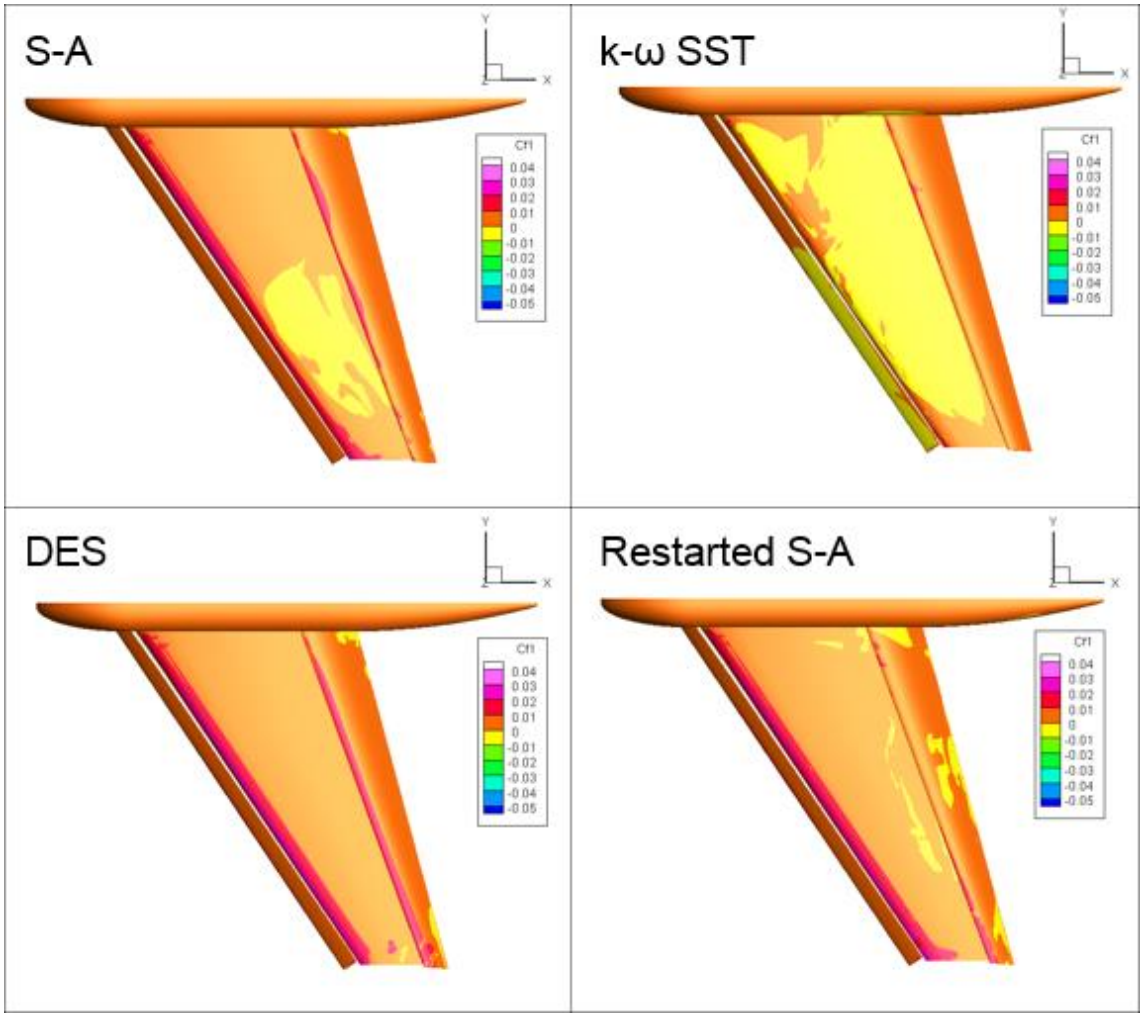

Figure 5.25 NASA Trap Wing Skin friction coefficient contour plot on upper surface when AoA = 28°

Compared to original S-A model, the restarted S-A model significantly delay the separation from half of the main wing tip section to a small number of scattered regions over the trailing edge of main wing and flap. Massive separation emerges when k-ω SST model is applied, which performs consistent results with pressure distribution.

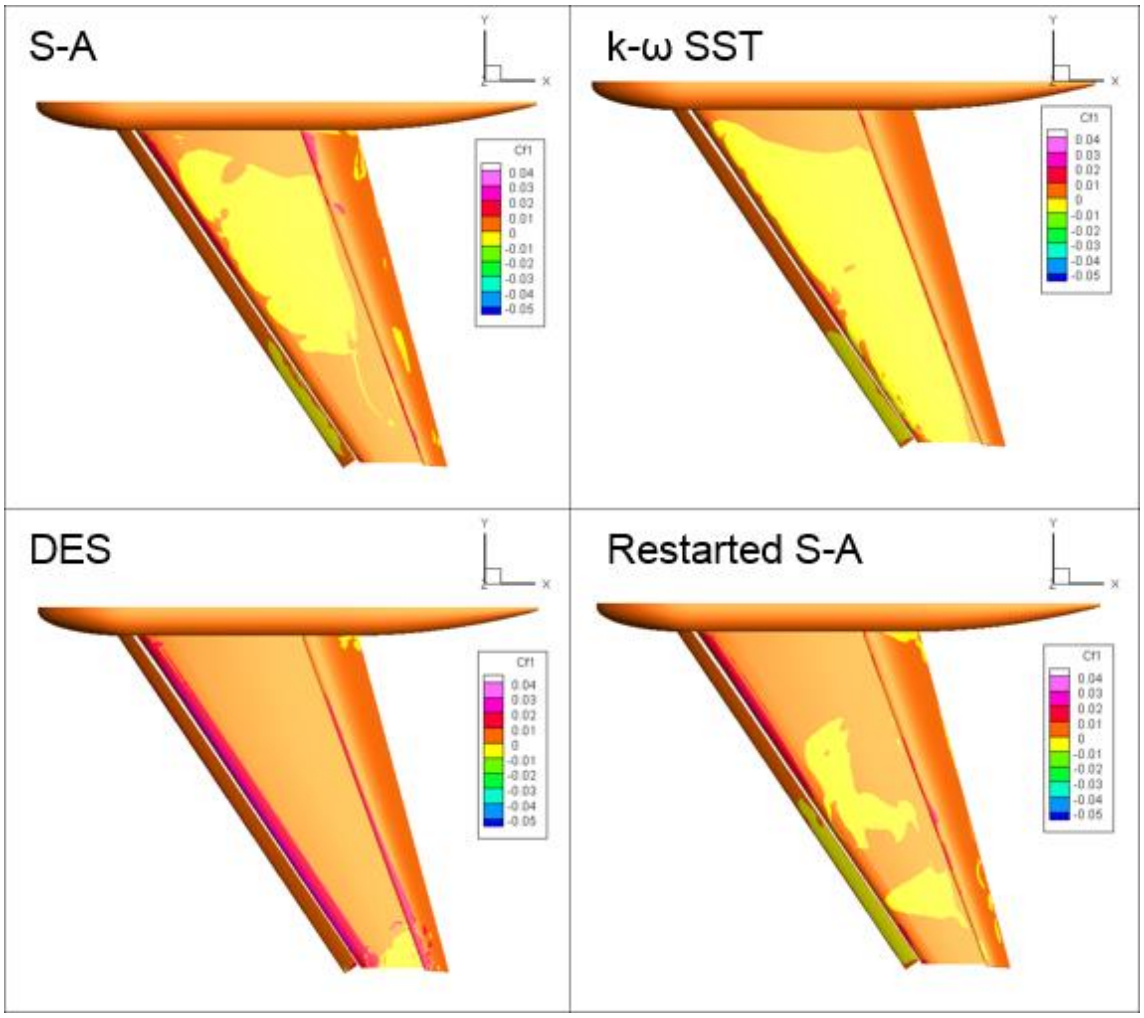

Figure 5.26 NASA Trap Wing Skin friction coefficient contour plot on upper surface when AoA =34°

Figure 5.26 shows the skin friction coefficient contour just before the stall happens when AoA = 34°. It can be easily observed that flow separation starts to spread when attack angle increases. DES begins to exhibit negative Cf value at wing tip section, which signifies that airflow detached from the surface near that position and leads to a little lift loss. Restarted S-A has damped effect on

separation postponement, while SST model completely fails to predict the flow separation occurrence with the yellow region almost covers all the upper surface.

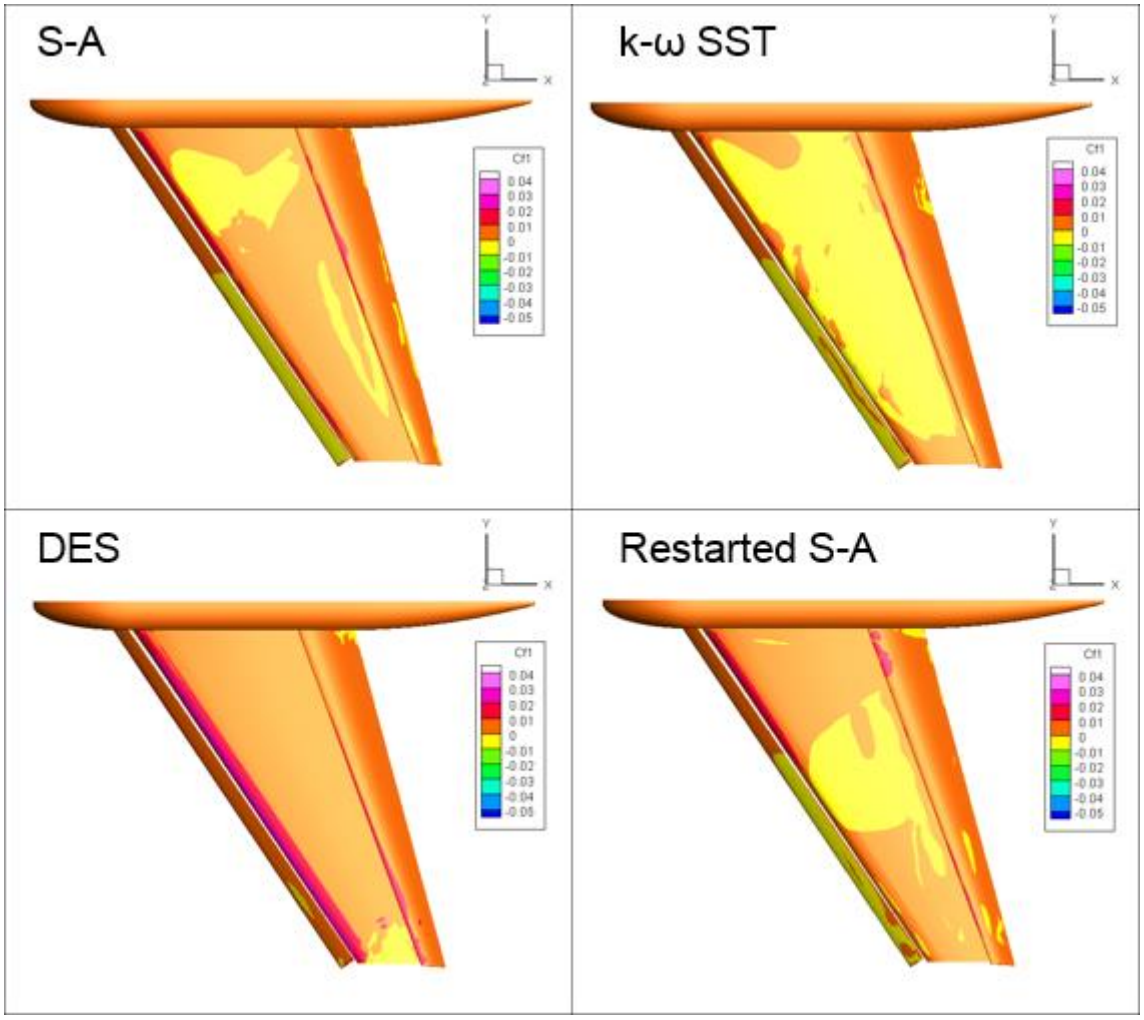

Figure 5.27 NASA Trap Wing Skin friction coefficient contour plot on upper surface when AoA =37°

Post-stall performance of skin friction coefficient is presented in Figure 5.27 at AoA = 37°. According to the lift coefficient curve, a strong decay of lift should happen due to massive separation when the angle of attack is higher than the critical AoA point, however, DES fails to show the post-stall phenomenon and continues to keep the separation in the range of wing tip. Analysing from experimental measurement of pressure coefficient, massive separation should happen over tip half of the airfoil on the upper surface. Both S-A and k-ω SST fails to predict the airflow over main wing leading edge region, which is in

agreement with the C_p distribution results. Compared to original S-A model, restarted S-A model, on the contrary, enlarges the separation area, which presents a reduction of flow prediction capability when AoA increases.

What's more, among all the turbulence models, only DES model simulation results show a transition onset near leading edge area for all the attack angles near stall. Restarted S-A model shows some transitions patterns when AoA = 28° but fails to predict when AoA gets higher.

Similar to pressure distribution plots, skin friction coefficient (C_f) distribution plots at three cross sections along the spanwise have been displayed as well in Figure 5.28 to 5.30. Plots are generated from the data that extracted from the slices cut at three positions. All four models are discussed in this situation with pitch angles are at 28°, 34° and 37°, respectively. By comparison with skin frictions contour, C_f distribution can illustrate the skin friction coefficient value covering both upper surface and lower surface. It has been universally acknowledged that $C_f < 0$ means the start of separation happens. Hence, for convenience of observation, a line of C_f=0 has been created for reference in each plot.

From Figure 5.28, when AoA = 28°, it can be obviously observed that separation for DES has mainly been concentrated in the leading edge region for each element and trailing edge region for main wing only. Figure 5.29 and 5.30 illustrate that the position of separation remain broadly consistent as the angle of attack increases. S-A performance is in accord with DES only when AoA = 28° around wing root region, while C_f value shows a rapider decline than DES for main element and flap leading edge, especially at higher incidences. Restart the case for S-A model can significantly raise the C_f value for upper surface, but it brings more separation for flow over wing tips on the contrary. K-omega model is the only method that gives a separation on both upper and lower surface. However, there is no obvious change for stagnation point from the C_f curve.

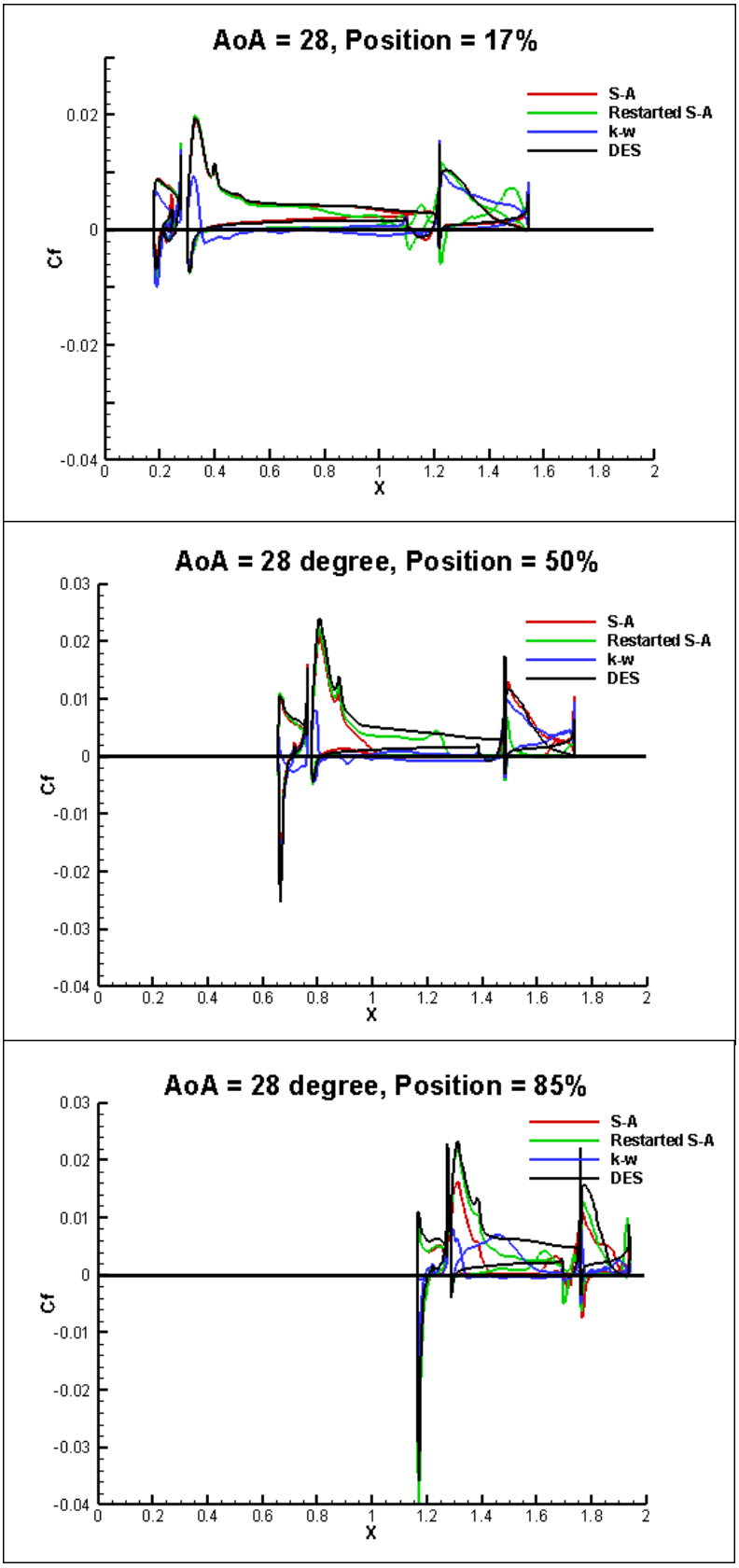

Figure 5.28 Skin friction coefficient plots at position ST17, ST50 and ST85 at AoA = 28°

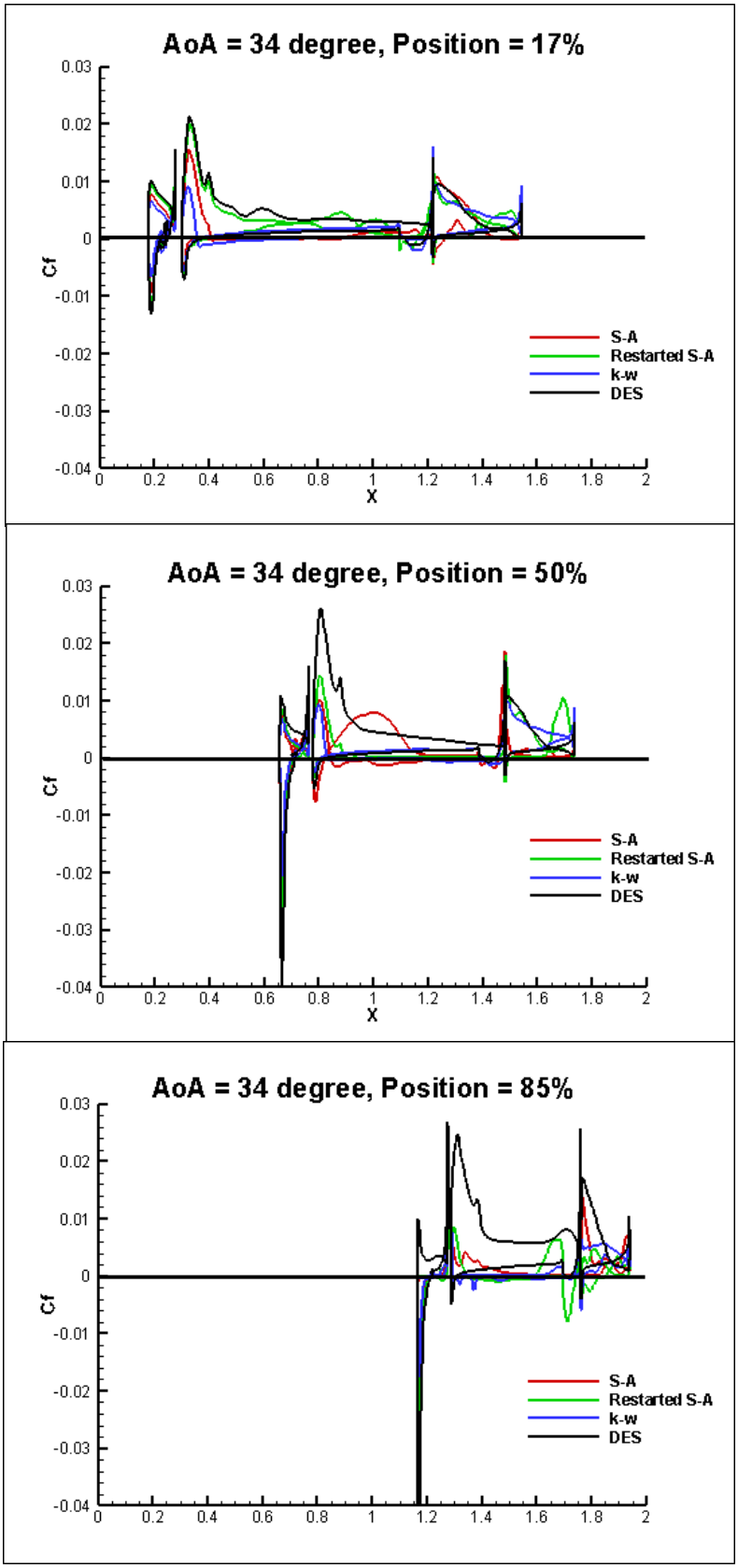

Figure 5.29 Skin friction coefficient plots at position ST17, ST50 and ST85 at AoA = 34°

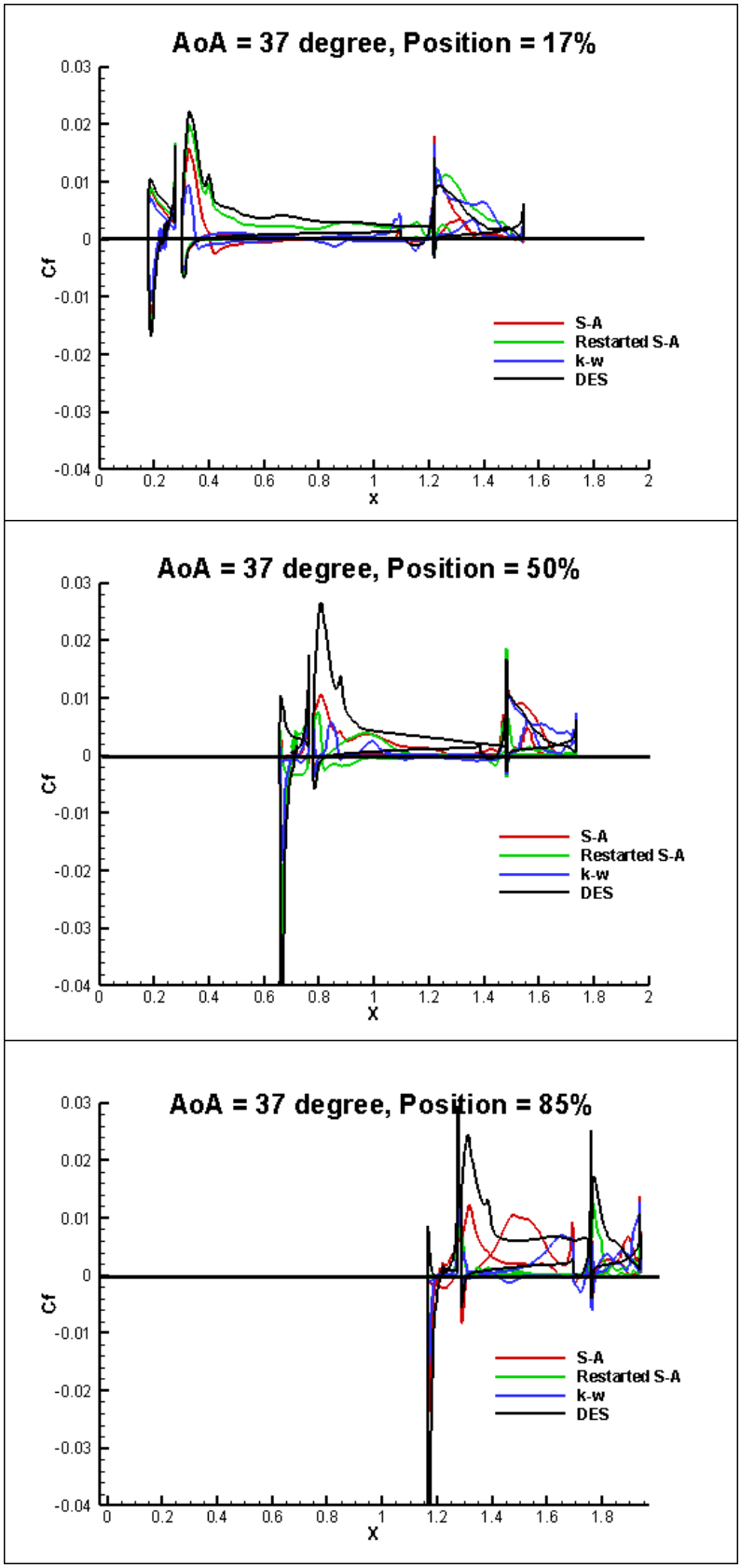

Figure 5.30 Skin friction coefficient plots at position ST17, ST50 and ST85 at AoA =37°

5.6 Total Pressure

In fluid dynamics, total pressure means the sum of static pressure and dynamic pressure[65]. Here in this paper, total pressure for the flow around the aircraft surface can be calculated from the following equation:

$$P_{total} = \mathrm{p} + \frac{1}{2}\rho v^2 \tag{5-22}$$

where p is the static pressure, ρ is the fluid density and v is the flow velocity.

Figure 5.31, 5.32 and 5.33 respectively illustrate the total pressure contour for S-A, restarted S-A and DES model at three cross-sections normal to x direction. The position of three cross section was determined to explore the wing tip vortex and side of body separation according to the workshop entries experience. From those three contours, facts can be found that the extent of total pressure loss is in concert with flow separation reflected in pressure distribution plots. Apart from the wing tip region, nearly no separation happens for both S-A and DES model when AoA = 21°. When the incidence is raised to 28°, both S-A and restarted S-A model gives a large separation over the upper surface for the region from midboard to outboard. Apparently, S-A with initialization from previous AoAs can supress the separation to some extent. Large total pressure loss that almost cover the whole wing area above is represented in post-stall contour when angle of attack is 37° for both S-A and the restarted S-A. Another thing that deserved to be paid attention is that small separations show up at the wing root region after the flap trailing edge, which is referred to as side of body separation, and the separation becomes greater when the restarted S-A model is put into effect.

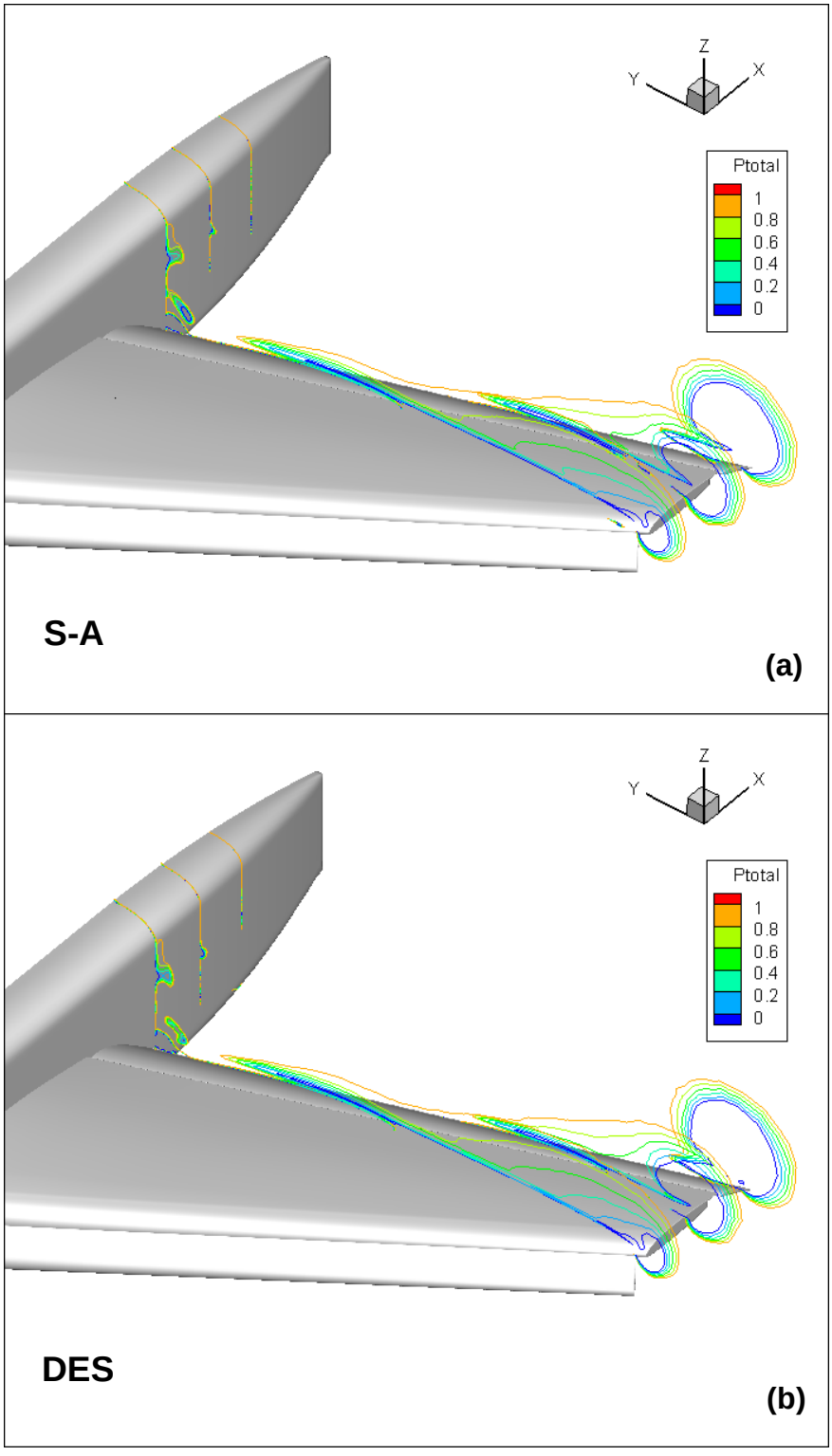

Figure 5.31 Total Pressure at three iso-surfaces for S-A model (a) and DES model (b) at AoA = 21°

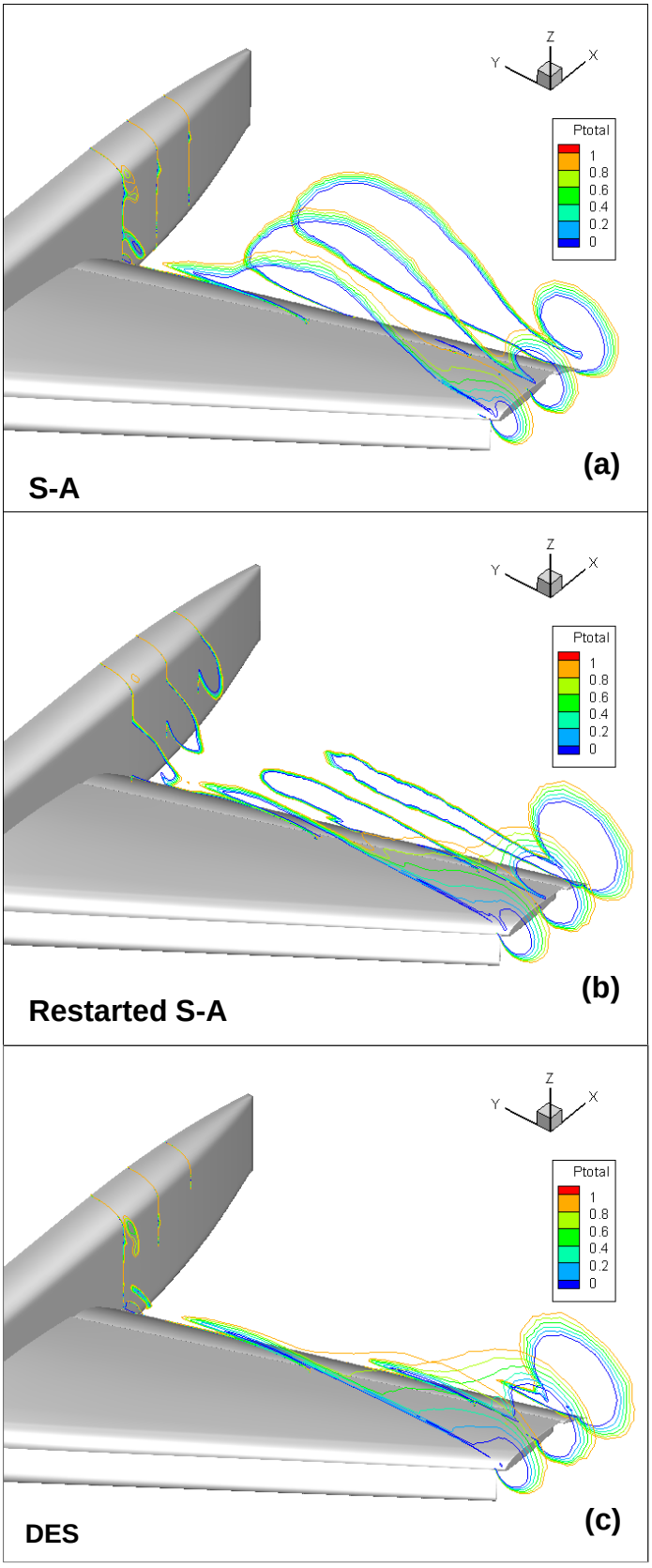

Figure 5.32 Total Pressure at three iso-surfaces for S-A model (a), restarted S-A (b) and DES model (c) at AoA = 28°

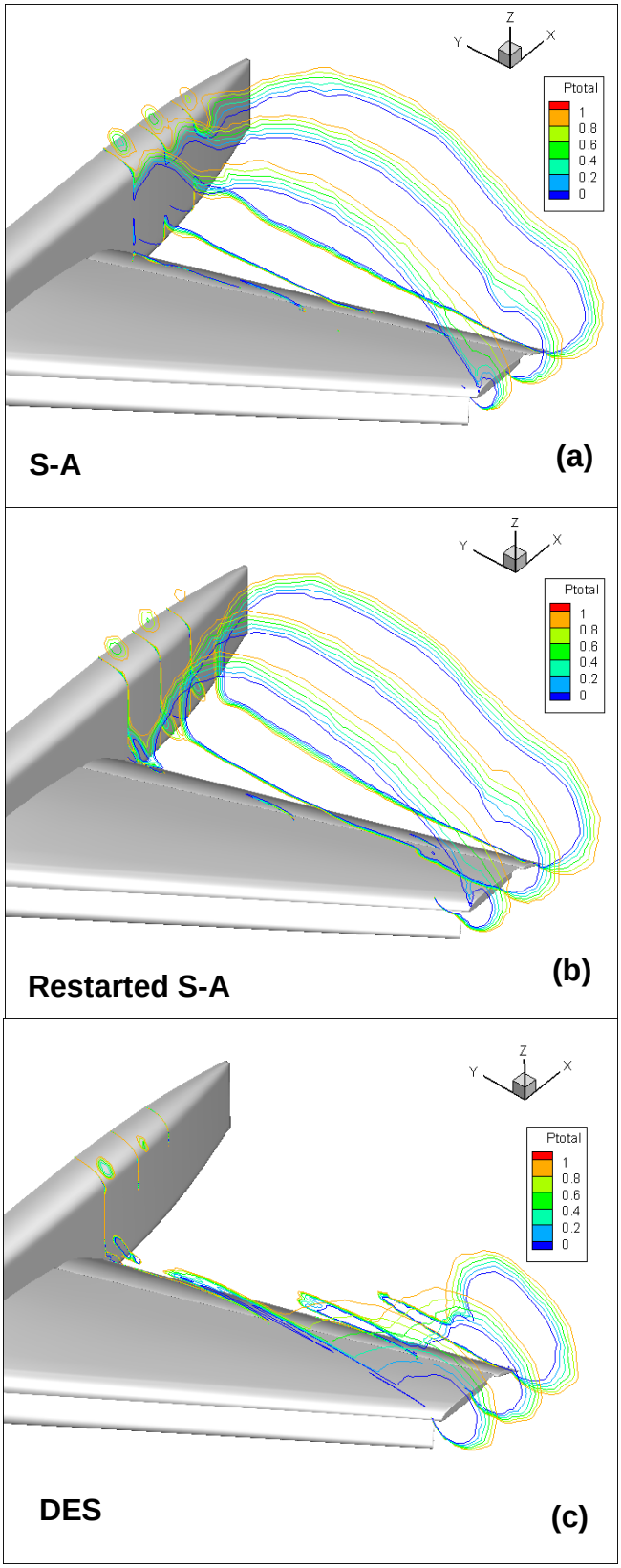

Figure 5.33 Total Pressure at three iso-surfaces for S-A model (a), restarted S-A (b) and DES model (c) at AoA = 37°

5.7 Velocity Streamline

For further investigation, velocity streamline is plotted by Tecplot360 and presented here in this subsection. Figure 5.34 to 5.36 represent the velocity streamline over the suction side of the wing elements for S-A, restarted S-A and DES model. Velocity streamlines at three angles of attack are revealed with regard to the performance shown in other flow characteristics, including 21°, 28° and 37°, which correspond to pre-stall performance without separation, with separation and post-stall performance. In those plots, the wing tip vortex can be clearly observed, with the vortex size increasing with pitch angle. Except for wing tip vortex, side of body separation can also be observed, which grows evident as the angle of attack increases. When AoA = 37°, both S-A model and restarted S-A model shows large separation while DES model on the contrary remains relative stability, which goes along with the increasing lift without any breakdown. However, same situation occurred for flow prediction in HiLiftPW-3, where some entries shows a later separation when comparing to measured data. If time permits, higher pitch angle case should be calculated for testing the capability of DES model in stall prediction.

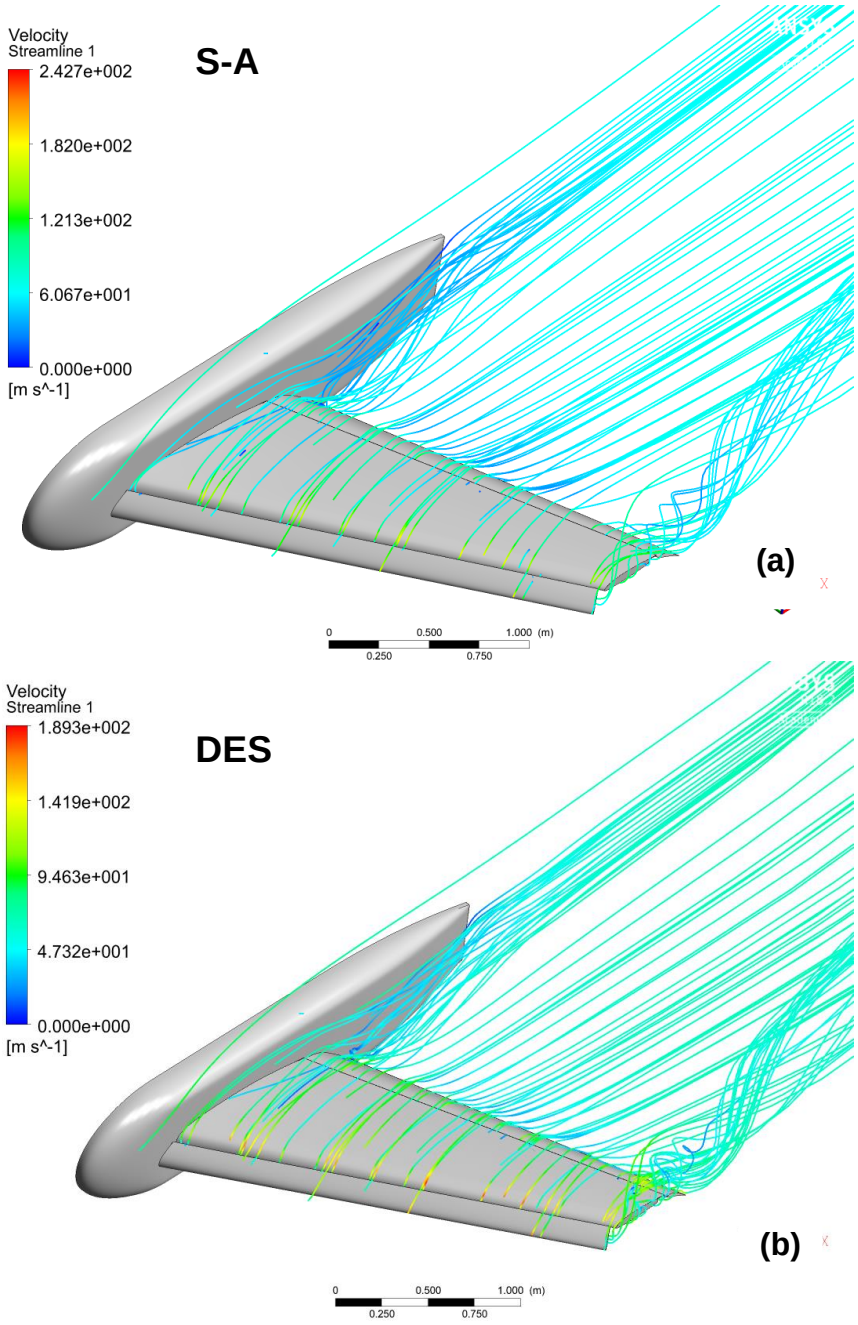

Figure 5.34 Velocity Streamline over the upper surface for (a) S-A model and (b) DES model at AoA = 21°

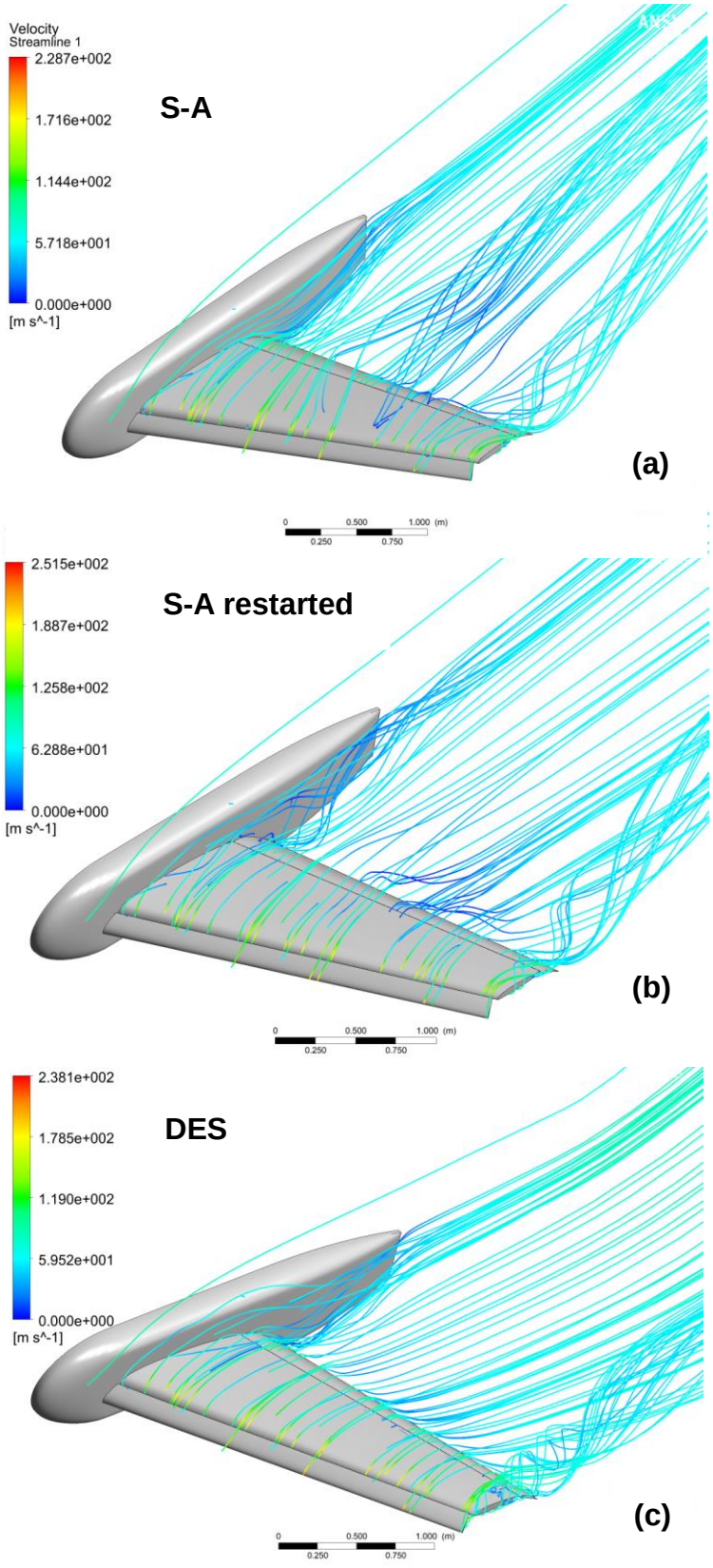

Figure 5.35 Velocity Streamline over the upper surface for (a) S-A, (b) S-A restarted and (c) DES model at AoA = 28°

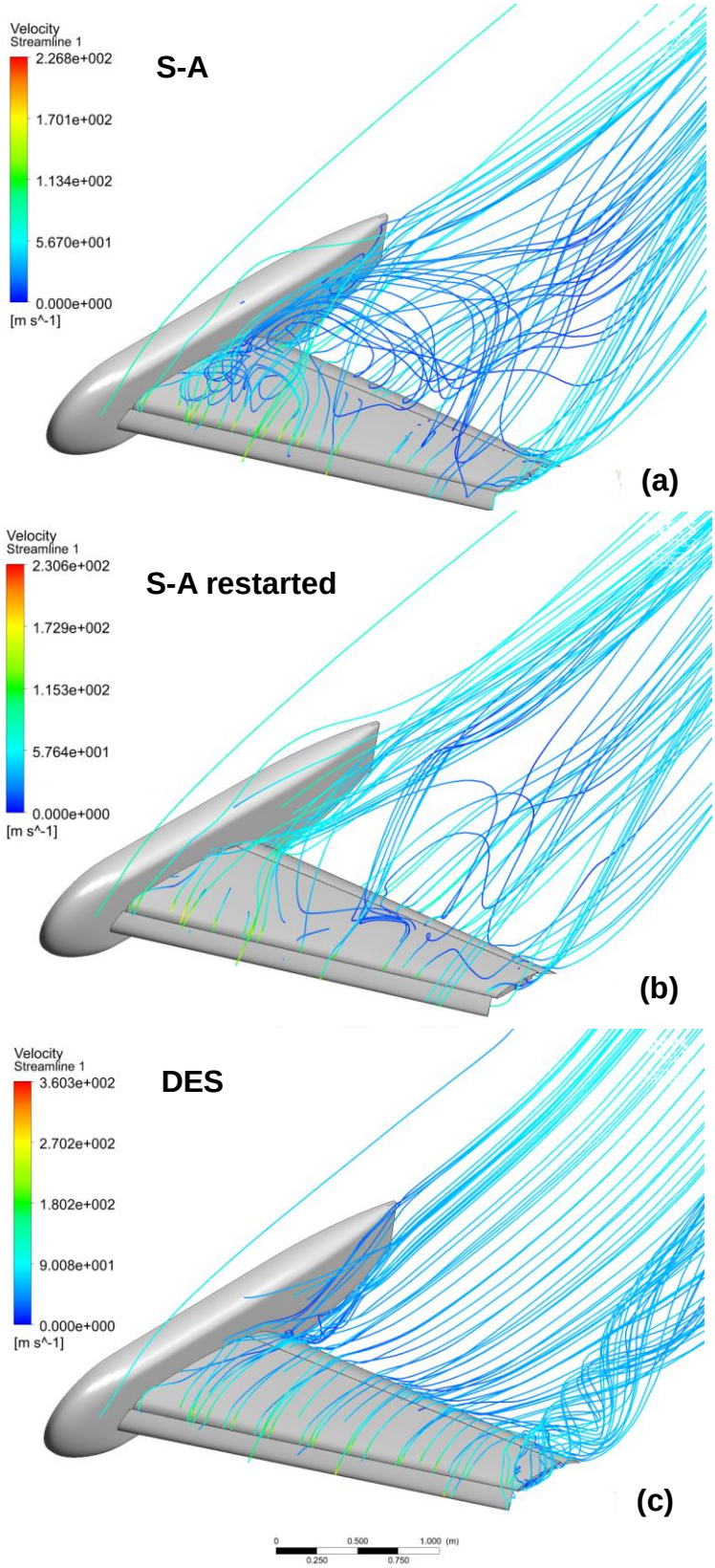

Figure 5.36 Velocity Streamline over the upper surface for (a) S-A, (b) S-A restarted and (c) DES model at AoA = 37°

6 Conclusion and Future Works

6.1 Conclusion

In this project, flow over NASA Trap Wing has been predicted by two RANS models and DES model using Pointwise for meshing, ANSYS Fluent for calculation, and Tecplot360 together with Microsoft Excel for data post processing.

The Trap Wing geometry is provided by the 1st AIAA High lift Prediction Workshop (HiliftPW-1) as a three-element airfoil with slat deployed angle of 30° and flap deployed angle of 25°. Meanwhile, in consideration of computational efficiency, HiliftPW-1 also published several gridding guidelines for different grid levels to guarantee the y+ value and mesh quality. Three different densities of mesh are generated based on the guideline with the cell number of 8 million, 22 million and 42 million, respectively. Two test cases are studied in this project. The first test case is called grid convergence study, where coarse, medium and fine mesh are required to run for grid convergence assessment only using S-A model. The second test case is called flap deflection prediction study, where only medium mesh from the grid convergence study is chosen to predict the flow over the NASA Trap Wing with S-A, k-ω and DES models for comparison and exploration. For further research, S-A model is initialized from the converged solution of lower angle of attack, namely, restarted S-A in this project, which, according to the participants of HiliftPW-1, can effectively avoid the massive separation near stall.

The results show that among three turbulence models, DES shows the best prediction results of both forces, moment coefficient and pressure distribution on airfoil surface while k-ω shows the worst. S-A model shows a premature stall in lift coefficient plot, and the restarted S-A can only delay the stall to a very limited extent. However, when it comes to post-stall performance, DES tends to overpredict the pressure coefficient on the upper surface, which leads to a failure to lift drop that should have happened in that situation. On the contrary, S-A model and k-ω model present data in good agreement with the experimental ones after critical AoA point. From force and moment curve, a lack of agreement at low

pitch angles happens for k-ω SST and DES model, possible reasons could be deduced that high lift system is out of optimum conditions, or the solution is lack of convergence due to closed re-circulation bubbles in flap and slat cove regions. The failure of RANS approaches in this paper What's more, primary cause may be the low mesh quality due to high skewness at trailing edge and leading edge of the elements. The failure of RANS approaches in this paper may result in part the essence of the model that cannot accurately capture the large-scaled motions at high incidence, where in the actual situation turbulent are governed by both small- and large-scaled motion.

It should also be mentioned that after restarting from the converged solutions of lower AoAs, S-A model tends to lose its capability of delaying the flow separation when the position as the angle of attack is approaching to stall point, as can be seen from force curve. Pressure distribution plots also reveals that problem of restarted S-A method lied in the wing tip region and aggravate the wing tip vortex, which is further proven in the total pressure contour and velocity streamline. Meanwhile, some little wiggles happen on lower surface pressure distribution and oscillation emerges during iteration process when restarted S-A model is applied.

From research in this paper, experience can be learned that the capability of DES with S-A model as its RANS part has been explored in commercial software such as ANSYS Fluent, which proves its feasibility in handling the flow prediction for multi-elements airfoil as a very promising approach. However, no post-stall behaviour is represented by DES model, which may be caused by DES for either no capability to capture the flow separation and large vortex shedding or predict the maximum lift coefficient at higher AoA value, which needs to be figured out as a future research topic. S-A model shows a relative good high-lift system prediction results as well, but it can only handle the low pitch angle cases and gives massive separation when angles of attack are high. Solutions can be taken to solve the early separation issue such as reinitializing the case with data interpolated from lower AoA case, which proves to offer limited help in this paper. K-omega SST model without any variant is not recommended in high-lift prediction case.

6.2 Future Work

As the limitation of time and technology, there are still some further researches that should be investigated in this subsection.

Firstly, as the mesh is not good enough through examination, the capability of more key location mesh adaption should be explored, such as the leading edge region of the main wing, wake region for every element of the airfoil and the wing tip region. From pressure distribution results of section 4.2, failure of prediction happen at the locations mentioned above. When the possibility of turbulence model influence is ruled out, mesh refinement will be the next choice for prediction accuracy enhancement.

Secondly, URANS (Unsteady RANS) for SA and k-ω SST models should be calculated for comparison to DES model results. This approach can filter out interference from different influences between steady and unsteady time solvers.

Thirdly, since DES shows no stall performance when AoA = 37°, high angle of attack case after AoA = 37° should be taken into consideration to check whether DES has no ability to perform post-stall flow field or the occurrence of the stall is simply postponed by DES.

Furthermore, the span of pitch angle chosen for calculation, which are specified at low values is a bit large, computations should start from low pitch angles and gradually ramp-up to higher-ones to better mimic the experiment trends.

Last but not least, for further computations, more recent workshop configurations that has a better, more comprehensive experimental database should be taken into the scope of the research, instead of the “clean” one in this paper without any bracket/fairings/nacelle.

REFERENCES

1. Smith AM. High-Lift Aerodynamics. Journal of Aircraft. 1975; 12(6): 501–530.

2. Page FH. The Handley Page Wing. The Aeronautical Journal. : p263.

3. Rumsey CL., Ying SX. Prediction of high lift : review of present CFD capability. 2002. 145-180 p.

4. Of O. Summary of the First AIAA CFD High-Lift Prediction Workshop. 2011; 48(6). Available at: DOI:10.2514/1.C031447

5. Nicolai LM., Carichner GE. Fundamentals of Aircraft and Airship Design: Volume 1-Aircraft Design. American Institute of Aeronautics and Astronautics; 2010. Available at: DOI:https://doi.org/10.2514/4.867538

6. Flap(aeronautics)-Wikipedia. Available at: https://en.wikipedia.org/wiki/Flap_(aeronautics)

7. Anderson JD. Fundamentals of Aerodynamics. Fifth Edit. New York: McGraw-Hill; 2011. 1106 p. Available at: DOI:10.1017/CBO9781107415324.004

8. Ying SX., Spaid FW., Mcginley CB., Rumsey CL. Investigation of confluent boundary layers in high-lift flows. Journal of Aircraft. 1999; 36(4): 550–562. Available at: DOI:10.2514/6.1998-2622

9. Thomas FO., Nelson RC. An Experimental Investigation of the Confluent Boundary Layer on a High-Lift System. California USA; 1998.

10. Hannon JA., Washburn AE., Jenkins LN., Watson RD. Trapezoidal Wing Experimental Repeatability and Velocity Profiles in the 14- by 22-Foot Subsonic Tunnel (Invited). 50th AIAA Aerospace Sciences Meeting including the New Horizons Forum and Aerospace Exposition. Nashville, Tennessee; 2012. pp. 1–15. Available at: DOI:10.2514/6.2012-706

11. Hannon JA. Trap Wing Experimental Summary , Geometry , and Repeatability. 1st AIAA CFD High Lift Prediction Workshop. Chicago, Illinois; 2010. pp. 1–53.

12. Geometries of 1st AIAA CFD High Lift Prediction Workshop. Available at: https://hiliftpw.larc.nasa.gov/Workshop1/geometries.html

13. Shankara P., Snyder D. Numerical Simulation of High Lift Trap Wing using STAR-CCM+. 30th AIAA Applied Aerodynamics Conference. New Orleans, Louisiana; 2012. pp. 1–14.

14. Crippa S., Melber-wilkending S., Rudnik R. DLR Contribution to the First High Lift Prediction Workshop. 49th AIAA Aerospace Sciences Meeting including the New Horizons Forum and Aerospace Exposition. Orlando, Florida; 2011. pp. 1–22.

15. Rumsey CL., Lee-rausch E., Slotnick JP. Lessons Learned and Future Goals of the High Lift Prediction Workshops. Specialists Meeting on Progress and Challenges in Validation Testing for Computational Fluid Dynamics. Avila, Spain; 2016. pp. 1–14.

16. Eliasson P., Peng S., Hanifi A. Improving the Prediction for the NASA High-Lift Trap Wing Model. 49th AIAA Aerospace Sciences Meeting including the New Horizons Forum and Aerospace Exposition. Orlando, Florida; 2011. pp. 1–16. Available at: DOI:10.2514/6.2011-867

17. Eliasson P., Defence S. Influence of Transition on High-Lift Prediction for the NASA Trap Wing Model. 29th AIAA Applied Aerodynamics Conference. Honolulu, Hawaii; 2011. pp. 1–12. Available at: DOI:10.2514/6.2011-3009

18. Park MA., Lee-rausch EM., Rumsey CL. FUN3D and CFL3D Computations for the First High Lift Prediction Workshop. 49th AIAA Aerospace Sciences Meeting including the New Horizons Forum and Aerospace Exposition. Orlando, Florida; 2011. pp. 1–24.

19. Rumsey CL., Lee-Rausch EM. NASA Trapezoidal Wing Computations Including Transition and Advanced Turbulence Modeling. 30th AIAA Applied Aerodynamics Conference. New Orleans, Louisiana; 2012.

20. Pandya MJ., Abdol-Hamid KS. CFD Computations for a Generic High-Lift Configuration Using TetrUSS. 29th AIAA Applied Aerodynamics Conference. Honolulu, Hawaii; 2011. pp. 1–21.

21. Rumsey CL., Slotnick JP. Overview and Summary of the Second AIAA High-Lift Prediction Workshop. Journal of Aircraft. 2015; 52(4): 1006–1025. Available at: DOI:10.2514/1.C032864

22. Mavriplis D., Long M., Lake T., Langlois M. NSU3D Results for the Second AIAA High-Lift Prediction Workshop. Journal of Aircraft. 2015; 52(4): 1063–1081. Available at: DOI:10.2514/1.C033042

23. Rudnik R., Melber-wilkending S., Huber KC., Crippa S. DLR's contributions to the High Lift Prediction Workshop Series. Deutscher Luft- und Raumfahrtkongress. 2016. pp. 1–10.

24. Chitale KC., Rasquin M., Martin J., Jansen KE. Finite Element Flow Simulations of the EUROLIFT DLR-F11 High Lift Configuration. 52nd Aerospace Sciences Meeting. Maryland; 2014. pp. 1–15. Available at: DOI:10.2514/6.2014-0749

25. Murayama M., Yamamoto K., Ito Y. Japan Aerospace Exploration Agency Studies for the Second High-Lift Prediction Workshop. Journal of Aircraft. 2015; 52(4): 1026–1041. Available at: DOI:10.2514/1.C033158

26. Coder JG. OVERFLOW Analysis of the DLR-F11 High-Lift Configuration Including Transition Modeling. Journal of Aircraft. 2015; 52(4): 1082–1097. Available at: DOI:10.2514/1.C033145

27. Glasby RS., Erwin JT. HPCMP CREATE ^{TM} -AV Kestrel HiLiftPW3 Results PID 004. the 3rd AIAA High Lift Prediction Workshop. Denver, Colorado; 2017. pp. 1–30.

28. Luo A., Lee P. TotalSim US Contributions to HiLiftPW-3 using OpenFOAM and FUN3D. the 3rd AIAA High Lift Prediction Workshop. Denver, Colorado; 2017. pp. 1–65.

29. Spalart PR. Strategies for turbulence modelling and simulations. International Journal of Heat and Fluid Flow. 2000; 21: 252–263.

30. Ito Y., Murayama M., Yamamoto K., Tanaka K., Hirai T. TAS Code Results for the Third High Lift Prediction Workshop. the 3rd AIAA High Lift Prediction Workshop. Denver, Colorado; 2017. pp. 1–33.

31. Jensen J., Denison M., Stich G., Housman J., Kiris C. LAVA Contribution to HiLiftPW-3. the 3rd AIAA High Lift Prediction Workshop. Denver, Colorado; 2017. pp. 1–22.

32. Spalart PR. Detached-Eddy Simulation. 2008; : 181–204. Available at: DOI:10.1146/annurev.fluid.010908.165130

33. Travin A., Shur M., Strelets M. Detached-Eddy Simulations Past a Circular Cylinder. 2000; : 293–313.

34. Spalart PR., Jou W-H., Strelets MK., Allmaras SR. Comments on the feasibility of LES for wings, and on a hybrid RANS_LES approach. In: Liu C, Liu Z (eds.) the First AFOSR International Conference on DNS/LES. Ruston, Louisiana, USA: Greyden Press; 1997. pp. 137–147.

35. Spalart PR., Deck S., Shur ML., Squires KD., Strelets MK., Travin A. A new version of detached-eddy simulation , resistant to ambiguous grid densities. Theory Computational Fluid Dynamics. 2006; 20: 181–195. Available at: DOI:10.1007/s00162-006-0015-0

36. Shur ML., Spalart PR., Kh M., Travin AK. A hybrid RANS-LES approach with delayed-DES and wall-modelled LES capabilities. International Journal of Heat and Fluid Flow. Elsevier Inc.; 2008; 29(6): 406–417. Available at: DOI:10.1016/j.ijheatfluidflow.2008.07.001

37. Brunet V., Deck S. Zonal-Detached Eddy Simulation of Transonic Buffet on a Civil Aircraft Type Configuration. 2008; (2003): 182–191.

38. Srinivasan R., Bowersox RDW. Transverse Injection Through Diamond and Circular Ports. AIAA Journal. 2008; 46(8): 1944–1962. Available at: DOI:10.2514/1.29253

39. Simon F., Deck S., Guillen P., Cedex C. Zonal-Detached-Eddy Simulation of Projectiles in the Subsonic and Transonic Regimes. 2007; 45(7). Available at: DOI:10.2514/1.26827

40. Nayyar P., Barakos GN., Badcock KJ. Numerical study of transonic cavity flows using large-eddy and detached-eddy simulation. 2016; (2968): 153–164.

41. Lawson GNBSJ., Nayyar RSP. Numerical Simulations of High-Speed Turbulent Cavity Flows. 2009; : 569–585. Available at: DOI:10.1007/s10494-009-9207-1

42. Rasquin M., Ny T., Ali M. Parallel Adaptive Detached Eddy Simulations of the EUROLIFT DLR-F11 high lift configuration. 2014; (June): 1–15. Available at: DOI:10.2514/6.2014-2570

43. Escobar JA., Suarez CA., Silva C., Velandia JS., Lara CA., Simulation LE., et al. Detached Eddy Simulation of the DLR - F11 wing / body. 2014; (June): 1–15. Available at: DOI:10.2514/6.2014-2398

44. Squires KD., Krishnan V., Forsythe JR. Prediction of the flow over a circular cylinder at high Reynolds number using detached-eddy simulation. 2008; 96: 1528–1536. Available at: DOI:10.1016/j.jweia.2008.02.053

45. Versteeg HK., Malalasekela W. An introduction to Computational Fluid Dynamics: the finite volume method. second edi. Harlow, England: Pearson Education Limited; 2007.

46. Spalart PR., Allmaras SR. A one-equation turbulent model for aerodynamic flows. AIAA 30th Aerospace Sciences Meeting and Exhibit. Reno, Nevada; 1992.

47. ANSYS I. ANSYS FLUENT 15.0 Theory Guide, Chapter 4.2.7. 2013.

48. Menter FR. Two-Equation Eddy-Viscosity Turbulence Models for Engineering Applications. AIAA Journal. 1994; 32(8): 1598–1605. Available at: DOI:10.2514/3.12149

49. Menter FR. Zonal Two Equation k-ω , Turbulence Models for Aerodynamic Flows. 23rd Fluid Dynamics, Plasmadynamics, and Lasers Conference, Fluid Dynamics and Co-located Conferences. Orlando,FL,U.S.A.; 1993. pp. 1–21. Available at: DOI:10.2514/6.1993-2906

50. ANSYS I. ANSYS FLUENT 15.0 Theory Guide, Chapter 4.4.1.6. 2013.

51. Townsend AA. The structure of turbulent shear flow. London: Cambridge U. Press.; 1975. 429 p.

52. Slotnick JP., Hannon JA., Chaffin M. Overview of the 1st AIAA CFD High Lift Prediction Workshop. 49th AIAA Aerospace Sciences Meeting including the New Horizons Forum and Aerospace Exposition. Orlando, Florida; 2011.

53. Trap Wing Geometry cruise configuration diagram. 2009. Available at: https://hiliftpw.larc.nasa.gov/Workshop1/cruisediagram-09June09.pdf

54. Adhikari N., Nichols DS. Grid Generation About High-Lift Wing Configurations. Numerical Simulation of the Aerodynamics of High-Lift Configurations. Springer; 2018.

55. Pointwise I. Pointwise User Manual. Fort Worth, Texas; 2016. p. 440.

56. Implicit vs. Explicit Numerical Methods. Available at: https://www.flow3d.com/resources/cfd-101/numerical-issues/implicit-versus-explicit-numerical-methods/

57. Roe PL. Characteristic-based Schemes for the Euler Equations. Annu. Rev. Fluid Mech. 1986; 18: 337–365.

58. ANSYS I. ANSYS FLUENT 15.0 Theory Guide, Chapter 20.3.3 Evaluation of Gradients and Derivatives. 2013.

59. 1st AIAA CFD High Lift Prediction Workshop :14x22 Wing Tunnel Information. Available at: https://hiliftpw.larc.nasa.gov/Workshop1/wall-info.html

60. ANSYS I. ANSYS FLUENT 15.0 Theory Guide, Chapter 20.3.2 Time Discreitization. 2013.

61. Roache PJ. Perspective: A Method for Uniform Reporting of Grid Refinement Studies. Journal of Fluids Engineering. 1994; 116: 405–413.

62. Fluids Engineering Division of ASME. Procedure for Estimation and Reporting of Uncertainty Due to Discretization in CFD Applications. Journal of Fluids Engineering. 2008; 130(July): 4. Available at: DOI:10.1115/1.2960953

63. Roache PJ. QUANTIFICATION OF UNCERTAINTY IN COMPUTATIONAL FLUID DYNAMICS. Annu. Rev. Fluid Mech. 1997; 29: 123–160.

64. Wiart L., Meunier M. Computational Assessment of the HiLiftPW-1 Trap-Wing Model Using the elsA CFD Software. the 1st AIAA High Lift Prediction Workshop. Orlando, Florida; 2011. pp. 1–31.

65. Wikipedia-Total pressure. Available at: http://en.m.wikipedia.org/wiki/Total-pressure